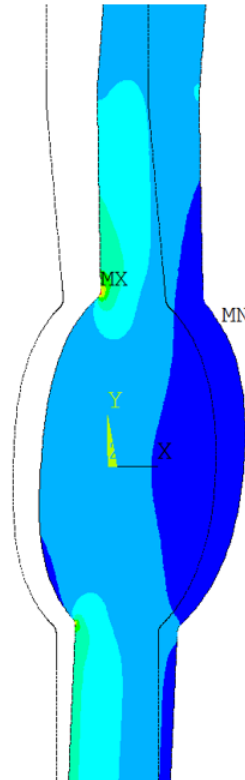
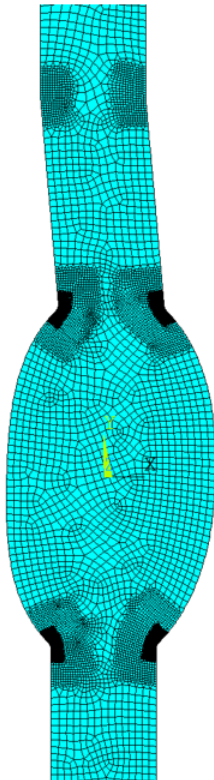


Degree Project in Engineering Mechanics  
Second Cycle, 30 Credits

# Fatigue life of butt welds – a numerical study on the influence of real geometry

KARTHICKEYAN ARASU





---

## Abstract

Welds play a crucial role in the product portfolio of GKN Aerospace. For ease of manufacturing and repairability, butt welds are preferred in the aerospace industry. Weld regions undergo local distortions during manufacturing due to the external heat-input, and the resulting local geometries are complex and stochastic in nature. Under operational loads, the distorted geometry affects the local stress field around the weld region, and this has a significant impact on the fatigue life.

Traditional design calculations of welds resort to idealization of the local weld geometry. In this thesis, the influence of real weld geometry on the computed fatigue life is investigated. Linear elastic fracture mechanics principles are utilized to calculate the fatigue life of a weld starting from a pre-defined initial crack. The influence of important weld geometric parameters, namely, – edge offset and weld toe radii, on the fatigue life is investigated in detail. A statistical analysis approach, using transfer functions and Monte Carlo simulation, is devised to study the effect of variation in the different weld geometric parameters. Different edge offset measures from a real geometry are identified and these measures are investigated as potential candidates to obtain conservative life estimates using the idealized geometry.

Investigations in this thesis show that the real geometry has a significant effect on the weld fatigue life. In all cases of local weld geometry, the edge offset has the largest influence on life. For a real weld geometry, the root toe radius has a significant influence on life. In an idealized geometry, for the same normalized edge offset, an increase in the plate thickness leads to a decrease in life. A new edge offset measure is proposed that leads to conservative life estimates when used in conjunction with the idealized geometry, thus enabling computationally efficient design calculations.

**Keywords:** Real weld geometry, fatigue life, edge offset, weld toe radius, crack propagation, transfer function, Monte Carlo simulation

---

## Sammanfattning

Svetsar spelar en avgörande roll i GKN Aerospace produktportfölj. För att underlätta vid tillverkning och reparationer föredras stumsvetsar inom flygindustrin. Svetsområden genomgår lokala deformationer under tillverkningen på grund av extern värmepåverkan, och de resulterande lokala geometrierna är komplexa och stokastiska till sin natur. Vid termisk och mekanisk belastning i drift påverkar den deformerade geometrin det lokala spänningsfältet runt svetsområdet vilket har en betydande inverkan på utmattningslivslängden.

Vid traditionell dimensionering av svetsar idealiseras den lokala svetsgeometrin. Denna avhandling undersöker inverkan av verklig svetsgeometri på den beräknade utmattningslivslängden. Linjärelastisk brottmekanik används för att beräkna utmattningslivslängden för en svets med utgångspunkt från en fördefinierad initial spricka. Inverkan av viktiga svetsgeometriska parametrar, nämligen - kantförskjutning och svetsradie, på utmattningslivslängden undersöks i detalj. En statistisk analysmetod, med hjälp av överföringsfunktioner och Monte Carlo simulering, är framtagen för att studera effekten av variation i de olika svetsgeometriska parametrarna. Olika kantförskjutningsmått från en verklig geometri identifieras och dessa mått undersöks som potentiella kandidater för att erhålla konservativa livslängdsuppskattningar med hjälp av den idealiserade geometrin.

Undersökningar i denna avhandling visar att den verkliga geometrin har en signifikant effekt på svetsutmattningslivslängden. I alla fall av lokal svetsgeometri har kantförskjutningen den största inverkan på livslängden. För en riktig svetsgeometri har svetsradien vid svetsens rotsida en betydande inverkan på livet. I en idealiserad geometri, för samma normaliserade kantförskjutning, leder en ökning av plåttjockleken till en minskning av livslängden. Ett nytt kantförskjutningsmått föreslås som leder till konservativa livslängdsuppskattningar när de används i kombination med den idealiserade geometrin, vilket möjliggör beräkningseffektiva designberäkningar.

**Nyckelord:** Verklig svetsgeometri, utmattningslivslängd, kantförskjutning, svetsradie, sprickutbredning, överföringsfunktion, Monte Carlo simulering

---

## Acknowledgements

Firstly, I would like to express my sincere gratitude to Dr. Sushovan Roychowdhury and Harald Söderlund, my supervisors at GKN Aerospace Sweden AB, for their expert guidance and consistent support in carrying out this Master's thesis project. Their valuable advice and constructive feedback truly helped improving every single aspect of this thesis.

I am extremely grateful to Rikard Nedar, Manager, Department of Solid Mechanics, for providing me this great learning opportunity, to work on this thesis, which has enabled me to gain insight into the aerospace industry. I would also like to extend my sincere thanks to all my colleagues and friends at GKN Aerospace, for their support throughout the thesis.

I would also like to express my deepest appreciation to my examiner Prof. Mårten Olsson, for his valuable comments and feedback on aspects of the thesis from an external academic view.

Finally, I would like to thank my family and friends, for being a constant support and encouragement, throughout my Master's studies.

Karthickeyan Arasu  
Trollhättan, Sweden, August 2023

---

# Table of Contents

<b>1</b>	<b>Introduction .....</b>	<b>1</b>
1.1	Background .....	1
1.2	Objective .....	3
1.3	Overview of work .....	4
1.4	Scope and limitations .....	4
<b>2</b>	<b>Theoretical Background.....</b>	<b>6</b>
2.1	Weld geometry .....	6
2.1.1	Schematic of a butt weld.....	6
2.1.2	Profilograph measurements .....	7
2.1.3	Types of local geometries .....	8
2.2	Fracture mechanics and fatigue.....	9
2.2.1	Linear elastic fracture mechanics .....	9
2.2.2	Fatigue crack propagation.....	10
2.2.3	NASGRO equation .....	13
2.3	Statistics .....	13
2.3.1	Types of statistical distributions .....	13
2.3.2	Statistical measures.....	14
2.3.3	Regression models .....	14
2.3.4	Design of Experiments .....	16
2.3.5	Empirical distribution function.....	19
<b>3</b>	<b>Weld measurements .....</b>	<b>20</b>
<b>4</b>	<b>Analysis Setup – Stress analysis and Life evaluation .....</b>	<b>21</b>
4.1	Stress analysis .....	21
4.1.1	Geometry Creation.....	21
4.1.2	Mesh and Material properties .....	23
4.1.3	Loads and boundary conditions .....	25
4.1.4	Stress gradient extraction.....	27
4.1.5	Forward and reverse bending.....	29
4.2	NASGRO Life calculation .....	29
4.2.1	Crack geometry.....	29
4.2.2	Material properties and failure criteria .....	30
4.2.3	Load blocks.....	31
4.3	Automation .....	32
4.3.1	Automation – Stress gradient extraction.....	32

---

4.3.2 Automation – Life evaluation .....	33
<b>5 Results – Deterministic analysis .....</b>	<b>35</b>
5.1 Initial Study – Case 1 geometry .....	35
5.2 Fatigue life results - Idealized Geometry .....	37
5.3 Fatigue life results - Real geometry .....	38
5.4 Fatigue life results – Different edge offset measures .....	40
<b>6 Analysis Setup – Monte Carlo Simulations .....</b>	<b>45</b>
6.1 Weld geometry parameters .....	45
6.2 Correlation between variables.....	49
6.3 Determination of transfer function.....	50
6.3.1 Transfer function for idealized geometry .....	51
6.3.2 Transfer function for real geometry.....	53
6.4 Monte Carlo Simulation.....	56
6.4.1 Number of Monte Carlo runs.....	56
6.4.2 Script algorithm to perform Monte Carlo simulation .....	57
<b>7 Results – Monte Carlo simulations .....</b>	<b>59</b>
7.1 Effect of thickness on fatigue life .....	59
7.1.1 Normalized edge offset.....	59
7.1.2 Absolute edge offset .....	60
7.2 Influence of real geometry on the fatigue life.....	62
7.3 Influence of different edge offset measures on fatigue life.....	65
7.3.1 Life distribution based on IG-LO <sub>1</sub> .....	66
7.3.2 Life distribution based on IG-LO <sub>2</sub> .....	67
7.3.3 Life distribution based on IG-LO <sub>4</sub> .....	69
<b>8 Conclusions.....</b>	<b>71</b>
8.1 Suggestions for future work .....	71
<b>9 References.....</b>	<b>73</b>
<b>10 Appendix I.....</b>	<b>75</b>
10.1 APDL script for mesh refinement.....	75
10.2 NASGRO FLABAT file structure .....	75
10.3 Fatigue life curves – Real geometry.....	76
10.4 Verification of transfer functions .....	77
10.5 MC convergence plots of <i>CAFL</i> .....	78

---

---

## List of Figures

Figure 1.1: Standard process for evaluation of fatigue life in welds .....	3
Figure 1.2: Illustration of an idealized weld geometry used in analysis .....	3
Figure 1.3: A typical TIG weld geometry .....	4
Figure 2.1: Illustration of a butt weld with the important geometric parameters .....	6
Figure 2.2: Casting wax placed on a weld in regions of interest .....	7
Figure 2.3: Typical profilograph measurement of a weld where the edge offset is measured .....	7
Figure 2.4: Case 1 - angular deflection more than one bead width .....	8
Figure 2.5: Case 2 - angular deflection within one bead width .....	8
Figure 2.6: Case 3 - angular deflection within one bead width .....	9
Figure 2.7: Case 4 - angular deflection within one bead width on both joining plates .....	9
Figure 2.8: Three modes of crack growth; sketch taken from ref. [2] .....	10
Figure 2.9: Edge crack in a strip under uniaxial tension $\sigma$ .....	10
Figure 2.10: Crack growth with applied cycles for different stress levels [2] .....	11
Figure 2.11: Typical $da/dN$ vs $\Delta K$ curve [13] .....	11
Figure 2.12: Effect of stress ratio ( $R$ ) on the fatigue crack growth rate [14] .....	12
Figure 2.13: Illustration of a response $y$ with respect to a variable $x$ .....	15
Figure 2.14: $2^3$ factorial design and respective design matrix [17] .....	17
Figure 2.15: Central Composite Design (CCD) for two and three factors [17] .....	17
Figure 2.16: CCD for three factors when $\alpha = 1$ [17] .....	18
Figure 2.17: Illustration of a 10-run Latin Hypercube Design for two factors [17] .....	18
Figure 4.1: Illustration of steps involved in the fatigue life prediction of a welded joint .....	21
Figure 4.2: Illustration of different weld geometries (a) IG (b) Case 1 (c) Case 2 .....	22
Figure 4.3: Construction of the weld bead .....	23
Figure 4.4: Illustration of mesh .....	23
Figure 4.5: Mesh convergence study .....	24
Figure 4.6: Fixed constraint applied to the highlighted edge of the model .....	25
Figure 4.7: Illustration of the two load steps (a) Load step 1 – Membrane (b) Load step 2 – Bending .....	26
Figure 4.8: Effect of large deformation on peak stress .....	27
Figure 4.9: Effect of large deformation on stress gradient (a) Membrane load = 1 MPa (b) Membrane load = 100 MPa .....	27
Figure 4.10: Illustration of (a) assumed initial crack for crack propagation analysis (b) Difference in maximum stress locations due to membrane and bending loads .....	28
Figure 4.11: Illustration of path definition for stress gradient extraction (a) Max stress at a location such that the crack grows along the global X-direction (b) Max stress at a location such that crack growth deviates from the global X-direction .....	28
Figure 4.12: Illustration of forward and reverse bending scenarios in IG and Case 2 geometries .....	29
Figure 4.13: SC30 crack geometry [10] .....	30
Figure 4.14: Stress gradients input in NASGRO (a) due to membrane load ( $S_0$ ) (b) due to bending load ( $S_1$ ) ...	31
Figure 4.15: Fatigue stress cycles used for the crack propagation analysis .....	32
Figure 4.16: Algorithm of steps followed to extract stress gradients .....	33
Figure 4.17: Algorithm of steps followed for evaluation of fatigue life .....	34
Figure 5.1: Illustration of case 1 analysis geometry .....	35
Figure 5.2: Results from FE analysis of case 1 geometry [ $\theta = 1^\circ$ ] (a) Stress distribution (in MPa) around weld region due to membrane load (1 MPa), plate length = 30 mm (b) Maximum stress in Y-direction due to membrane load as a function of the length of the plates .....	35
Figure 5.3: Length of joining plates vs observed life for case 1 geometry [ $\theta = 1^\circ$ ] .....	36
Figure 5.4: Illustration of higher moment resulting in reduction of fatigue life in case 1 geometry .....	36

---



Figure 5.5: Stress distributions (in MPa) around weld region due to membrane load (1 MPa) for an idealized geometry (a) $e/t = 0$ (b) $e/t = 0.41$ .....	37
Figure 5.6: Normalized edge offset vs fatigue life for idealized geometry [ $t = 4\text{mm}$ ] .....	38
Figure 5.7: Normalized edge offset vs fatigue life for real geometry [ $t = 4\text{mm}$ ; $\theta = 2^\circ$ ] .....	39
Figure 5.8: Maximum stress locations in real geometry for (a) No edge offset (b) With edge offset .....	39
Figure 5.9: Stress distributions (in MPa) around the weld region in a real geometry [ $t = 4\text{mm}$ ; $\theta = 2^\circ$ ; $f = 0.6$ ] due to membrane load (1 MPa) for (a) $e/t = 0.025$ (b) $e/t = 0.1$ .....	40
Figure 5.10: Illustration of two possible offset measurements in the real geometry .....	40
Figure 5.11: Different stress analysis geometries for a case with $RO = 0.05$ , $\theta = 2^\circ$ and $f = 0.6$ (a) RG (b) IG [ $RO = 0.05$ ] (c) IG [ $LO_1 = 0.15$ ] .....	41
Figure 5.12: Stress gradients due to membrane load for three cases in Table 5.3 .....	41
Figure 5.13: Different stress analysis geometries for a case with $RO = 0.025$ , $\theta = 2^\circ$ and $f = 0.6$ (a) RG (b) IG [ $RO = 0.025$ ] (c) IG [ $LO_1 = 0.043$ ] .....	42
Figure 5.14: Stress gradients due to membrane load for three cases in Table 5.4 .....	42
Figure 5.15: Different stress analysis geometries for a case with $RO = 0.08$ , $\theta = 2^\circ$ and $f = 0.6$ (a) RG (b) IG [ $RO = 0.08$ ] (c) IG [ $LO_1 = 0.16$ ] .....	43
Figure 5.16: Stress gradients due to membrane load for three cases in Table 5.5 .....	43
Figure 5.17: Fatigue life results for various cases of idealized and real geometries .....	44
Figure 6.1: Illustration of steps involved to perform a Monte Carlo simulation .....	45
Figure 6.2: Histogram of normalized edge offset and exponential distribution fit .....	46
Figure 6.3: Histogram of normalized top toe radius and lognormal distribution fit .....	46
Figure 6.4: Histogram of normalized root toe radius and lognormal distribution fit .....	47
Figure 6.5: Uniform distribution for local angular deflection ( $\theta$ ) .....	47
Figure 6.6: Idealized geometries at the extremities of the design space (a) lower bounds (b) upper bounds .....	49
Figure 6.7: Real geometries at the extremities of the design space (a) lower bounds (b) upper bounds .....	49
Figure 6.8: Correlation plots (a) $norm\_e$ vs $norm\_TR$ (b) $norm\_e$ vs $norm\_RR$ (c) $norm\_TR$ vs $norm\_RR$ .....	50
Figure 6.9: Fifteen full simulation points according to CCD for training IG transfer function .....	52
Figure 6.10: Seventy-five full simulation points according to LHS for training IG transfer function .....	52
Figure 6.11: Full simulation vs Predicted life from transfer function of IG [Thickness = 2.03 mm] .....	53
Figure 6.12: Twenty-five full simulation points according to CCD for training real geometry transfer function .....	54
Figure 6.13: Seventy-five full simulation points according to LHS for training real geometry transfer function .....	54
Figure 6.14: Full simulation vs Predicted life from transfer function for real geometry [Thickness = 2.03 mm] .....	56
Figure 6.15: Convergence plot of $CAFL$ for 20 iterations of 50000 MC runs .....	57
Figure 6.16: Algorithm for MC simulation - idealized geometry .....	58
Figure 7.1: Empirical CDF of fatigue life for three thickness cases – Idealized geometry (IG) .....	59
Figure 7.2: Empirical CDF of fatigue life for three thickness cases – Idealized geometry (IG) [ $e = 0.3\text{ mm}$ ] .....	60
Figure 7.3: a-tip and c-tip in a surface crack .....	61
Figure 7.4: Crack size vs Applied cycles of a-tip and c-tip for three thicknesses - IG [ $e = 0.3\text{ mm}$ ] .....	61
Figure 7.5: Stress intensity factor range $\Delta K$ vs crack size at c-tip for three thicknesses - IG [ $e = 0.3\text{ mm}$ ] .....	62
Figure 7.6: Empirical CDF of fatigue life for idealized and real geometries [Thickness = 2.03 mm] .....	63
Figure 7.7: Contribution to variance in fatigue life from three input variables - idealized geometry .....	63
Figure 7.8: Contribution to variance in fatigue life from four input variables - real geometry .....	64
Figure 7.9: Dependence of life on normalized edge offset from results of MC simulation (a) Idealized geometry (b) Real geometry .....	65
Figure 7.10: Dependence of life on normalized top toe radius from results of MC simulation (a) Idealized geometry (b) Real geometry .....	65
Figure 7.11: Dependence of life on normalized root toe radius from results of MC simulation (a) Idealized geometry (b) Real geometry .....	65
Figure 7.12: Three offset measures - $RO$ , $LO_1$ and $LO_2$ .....	66
Figure 7.13: Schematic representation of geometry for calculation of $LO_1$ and $LO_2$ .....	66

---

Figure 7.14: Illustration of $LO_1$ measure relative to $RO$ for two cases when (a) $LO_1$ below $X_{ref}$ (b) $LO_1$ above $X_{ref}$ .....	67
Figure 7.15: Empirical CDF of fatigue life for two offset measures - $RO$ and $LO_1$ [Thickness = 2.03 mm] .....	67
Figure 7.16: $LO_2$ measure relative to $RO$ in (a) <i>Region C</i> and (b) <i>Region D</i> .....	68
Figure 7.17: Empirical CDF of fatigue life for two offset measures - $RO$ and $LO_2$ [Thickness = 2.03 mm] .....	68
Figure 7.18: Empirical CDF of fatigue life for three offset measures and real geometry [Thickness = 2.03 mm] .....	69
Figure 7.19: Empirical CDF of fatigue life for $LO_4$ measure along with other cases .....	70

---

## List of Tables

Table 2.1: List of important weld geometric parameters .....	6
Table 2.2: List of additional geometric parameters to account for local geometry cases.....	9
Table 4.1: List of parameters and values used for the analysis .....	22
Table 4.2: Results from mesh convergence study .....	24
Table 4.3: Results for plane stress and plane strain conditions - Case 2 geometry [ $\theta = 5^\circ; f = 0.7$ ].....	24
Table 4.4: Material properties used in the analysis [20] .....	25
Table 4.5: Applied loads for the analysis .....	25
Table 4.6: Crack plane dimensions used for crack propagation analysis .....	30
Table 4.7: Paris law parameters of IN718 for crack propagation analysis.....	30
Table 5.1: List of parameters used for Case 1 geometry analysis .....	35
Table 5.2: Bounds for parameters of real geometry used for deterministic analysis.....	38
Table 5.3: Example 1 – Parameters of a real geometry and life results from three analysis approaches .....	41
Table 5.4: Example 2 – Parameters of a real geometry and life results from three analysis approaches .....	42
Table 5.5: Example 3 – Parameters of a real geometry and life results from three analysis approaches .....	43
Table 6.1: Variables considered for MC simulation .....	45
Table 6.2: Parameters of exponential distribution fit for normalized edge offset .....	46
Table 6.3: Parameters of lognormal distribution fit for normalized top toe radius .....	46
Table 6.4: Parameters of lognormal distribution fit for normalized root toe radius .....	47
Table 6.5: Values of weld geometry parameters used in MC simulation.....	48
Table 6.6: Other weld geometric parameter values used in MC simulation .....	48
Table 6.7: Lower and Upper bounds of the design space for MC simulation .....	48
Table 6.8: Correlation coefficients of three variable pairs .....	50
Table 6.9: Regression coefficients of transfer functions for IG – Three plate thicknesses .....	52
Table 6.10: $R^2$ and $R^2_{adj}$ values of IG transfer functions for respective plate thickness values .....	53
Table 6.11: Regression coefficients of transfer function for real geometry [Thickness = 2.03 mm] .....	55
Table 6.12: $R^2$ and $R^2_{adj}$ values of the transfer function for real geometry [Thickness = 2.03 mm].....	55
Table 6.13: Coefficient of variation for $CAFL$ for various cases of MC runs.....	56
Table 7.1: Minimum life and median life for three thickness cases – Idealized geometry .....	59
Table 7.2: $norm\_e$ values for different plate thicknesses [ $e = 0.3$ mm] .....	60
Table 7.3: Minimum life and median life for three thickness cases – IG [ $e = 0.3$ mm] .....	60
Table 7.4: Fatigue lives for three thickness cases from full simulation - IG [ $e = 0.3$ mm] .....	61
Table 7.5: Minimum life and median life for idealized (IG) and real (RG) geometries .....	62
Table 7.6: Minimum life and median life for two offset measures - $RO$ and $LO_1$ .....	66
Table 7.7: Minimum life and median life for two offset measures - $RO$ and $LO_2$ .....	67
Table 7.8: Minimum life for $LO_4$ measure and real geometry .....	69

# 1 Introduction

In recent years, sustainability has become the primary focus area in the aviation industry. The industry is working towards developing technologies that are environmentally friendly and meet the new emission standards. In an aircraft, the engine is the most crucial and most expensive component. Technological advancements in the engine will be a driving factor in the industry's transition to more sustainable travel [1].

The aircraft engine is a highly complex component. High-quality welds are an integral part of the manufacturing process. The welds enable lighter engines and thus directly contribute to reduce emissions. During a flight cycle, the engine undergoes complex load cycles and the welds play a critical role in maintaining structural integrity of the engine. During manufacturing, the weld regions undergo local deformation because of the external heat input. Residual stresses accompany these deformations. In the aerospace industry, it is a common practice to alleviate the residual stress through post-weld heat treatment. However, the deformed geometry remains, and, during operation of the engine, affects the local stress field around the weld. Therefore, it is important to study the effect of such geometric variations on fatigue life.

## 1.1 Background

Different methods are used in the literature to evaluate the fatigue life of a component that undergoes cyclic loading. Most approaches are based on S-N curves obtained from constant-amplitude tests [2], where S represents applied stress and N represents corresponding fatigue life. In the case of variable-amplitude loading, damage accumulation hypothesis such as Palmgren-Miner rule is employed [2]. Other approaches include crack propagation methods, which assumes an initial crack is present in the component.

The above methods can also be applied in evaluating the fatigue life of welds [3]. The fatigue life of welds are highly affected by factors such as the applied stress range ( $\Delta S$ ), material property, the weld geometry, and other microscopic and macroscopic defects. The weld geometric parameters include features such as the weld toe radius, undercut and misalignment [2].

Several studies have been carried out by different authors investigating the various weld geometric parameters and its effect on fatigue life [4] [5]. Through experimental fatigue tests and fracture surface analysis of laser-MAG hybrid butt-welded specimens, it was identified that Fatigue Crack Initiation (FCI) location was dictated mainly by the undercut depth [4]. With Linear Elastic Fracture Mechanics (LEFM), Finite Element Analysis (FEA) and superposition approaches, the effect of the weld geometry parameters of butt-welded specimens on Fatigue Crack Propagation (FCP) life was investigated [5]. From this study, it was concluded that initial

crack growth was controlled by the weld geometry, after which the geometry did not play a significant role on FCP life.

The type of welding process can also affect the fatigue life of a joint. Butt-welded specimens with three different techniques: Gas Metal Arc Welding (GMAW), Laser Hybrid Welding (LHW) and Electron Beam Welding (EBW) were fatigue tested and fracture mechanics method was employed to study the fatigue behaviour [6]. It was observed that GMAW resulted in high quality weld profile, which meant a smaller initial crack size. In the case of LHW and EBW, the differences in the S-N curves cannot be solely explained by the resulting weld profiles, since the fatigue life is also influenced by defects such as undercuts and underfills. It is thus important to acknowledge the presence of possible defects in the design calculations of welds.

The fatigue life of a welded joint is also sensitive to the stochastic nature of its geometric parameters. Reliability of butt-welded joints considering uncertainties in geometric parameters such as misalignment, weld toe radius, flank angle and crack like imperfections (secondary notch) were assessed [7]. It was concluded that, while the above-mentioned parameters are important sources of total uncertainty, it is seen that the weld toe radius and secondary notch have a significant effect on the reliability index. Moreover, an increase in the fatigue reliability was observed for higher quality of welds.

In order to ensure high reliability, a common practice in the aerospace industry is to employ fracture mechanics principles to predict the fatigue life of welds. This approach assumes the presence of a small crack in the weld. The fatigue life of the weld is the number of stress cycles taken by the crack to grow to a critical size. The critical size is the one that causes a loss of function of the component. A fatigue crack propagation analysis is used to compute the cycles to failure.

The approach, as illustrated in Figure 1.1, involves evaluating the stresses in a global model without considering the local weld geometric features. The stresses at the weld region are linearized and the membrane and bending stresses are evaluated. A local beam or a tube model, with the weld geometric features included, is subjected to unit membrane and bending stresses and the corresponding stress gradients are extracted. By combining the linearized stresses from the global model and the stress gradients from the local model, the crack propagation life is evaluated [8].

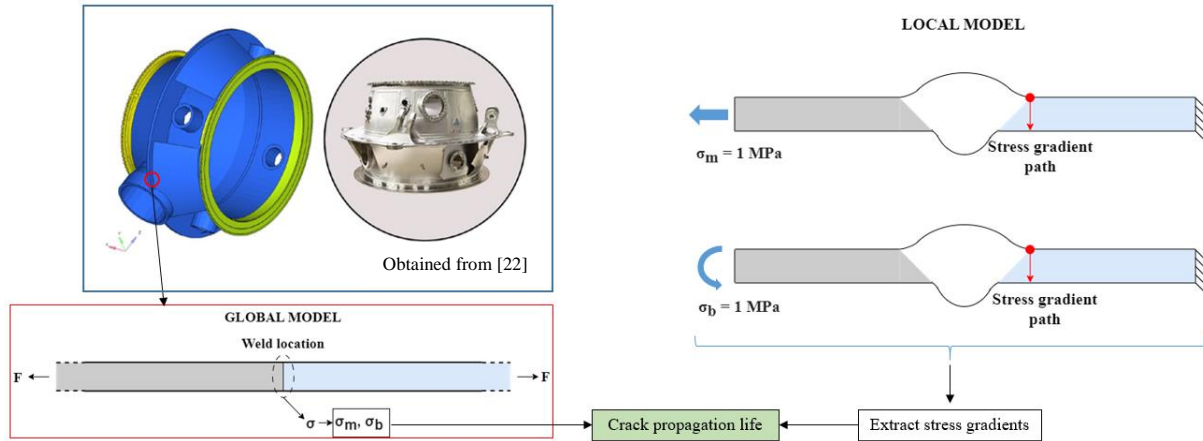


Figure 1.1: Standard process for evaluation of fatigue life in welds

A comparison between crack propagation experiments and the standard analysis method followed within GKN was carried out [9]. The crack propagation tests were conducted on IN718 sheet material that were manufactured to reflect the geometry in a GKN weld specification. From the obtained results, it was concluded that the fracture mechanics approach provides a good accuracy in predicting the fatigue life of welded joints. The life predicted using the standard practice is also generally conservative compared to the experimental results. However, the local deflections around the weld region and the effect of the weld toe radius on the fatigue life was not studied in this report.

## 1.2 Objective

The edge offset and the weld toe radius are two important parameters that have the most pronounced effect on the fatigue life. Usually, in the design calculations, the edge offset ( $e$ ) is applied between two parallel plates, which is an ideal scenario. The weld toe radius ( $R$ ) is considered 10% of the plate thickness. If the two joining plates are of varying thickness, the minimum thickness value is considered [8]. An illustration of this ideal geometry is shown in Figure 1.2.

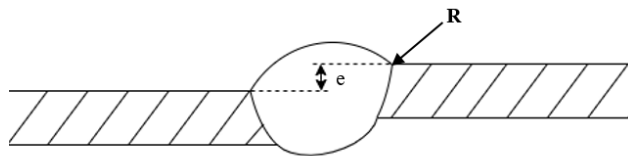


Figure 1.2: Illustration of an idealized weld geometry used in analysis

However, in reality the local geometry around the weld region differ significantly from the ideal scenario. Figure 1.3 shows the picture of a typical TIG weld. One of the first observations is that the joined plates are not parallel to each other. Further, in this case, the weld toe radii are large, since the weld bead on the top side is nearly flush with the plates. In general, it is observed that the local weld geometry vary significantly from the idealized one depicted in Figure 1.2. Some of the typical local geometries are discussed further in Section 2.1.3. Since such local deformations are common, it is important to understand the effect of these variations on the

fatigue life. Additionally, given the stochastic nature of these geometric parameters it is important to study the sensitivity of weld fatigue life on the various geometric parameters that define the local weld region.



Figure 1.3: A typical TIG weld geometry

Thus, the objectives of this thesis can be stated as follows.

1. Study the effect of distorted local geometries around the weld region on the fatigue life. Compare the results with those from the idealized geometry.
2. Investigate the sensitivity of calculated fatigue life to different edge offset measures and weld toe radii in the context of distorted local geometry. Quantify the results by comparing with idealized geometry.

### **1.3 Overview of work**

To achieve the objectives, in the first phase of the thesis, dimensional measurements of various weld geometric parameters are collected from typical GKN products, which is discussed further in Chapter 3. A deterministic study is carried out to evaluate the effect of distorted local geometries on the fatigue life. The analysis setup conditions for performing stress analysis and life evaluation are discussed in Chapter 4. Ansys APDL 2022R1 software is used to perform stress analysis. Crack propagation analysis for evaluating fatigue life is carried out in NASGRO 9.1 [10]. The results from the deterministic study are discussed in Chapter 5.

In order to statistically investigate the effect of different edge offset measures and weld toe radii on fatigue life, Monte Carlo simulations are performed using Python and MATLAB. The analysis setup conditions for Monte Carlo simulation are discussed in Chapter 6 and the results from the study are discussed in Chapter 7. Chapter 8 provides the conclusions from the work.

### **1.4 Scope and limitations**

All the results presented in this thesis are from numerical analysis alone, and no experimental tests were performed. To evaluate the stresses of various local weld geometries, linear and small deformation conditions are assumed. LEFM conditions are assumed for crack propagation analysis and an initial surface crack is considered for the fatigue life calculations.

The compiled measurement data for various weld geometric parameters is available for different types of welding processes: Tungsten Inert Gas (TIG) and Laser Beam Welding

(LBW) and for different base materials: Nickel base or Titanium base. However, only the data compiled for Nickel base TIG welds is used for analysis. Therefore, the effect of different welding processes is not investigated in this thesis work.



## 2 Theoretical Background

As explained in Chapter 1, this thesis investigates the effect of local geometry on the fatigue life of butt welds through a fracture mechanics approach, and uses statistical methods to quantify such effects. This chapter provides relevant theoretical background in these areas.

### 2.1 Weld geometry

#### 2.1.1 Schematic of a butt weld

A typical butt weld geometry of two plates joined together is shown in Figure 2.1. A butt weld has two regions: the top side and the root side. The top side corresponds to the side on which the welding operation is performed and the opposite side is referred to as the root side.

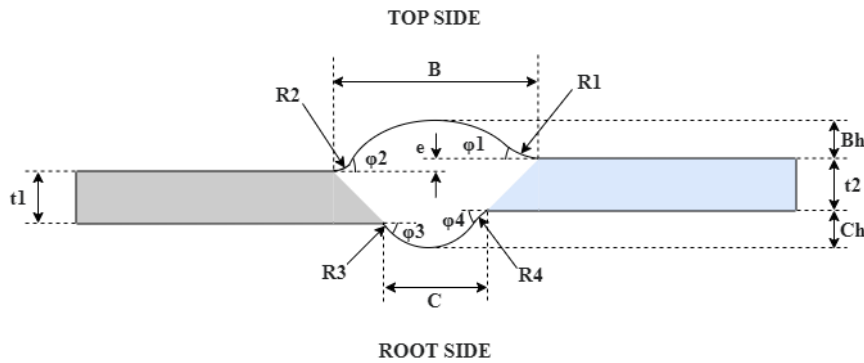


Figure 2.1: Illustration of a butt weld with the important geometric parameters

A description of the important geometric parameters as shown in the figure is listed in Table 2.1.

Table 2.1: List of important weld geometric parameters

<i>Parameter</i>	<i>Description</i>
$t1$	Thickness of plate #1
$t2$	Thickness of plate #2
$B$	Weld bead width on the top side
$Bh$	Weld bead height on the top side
$C$	Weld bead width on the root side
$Ch$	Weld bead height on the root side
$e$	Edge offset between the two plates
$\phi1 - \phi4$	Internal weld bead angles
$L1$	Length of plate #1
$L2$	Length of plate #2
$R1 - R4$	Weld toe radii

Previous studies have shown that the two important parameters that affect the fatigue life are the edge offset ( $e$ ) and the weld toe radius ( $R$ ). The edge offset ( $e$ ) is an important parameter, since it causes a local secondary bending moment that has a significant effect on the fatigue life of the welded joint. The weld toe radii ( $R$ ) causes regions of stress concentration within the weld that has an effect on the life.

### 2.1.2 Profilograph measurements

According to standard inspection processes followed in the aerospace industry, all manufactured welds undergo visual inspection for any surface defects and weld features [11]. One method used for performing inspection on welds involves casting wax and profilograph measurements. The process begins with placing a casting wax on the welds in the region of interest as shown in Figure 2.2.



Figure 2.2: Casting wax placed on a weld in regions of interest

A profilograph is used on the cast wax to map the surface. This yields a profile of the weld bead surface as shown in Figure 2.3. Using such measurements the edge offset and other weld geometric parameters of interest can be measured.

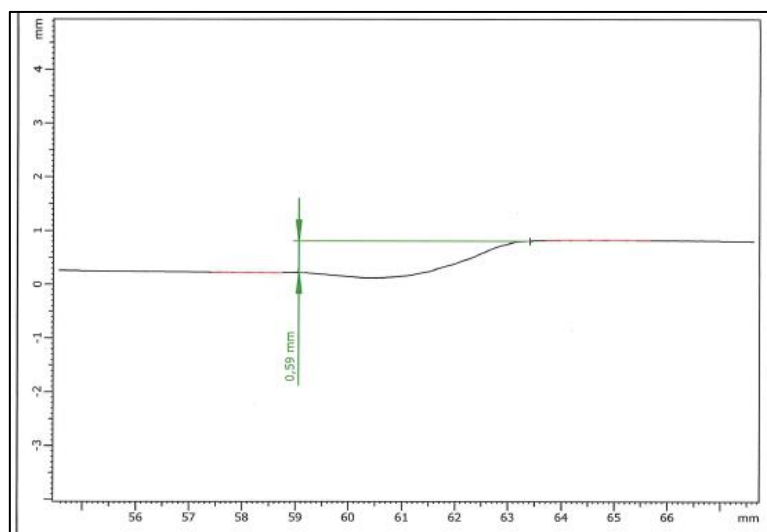


Figure 2.3: Typical profilograph measurement of a weld where the edge offset is measured

### 2.1.3 Types of local geometries

During the welding process, heat causes local deformation around the weld. In the as-welded state, these deformations are accompanied by residual stress. In the aerospace industry, post-weld heat treatments are carried out to eliminate the residual stress. However, the local geometry around the weld remains deformed and causes stress concentration under operating load. Based on the profilograph observations of the welds in a wide range of GKN products, four types of local geometries around the weld region have been identified [12].

In the first type of local geometry (Case 1, see Figure 2.4), one of the joining plates has a local angular deflection ( $\theta$ ) with respect to the other. However, the extent of the angular distortion is not known from the profilograph measurement. In this case, the edge offset ( $e$ ) is the distance measured between two parallel lines that are extrapolated from the weld toe radii of the two joining plates.

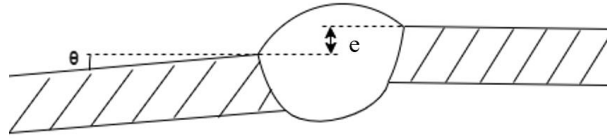


Figure 2.4: Case 1 - angular deflection more than one bead width

Case 2 is similar to the Case 1, but the length of the angular distortion can be identified from the profilograph measurement as illustrated in Figure 2.5. Here the edge offset is the distance between two parallel lines extrapolated from the two joining plates. The first line is extrapolated from the weld toe radius of the plate without the local deflection. The second line is extrapolated from the horizontal part of the plate with the local deflection.

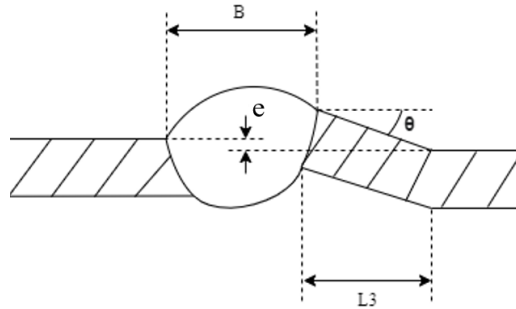


Figure 2.5: Case 2 - angular deflection within one bead width

For analysis purposes, the length of the angular distortion can be quantified as  $L3$  that can be expressed as

$$L3 = f * B \quad (1)$$

where  $f$  is a factor and  $B$  is the top bead width of the weld geometry. The additional parameters that are defined to account for the two local weld geometry cases are summarized in Table 2.2.

Table 2.2: List of additional geometric parameters to account for local geometry cases

<i>Parameter</i>	<i>Description</i>
$\theta$	Local angular deflection (Case 1 and Case 2)
$f$	Length factor of the local deflection (Case 2)

Case 3 is similar to the case 2, however the angular deflection has a geometry as illustrated in Figure 2.6.

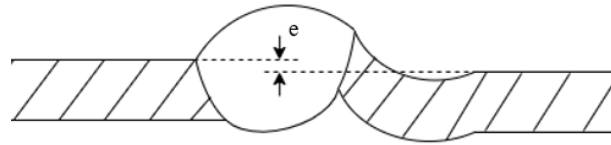


Figure 2.6: Case 3 - angular deflection within one bead width

In Case 4, both the joining plates have an angular deflection as illustrated in Figure 2.7.

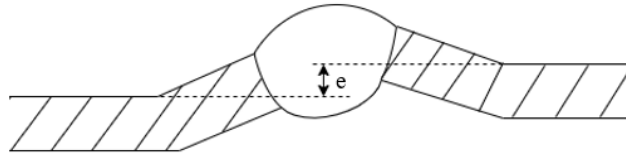


Figure 2.7: Case 4 - angular deflection within one bead width on both joining plates

This thesis will only focus on the idealized geometry as shown in Figure 1.2 along with Case 1 and Case 2 local geometries.

## 2.2 Fracture mechanics and fatigue

### 2.2.1 Linear elastic fracture mechanics

Fracture Mechanics provides the fundamental principles that are employed to study fatigue crack growth and evaluate the fatigue life of a component in the presence of a crack. In metallic materials, yielding takes place at the crack tip under external load. When the plastic zone is small compared to other dimensions of the problem, one can make use of Linear Elastic Fracture Mechanics (LEFM). In fatigue calculations based on LEFM, it is assumed that parameters obtained from linear elasticity assumptions can be used to capture the crack growth behaviour.

A crack can grow in three modes as shown in Figure 2.8 [2]. In Mode I, which corresponds to crack opening and is the most common one, the load acts normal to the crack plane. Mode II is the in-plane shearing or sliding mode, in which the two crack faces slide over each other. Mode III is the tearing or anti-plane shear mode [2].

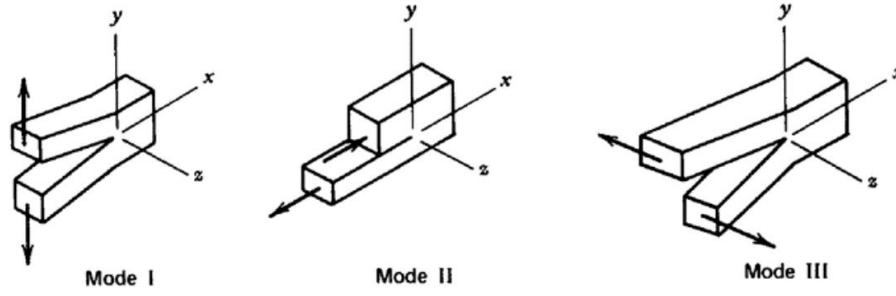
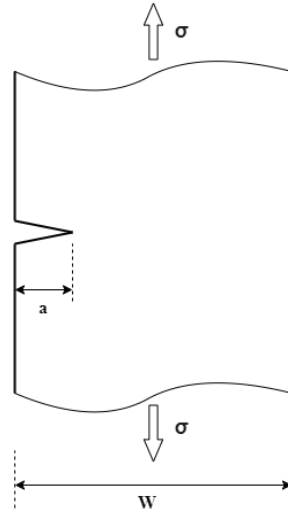


Figure 2.8: Three modes of crack growth; sketch taken from ref. [2]

The Stress Intensity Factor (SIF) denoted by  $K$  is an important quantity in fracture mechanics and is used to quantify the crack driving force. The SIF is given by

$$K = \sigma \sqrt{\pi a} f\left(\frac{a}{W}\right) \quad (2)$$

where  $\sigma$  is the applied stress,  $a$  is the crack length and  $f$  is a function that is dependent on the specimen geometry. It is dependent on the crack length and the specimen width  $W$ . The dimensions pertaining to a simple edge crack in a strip under uniaxial tension ( $\sigma$ ) is shown in Figure 2.9.

Figure 2.9: Edge crack in a strip under uniaxial tension  $\sigma$ 

The critical value of  $K$  for which the crack grows in an unstable manner under monotonic loading is defined as fracture toughness and is denoted as  $K_c$ . The fracture toughness of a material is highly dependent on the thickness of the specimen, as it determines whether plane stress/strain conditions are present at the crack tip.

### 2.2.2 Fatigue crack propagation

Consider a specimen with an initial crack size  $a_0$ . The specimen is subjected to three different cyclic stress levels  $S_1$ ,  $S_2$ ,  $S_3$  that can be ranked in descending order as  $S_1 > S_2 > S_3$ . Figure 2.10 shows, schematically, crack growth with the applied load cycles for the different cases given the same initial crack size.

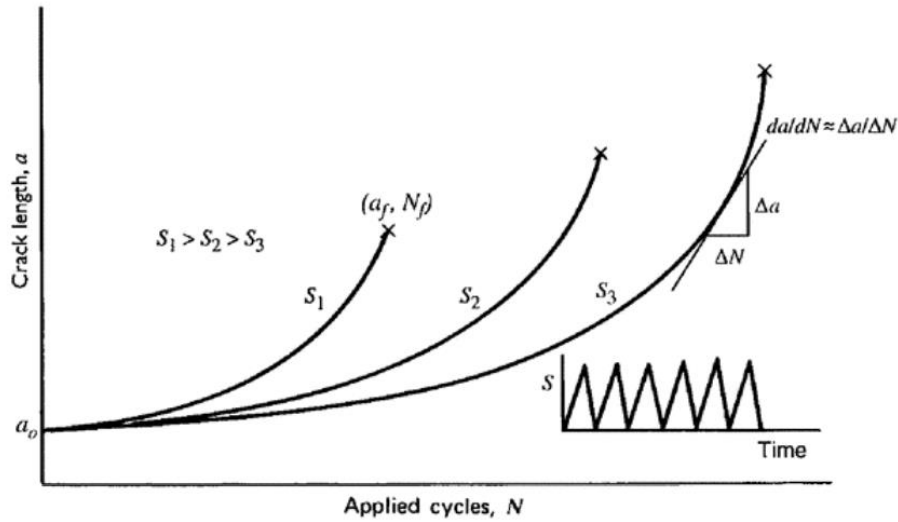
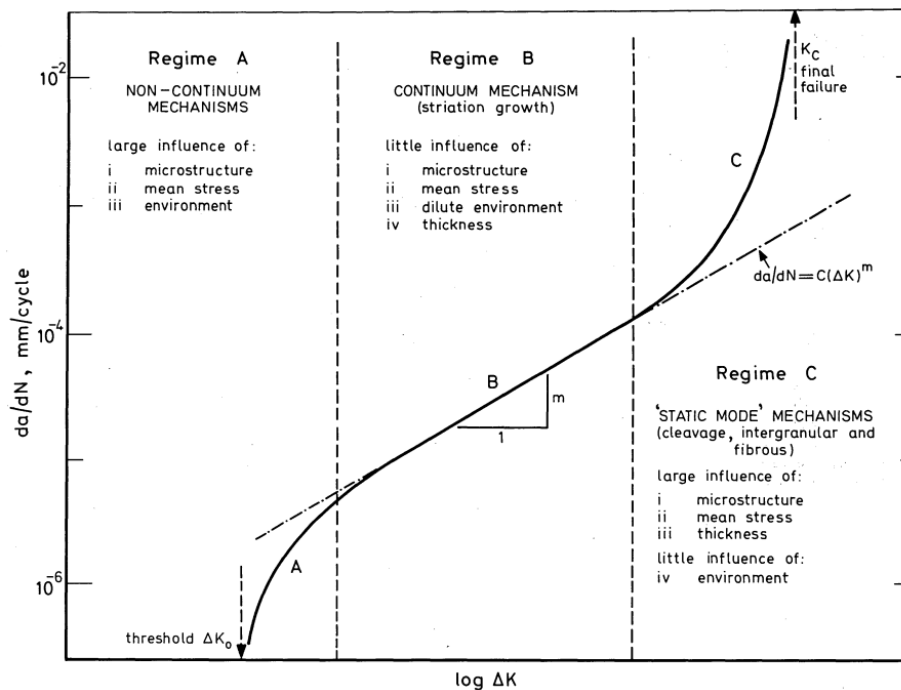


Figure 2.10: Crack growth with applied cycles for different stress levels [2]

The end of all the curves signifies the point of fracture. It can be seen that the crack growth rate increases as the magnitude of the applied load increases. Further, the number of cycles to fracture ( $N_f$ ) and the crack length at fracture ( $a_f$ ) decrease with an increase in the magnitude of applied load.

The curves shown in Figure 2.10 cannot be directly used in the fatigue design of components. Using LEFM concepts the data can be expressed in terms of fatigue crack growth rate ( $da/dN$ ) vs the applied stress intensity factor range ( $\Delta K$ ). Such a typical curve is shown in Figure 2.11. The curve can be divided into three main regions.

Figure 2.11: Typical  $da/dN$  vs  $\Delta K$  curve [13]

Regime A is the near-threshold region and corresponds to the threshold stress intensity factor ( $\Delta K_o$ , also denoted as  $\Delta K_{th}$ ) below which the cracks do not propagate. Various factors such as the mean stress and microstructure have a strong influence on the crack growth rates in this region. Crack growth in this region also displays, increased sensitivity to stress history and environmental effects [13].

Regime B corresponds to the region where the linear relationship between  $da/dN$  and  $\Delta K$  holds. Crack growth in this region is governed by the Paris law as shown below,

$$\frac{da}{dN} = C (\Delta K)^m \quad (3)$$

where  $C$  and  $m$  are constants that are determined through data fitting to experimental test results and  $\Delta K$  is the difference between the maximum and the minimum applied stress intensity factors i.e.,  $\Delta K = K_{max} - K_{min}$ . Regime C corresponds to higher crack growth rates and the  $K_{max}$  values generally approach the fracture toughness value ( $K_c$ ).

A fatigue load cycle alternates between a minimum stress level ( $\sigma_{min}$ ) and a maximum stress level ( $\sigma_{max}$ ). The stress ratio ( $R$ ) is then defined as

$$R = \frac{\sigma_{min}}{\sigma_{max}} \quad (4)$$

With LEFM assumptions, in view of Equation (2),  $R = K_{min}/K_{max}$ .

The effect of the stress ratio on the fatigue crack growth rate is shown in Figure 2.12. It is observed that the effect of the stress ratio is more pronounced in the near-threshold and fracture toughness regions (Regions A and C) compared to the linear region (Region B).

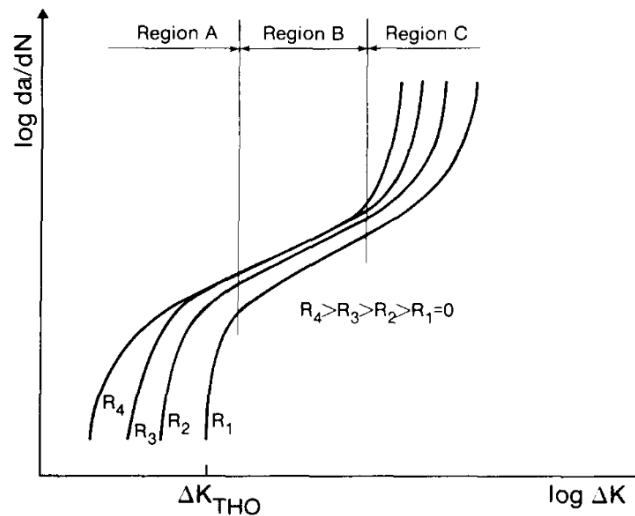


Figure 2.12: Effect of stress ratio ( $R$ ) on the fatigue crack growth rate [14]

### 2.2.3 NASGRO equation

To evaluate the fatigue life of welds, crack propagation analysis is carried out in NASGRO in this thesis work. The crack growth equation used in NASGRO is a modified form of the Paris law as shown in Equation (3) and is often referred to as the NASGRO equation. Along with the Paris law region, the NASGRO equation accounts for both the near-threshold region as well as the end of life region in the  $da/dN$  vs  $\Delta K$  curve. The NASGRO equation can be expressed as,

$$\frac{da}{dN} = C \left[ \left( \frac{1-f}{1-R} \right) \Delta K \right]^n \frac{\left( 1 - \frac{\Delta K_{th}}{\Delta K} \right)^p}{\left( 1 - \frac{K_{max}}{K_c} \right)^q} \quad (5)$$

where  $N$  is the number of applied fatigue cycles,  $a$  is the crack length,  $R$  is the stress ratio,  $\Delta K$  is the stress intensity factor range and  $C$ ,  $n$ ,  $p$  and  $q$  are empirically derived constants. The term  $\Delta K_{th}$  represents the threshold stress intensity factor,  $f$  is the crack opening function and  $K_c$  is the critical stress intensity factor [10]. The crack opening function accounts for plasticity-induced crack closure that takes place during fatigue crack growth. More details can be found in the NASGRO manual [10].

## 2.3 Statistics

### 2.3.1 Types of statistical distributions

Several statistical distribution functions are available in the literature. Here we mention the ones used in the current work.

The uniform distribution is applicable when the variable under consideration has known lower and upper bounds and can take equally likely values in this range. If  $X$  is a continuous random variable and can take any value within a given range  $[a, b]$ , then the probability density function for a uniform distribution is expressed as [15]

$$f(x) = \begin{cases} 1/(b-a), & a \leq x \leq b \\ 0, & \text{otherwise} \end{cases} \quad (6)$$

The exponential distribution is another type of distribution, whose probability density function can be expressed as

$$f(x) = \lambda e^{-\lambda x} \quad \text{for } 0 \leq x < \infty \quad (7)$$

where  $\lambda$  is a distribution parameter, and is defined for positive values of  $x$ . The mean and the standard deviation is then given by  $1/\lambda$ .



If the region of interest for a parameter is only the positive real numbers, a lognormal distribution can be used. The lognormal distribution is used in wide range of applications, such as, material strength, fatigue life, loading intensity etc. [15]. A random variable  $X$  is said to follow lognormal distribution if  $\ln X$  is normally distributed. The probability density function for a lognormal distribution can be expressed as

$$f(x) = \frac{1}{x\sigma\sqrt{2\pi}} \exp\left\{-\frac{1}{2}\left(\frac{\ln(x) - \mu}{\sigma}\right)^2\right\} \quad \text{for } 0 < x < \infty \quad (8)$$

where  $\mu$  is the mean value of  $\ln X$  and  $\sigma$  is the standard deviation of  $\ln X$ .

### 2.3.2 Statistical measures

Given two or more random variables, it is often useful to understand how the variables vary with respect to each other. For two random variables  $X$  and  $Y$ , a common measure of the relationship between the two variables is the covariance that can be defined as [16],

$$\text{cov}(X, Y) = E[(X - \mu_X)(Y - \mu_Y)] \quad (9)$$

where  $E$  is the expected value of a distribution,  $\mu_X$  is the mean value of  $X$  and  $\mu_Y$  is the mean value of  $Y$ . The covariance can be explained as the expected value of the product of the individual deviations of the two random variables from their respective mean values. Another measure of the relationship between two variables is the correlation coefficient. This can be defined as follows,

$$\rho_{xy} = \frac{\text{cov}(X, Y)}{\sigma(X) \sigma(Y)} \quad (10)$$

where  $\sigma(X)$  and  $\sigma(Y)$  are the standard deviations of  $X$  and  $Y$  respectively. The above definition is also known as the Pearson's correlation coefficient. The correlation coefficient scales the covariance by the standard deviation of each variable. Hence, it is a dimensionless quantity and can be used to compare relationships between pairs of variables of different units. Moreover,  $\rho_{xy}$  varies between -1 and +1 and the value of  $\rho_{xy}$  signifies the type of correlation between the pair of variables. The two variables have a positive correlation if the value of  $\rho_{xy}$  is +1. If the value of  $\rho_{xy}$  is -1, the two variables have a negative correlation and if the value of  $\rho_{xy}$  is 0, then the two variables are independent or have no correlation.

### 2.3.3 Regression models

In many problems, it is important to study the relationship between multiple variables. The relationship between multiple weld geometric parameters and the resulting fatigue life of the joint constitute such an example. In general, consider a single dependent or response variable  $y$

that is dependent on  $k$  independent or regressor variables, for example  $x_1, x_2, \dots, x_k$  as shown below

$$y = \beta_0 + \beta_1 x_1 + \beta_2 x_2 + \dots + \beta_k x_k + \epsilon \quad (11)$$

The mathematical relationship between the variables is known as a *regression model*. Specifically, the above equation is a multiple linear regression model since the equation is a linear function. The parameters  $\beta_k$  are known as regression coefficients and  $\epsilon$  is the error. In most cases, the true relationship between the variables is not known and instead an approximate function is used [17]. Sometimes it is of interest to study the interaction effects between the variables and for such a case, Equation (11) can be rewritten for two variables as,

$$y = \beta_0 + \beta_1 x_1 + \beta_2 x_2 + \beta_{12} x_1 x_2 + \epsilon \quad (12)$$

If we consider  $\beta_3 = \beta_{12}$  and  $x_3 = x_1 x_2$ , we can still express Equation (12) in the form of the Equation (11). The term  $\beta_{12} x_1 x_2$  accounts for the interaction effects [17].

In general, a second order regression model with interaction effects can be expressed as,

$$y = \beta_0 + \sum_{j=1}^k \beta_j x_j + \sum_{i < j} \beta_{ij} x_i x_j + \sum_{j=1}^k \beta_{jj} x_j^2 + \epsilon \quad (13)$$

Similar to Equation (12), a second order regression model can also be expressed as a linear regression model through clever assignment of variables. This is because all the above equations vary linearly with respect to the parameter  $\beta$ .

The choice of the appropriate regression model depends on the how the response variable is expected to vary with respect to the regressor variables. For example, consider a scenario as illustrated in Figure 2.13.

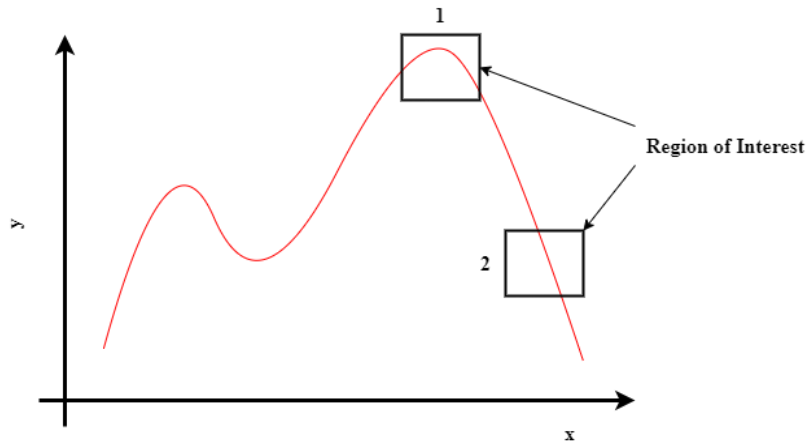


Figure 2.13: Illustration of a response  $y$  with respect to a variable  $x$

In Region of Interest 1 (ROI 1 in Figure 2.13), the response shows a quadratic behaviour where a second order regression model is an appropriate choice. However, in ROI 2, the response shows a linear behaviour and therefore a first order regression model would suffice. In this thesis work, the second order regression model will be used which is discussed further in Section 6.3.

With the parameters of a regression model identified, it is important to test the veracity of the model. The validation of the regression model can be done in several ways. One approach is to check the accuracy of the model with additional points within the design space. Quantities such as  $R^2$  or  $R^2_{adj}$  can be used to check the adequacy of the model. The quantity  $R^2$  is known as the coefficient of determination which is given by,

$$R^2 = \frac{SS_R}{SS_T} = 1 - \frac{SS_E}{SS_T} \quad (14)$$

where  $SS_T$  is the total sum of squares ( $SS_T = SS_R + SS_E$ ),  $SS_R$  is the sum of squares due to the regression model and  $SS_E$  is the sum of squares due to the residual. For more details, refer [16]. The  $R^2$  is a measure of how well the regression model fits the response and a higher  $R^2$  value indicates a better fit. However, the  $R^2$  value increases as variables are added to the model irrespective of whether the variable is statistically significant or not. Therefore, it is possible to have models with large  $R^2$  values and yet have poor predictions [17]. Alternatively, the *adjusted*  $R^2$  statistic can be defined as,

$$R^2_{adj} = 1 - \left( \frac{n-1}{n-k} \right) (1 - R^2) \quad (15)$$

where  $n$  is the number of simulations and  $k$  is the degrees of freedom or the number of variables assumed in the model. The  $R^2_{adj}$  will not always increase as variables are added in the model. If unnecessary terms are added, the value of  $R^2_{adj}$  will often decrease [17]. In general, it can be said that the  $R^2_{adj}$  should be close to  $R^2$  to have a good regression model.

### 2.3.4 Design of Experiments

Experimentation is a vital part of the scientific or engineering method to understand the effect of the independent variables on a response variable. The approach to planning and conducting the experiment is called the strategy of experimentation [17]. It is essential to design an experiment carefully, to extract the maximum information from the experiment. Note that in the context of Design of Experiments, the term experiment include both physical laboratory-based tests and reference numerical simulations.

One approach to design an experiment is to vary one factor at a time and evaluate the response of the system. However, this approach is inferior while studying multiple factors since it cannot model the interaction effects between the different factors. This can be achieved with a class of

experimental designs known as factorial designs. In a factorial design, multiple parameters are varied at a time, in addition to be varied one at a time.

The  $2^k$  factorial design is one such design where  $k$  is the number of factors. Figure 2.14, taken from [17] illustrates the  $2^3$  factorial design for three independent factors A, B and C. Eight experiments are required to capture the individual and interaction effects. The experimental points are shown as black dots (vertices) in Figure 2.14(a) and in matrix form in Figure 2.14(b). As shown in the figure, only the extreme values of the factors are captured with this design; therefore, the resulting response surface would be linear in nature.

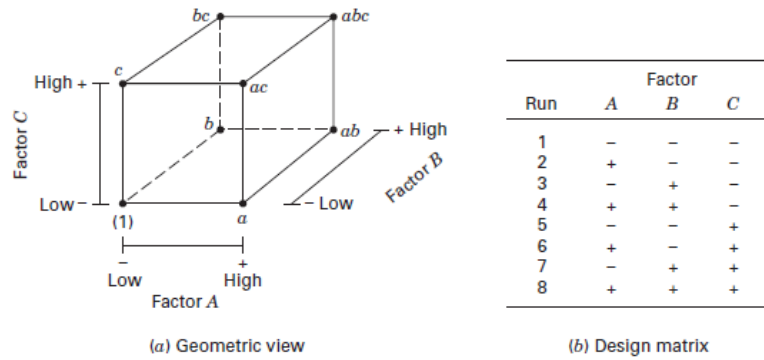


Figure 2.14:  $2^3$  factorial design and respective design matrix [17]

If it is assumed that the response of the system is quadratic in nature, a second order factorial design can be used to capture the quadratic behaviour. Several methods are available, such as, the  $3^k$  factorial design, Box-Behnken design, Central Composite design etc. The Central Composite Design (CCD) for two and three factors are illustrated in Figure 2.15.

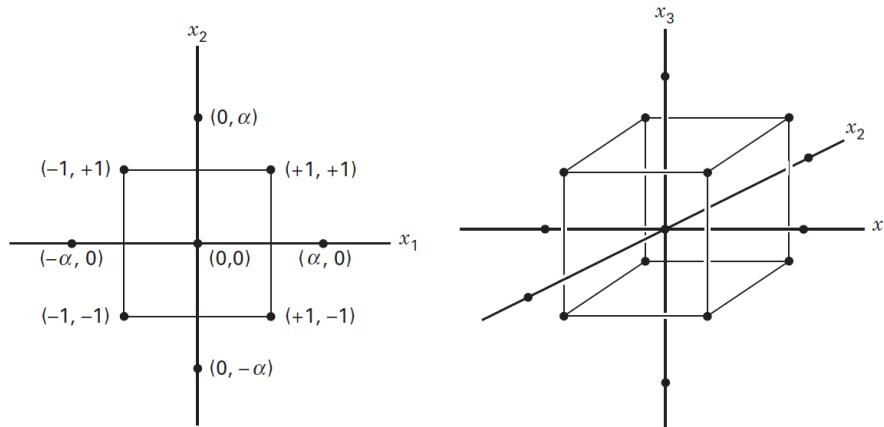


Figure 2.15: Central Composite Design (CCD) for two and three factors [17]

In addition to  $2^k$  factorial runs,  $2*k$  axial or star runs and  $n_c$  center runs form a central composite design. For one center point ( $n_c = 1$ ) and  $k$  factors, the number of CCD runs are  $2^k + 2*k + 1$ . The star points can be chosen by specifying the parameter  $\alpha$ , which depends on the Region of Interest (ROI). If the ROI is well defined,  $\alpha$  can be set to 1 forming a face centered design. If

the ROI is not clearly defined,  $\alpha$  can be set to be greater than 1. If additional accuracy is required within the ROI,  $\alpha$  can be set to be less than 1. The case when  $\alpha = 1$  is shown in Figure 2.16.

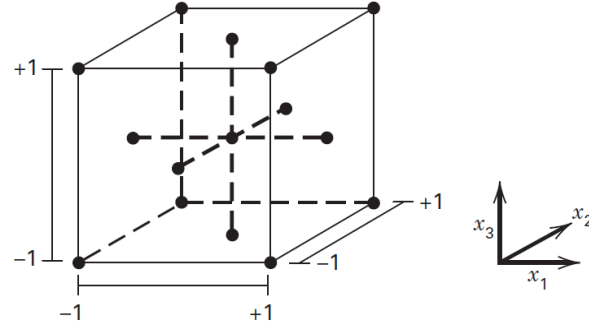


Figure 2.16: CCD for three factors when  $\alpha = 1$  [17]

If the response of the system needs to be approximated with additional accuracy over the entire design space, experiments can be modelled with space filling designs. One such design is the Latin Hypercube Design. If  $n$  runs are needed for  $k$  factors, then a Latin Hypercube design yields  $n \times k$  matrix. Each column represents a variable  $X = [x_1 \ x_2 \ \dots \ x_n]^T$  and each row represents a sample  $x_i = [x_i^{(1)} \ x_i^{(2)} \ \dots \ x_i^{(k)}]$ . The points are chosen such that each of the  $k$  factors is divided into  $n$  equal levels and there is only one point (or sample) at each level [18]. Due to this, the design space is filled out more evenly. A Latin Hypercube design for 10-runs and two factors is shown in Figure 2.17. Since it is a sampling procedure from a design space, it can also be called as Latin Hypercube Sampling (LHS).

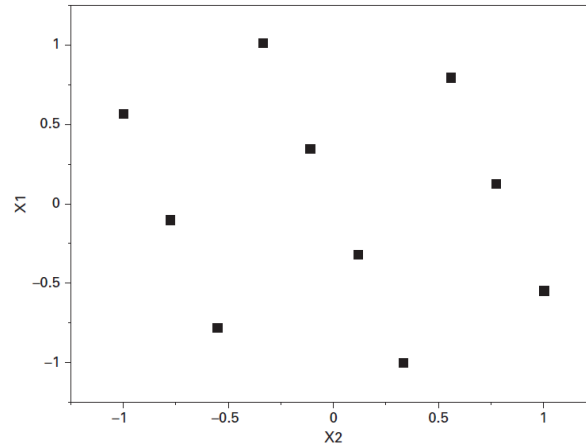


Figure 2.17: Illustration of a 10-run Latin Hypercube Design for two factors [17]

Mathematical models such as regression models discussed in the previous section can be trained with experimental points from factorial designs or space filling designs. These models are used to mimic the system behaviour within the considered design space. Such models are known by several names, such as, surrogate model, transfer function etc. The CCD and LHS approaches are used in this thesis work to build a surrogate model, which is discussed further in Section 6.3.

### 2.3.5 Empirical distribution function

Empirical cumulative distribution functions (eCDF) are used in conjunction with non-parametric regression models, and are widely employed in survival and reliability analysis [19]. If a sample of observations  $Y_1, \dots, Y_n$  is assumed to follow a distribution function  $F$ , the empirical distribution function computed at a given real number  $y$  is

$$F_n(y) = n^{-1} \sum_{i=1}^n I(Y_i \leq y) \quad (16)$$

where  $I(Y_i \leq y)$  is an indicator function assuming the value 1 if  $Y_i \leq y$  and 0 otherwise [19]. The step size in an empirical distribution function is  $1/n$  and for large sample sizes, the empirical distribution function converges to the underlying cumulative distribution function. The eCDF will be used to compare results from various cases of Monte Carlo simulations. The Monte Carlo simulation process is discussed in Section 6.

### 3 Weld measurements

In the first phase of the current work, measurements of various weld geometric parameters are collected from typical GKN products. The data is obtained from two sources: geometric non-conformance reports and weld qualification reports.

The base material, the type of welding process, and the reported edge offset are noted. The reported edge offset is later normalized by the nominal thickness of the joining plates.

From the non-conformance reports, for each reported case, the weld is first classified in one of the four cases shown in Section 2.1.3. The profilograph measurements are used to obtain the geometric parameters  $\theta$  and  $f$ , see Figure 2.4 and Figure 2.5. From the weld qualification data, the weld toe radii are measured using NIS-Elements software. Measurements of other weld geometric parameters listed in Table 2.1 are also collected.

A summary of the compiled data along with the spread of different parameters is explained in Appendix II. The compiled data is used to set bounds for the weld geometric parameters, for the various analysis performed in this work. Since the compiled information is GKN proprietary data, Appendix II is not attached with the thesis report.

## 4 Analysis Setup – Stress analysis and Life evaluation

The analysis procedure followed in the thesis to predict the fatigue life of a welded joint consists of six steps as illustrated in Figure 4.1. In essence, it involves a stress analysis incorporating the local weld geometry followed by a crack propagation analysis using the resulting stress field. The stress analysis, as shown in Figure 4.1, is carried out in Ansys APDL 2022R1. A Finite Element (FE) analysis of the local weld geometry is performed and the stress gradients are extracted. The stress gradients then serve as an input for the next three steps, in which, fatigue crack growth calculations are conducted in NASGRO 9.1 to predict the fatigue life. Each step is discussed in detail in Sections 4.1 and 4.2.

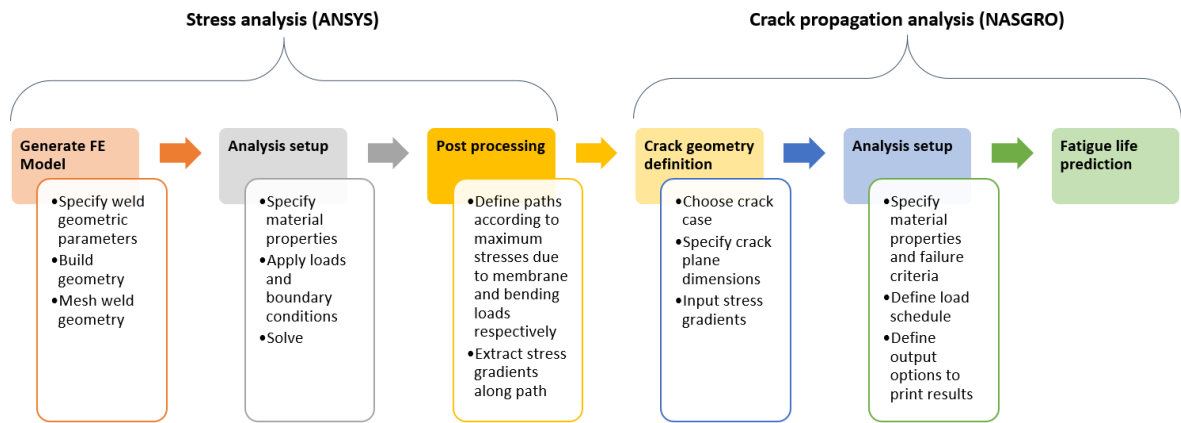


Figure 4.1: Illustration of steps involved in the fatigue life prediction of a welded joint

### 4.1 Stress analysis

#### 4.1.1 Geometry Creation

As mentioned in Section 2.1.3, three local weld geometry cases: idealized (Figure 1.2), Case 1 (Figure 2.4) and Case 2 (Figure 2.5) are included within the scope of this thesis work. A 2D weld geometry is modelled for the FE analysis. An APDL script, available from previous work, can only create the idealized geometry (Figure 1.2). In order to construct the local deformed geometries shown in Figure 2.4 and Figure 2.5, two new APDL scripts are written. These APDL scripts generate and mesh the weld geometry, perform the FE calculation and extract the stress gradients.

The parameters and their values used to define the weld geometries are listed in Table 4.1. The length parameters are normalized by the plate thickness. The weld geometry parameters are chosen such that it represents a typical TIG weld geometry. The normalized edge offset ( $e/t$ ), angular deflection ( $\theta$ ) and the length factor for the extent of the angular deflection ( $f$ ) are varied within bounds that were obtained from collected non-conformance data as discussed in Section 3.



Table 4.1: List of parameters and values used for the analysis

<i>Parameter</i>	<i>Value</i>	<i>Description</i>
$t1$	4 [mm]	Thickness of plate #1
$t2$	4 [mm]	Thickness of plate #2
$B$	3.275	Normalized bead width on the top side
$Bh$	$0.15*B$ [mm]	Weld bead height on the top side
$C$	$B$	Normalized bead width on the root side
$Ch$	$0.15*C$ [mm]	Weld bead height on the root side
$e/t$	0 – 0.41	Normalized edge offset
$\phi1 - \phi4$	45 [°]	Internal weld bead angles
$L1$	30 [mm]	Length of plate #1
$L2$	30 [mm]	Length of plate #2
$R1 - R4$	10% of thickness	Weld toe radii
$\theta$	1 – 5 [°]	Local angular deflection (Case 1 and Case 2)
$f$	0.1 – 0.7	Length factor of local deflection (Case 2)

To create the geometry, the top side is constructed first followed by the root side. Illustrations of idealized (IG), Case 1 and Case 2 analysis geometries are shown in Figure 4.2.

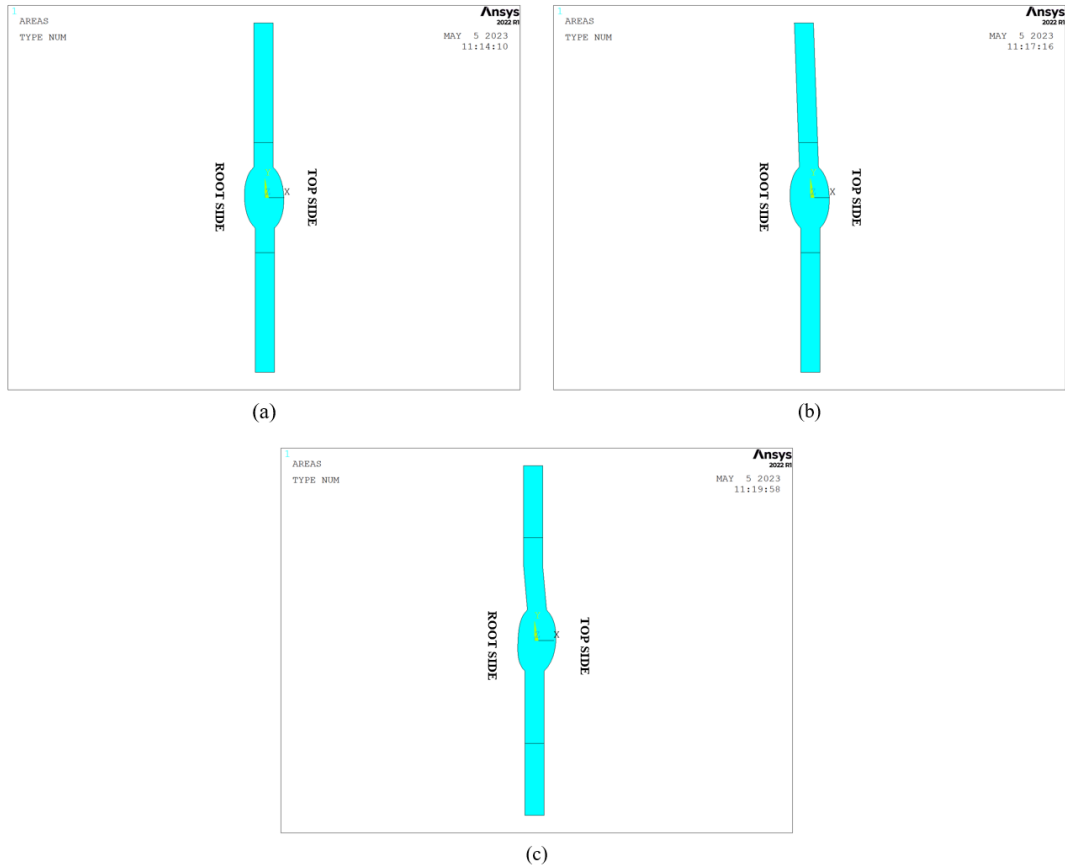


Figure 4.2: Illustration of different weld geometries (a) IG (b) Case 1 (c) Case 2

Three keypoints are used to construct the weld bead on the top side, see Figure 4.3. These are located at the two weld toe radii and the maximum bead height ( $Bh$ ). A BSPLINE curve is then fitted through the three keypoints. The same process is repeated for the root side, with corresponding bead height ( $Ch$ ).

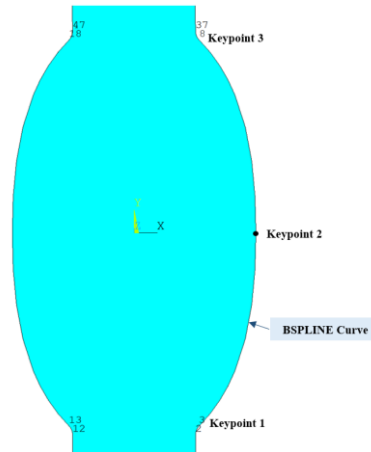


Figure 4.3: Construction of the weld bead

#### 4.1.2 Mesh and Material properties

Higher order quadrilateral elements (8-noded, Ansys type PLANE183) are used to mesh the geometry. Mesh refinement is carried out at the regions of high stress locations i.e., the weld toe radii. An illustration of the mesh is shown in Figure 4.4.

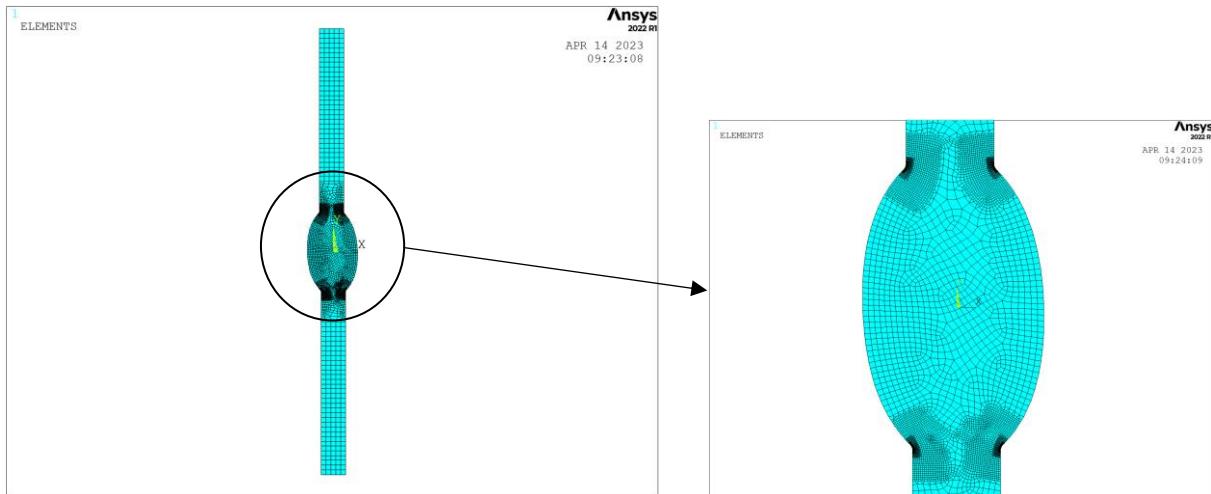


Figure 4.4: Illustration of mesh

The mesh refinement process starts by selecting the nodes associated with the arcs of the weld toe radii. Using the *ESLN* and *NSLE* commands the elements close to the weld toe radii are selected. Using the *SMRTSIZE* and *EREFINE* commands, a mesh refinement is done on the selected elements. To achieve an adequately fine mesh the above steps are repeated multiple times. The script followed for the mesh refinement process is shown in Appendix 10.1. A mesh convergence study is carried out and the obtained results are shown in Figure 4.5 and Table 4.2.

The loads and boundary conditions used in the convergence study are similar to those used in the main work of the thesis; see Section 4.1.3 (Figure 4.6 and Figure 4.7).

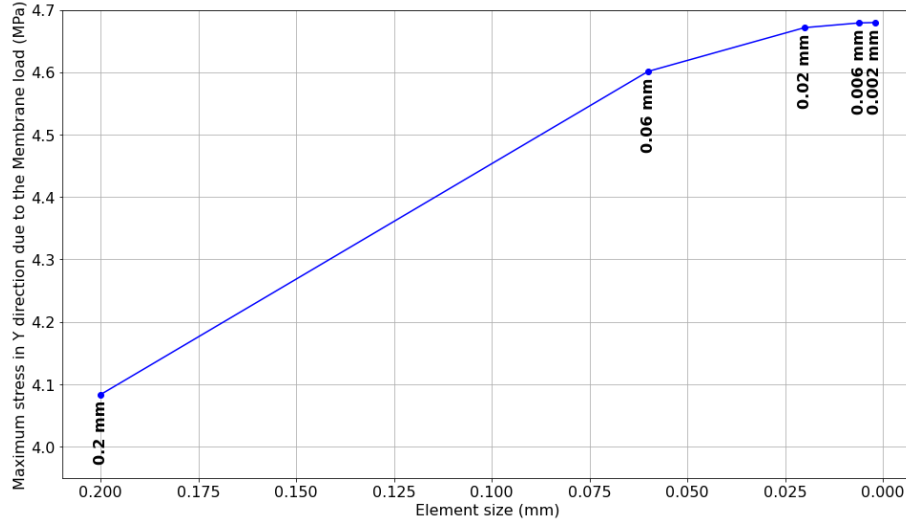


Figure 4.5: Mesh convergence study

Under unit membrane load (1 MPa tensile), the maximum observed stress converges for an element size of 0.006 mm. Therefore, for further analysis an element size of 0.006 mm is used.

Table 4.2: Results from mesh convergence study

<i>Element size (mm)</i>	<i>Maximum stress in Y direction due to Membrane load (MPa)</i>
0.2	4.10839
0.06	4.60733
0.02	4.67162
0.006	4.67901
0.002	4.67958

A study is carried out to evaluate the differences between plane stress and plane strain conditions and the obtained results are tabulated in Table 4.3. The analysis is carried out for Case 2 geometry with  $\theta$  set to  $5^\circ$  and  $f$  set to 0.7. Two load cases: unit membrane and bending loads with boundary conditions as discussed in Section 4.1.3 are analysed.

Table 4.3: Results for plane stress and plane strain conditions - Case 2 geometry [ $\theta = 5^\circ$ ;  $f = 0.7$ ]

<i>Condition</i>	<i>Load</i>	<i>Maximum observed stress (MPa)</i>					
		SX	SY	SZ	S1	S2	S3
Plane stress	Membrane	1.434	4.679	0	4.827	0.600	0
	Bending	0.574	1.957	0	2.004	0.245	-1.925
Plane strain	Membrane	1.434	4.679	1.651	4.827	1.651	0.600
	Bending	0.574	1.957	0.685	2.004	0.685	-1.925

As expected, the out of plane stresses (SZ) are zero for plane stress condition, while they are non-zero for plane strain condition. Moreover, the in-plane stresses (SX and SY) do not change between plane stress and plane strain conditions. The maximum principal stress (S1) remains unchanged between the two conditions. It is also observed that the stress gradients extracted (discussed in Section 4.1.4) do not change for the two conditions. For further analysis, the plane stress condition will be used. Linear elastic material properties that correspond to Inconel 718 (IN718) [20] are used in the analysis as listed in Table 4.4.

Table 4.4: Material properties used in the analysis [20]

<i>Parameter</i>	<i>Value</i>
Young's modulus ( $E$ )	199.94e3 [MPa]
Poisson's ratio ( $\nu$ )	0.294

### 4.1.3 Loads and boundary conditions

The boundary conditions used in the analysis is shown in Figure 4.6. All the nodes on the edge of one of the joining plates as highlighted are fully constrained in all degrees of freedom. The analysis consists of two load steps and the magnitude of the applied loads is listed in Table 4.5.

Table 4.5: Applied loads for the analysis

<i>Applied load</i>	<i>Magnitude</i>
$\sigma_m$	1 [MPa]
$\sigma_b$	1 [MPa]



Figure 4.6: Fixed constraint applied to the highlighted edge of the model

In the first step, a membrane load ( $\sigma_m$ ), as shown in Figure 4.7(a), is applied as a (negative) pressure load using the *SFL* command. In the second step, a bending load ( $\sigma_b$ ), as shown in Figure 4.7(b), is applied through a force couple. The magnitude of force to be applied can be determined as follows. The stress in a beam under simple bending is,

$$\sigma_b = \frac{M * z}{I} \quad (17)$$

where  $M$  is the bending moment about the neutral axis,  $z$  is the perpendicular distance from the neutral axis and  $I$  is the second moment of area of the beam cross-section. Given a force couple acting at the end of a rectangular beam, the expressions for  $M$ ,  $z$  and  $I$  can be written as

$$M = F * t \quad ; \quad z = \frac{t}{2} \quad ; \quad I = \frac{bt^3}{12} = \frac{t^3}{12} \quad (18)$$

where  $F$  is the magnitude of the force couple,  $t$  is the thickness of the joining plates and  $b$  is the breadth of the beam cross-section. Substituting Equations (18) in (17) and rearranging, the magnitude of the force couple is given as,

$$F = \pm \frac{1}{6} (\sigma_b * t) \quad (19)$$

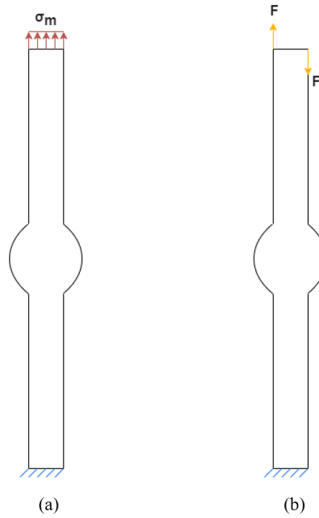


Figure 4.7: Illustration of the two load steps (a) Load step 1 – Membrane (b) Load step 2 – Bending

A study is carried out to evaluate differences between small and large deformation analysis. The analysis is performed with Case 1 geometry with  $\theta$  set to  $1^\circ$ . The large deformation effects can be toggled in APDL with the *NLGEOM* command. A membrane load is varied from 1 MPa to 100 MPa and the resulting maximum stress in Y direction is evaluated. Figure 4.8 shows two curves for analysis results with large deformation effects (*NLGEOM* = ON) and without large deformation effects (*NLGEOM* = OFF).

It is observed that the maximum stress with large deformation effects begins to deviate from small deformation analysis for an applied membrane load of approximately 40 MPa. The stress gradients for a membrane load of 1 MPa and 100 MPa, with and without considering large deformation effects, is shown in Figure 4.9(a) and Figure 4.9(b) respectively. For a membrane load of 100 MPa, a slight increase in the peak stress is observed by including large deformation

effects. However, to facilitate scaling of stress gradient with respect to applied load, small deformation is assumed for further analysis.

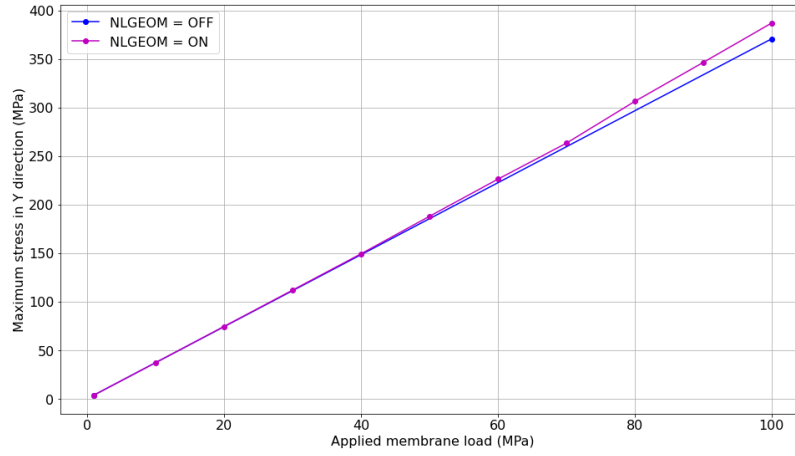


Figure 4.8: Effect of large deformation on peak stress

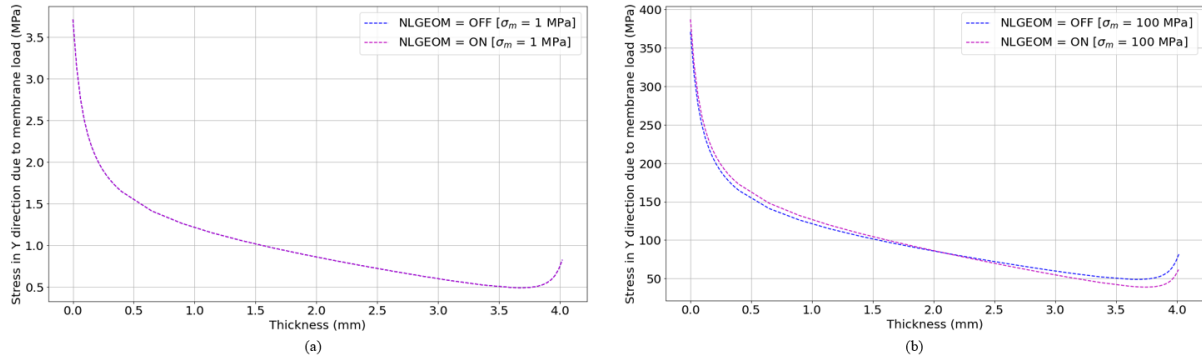


Figure 4.9: Effect of large deformation on stress gradient (a) Membrane load = 1 MPa (b) Membrane load = 100 MPa

#### 4.1.4 Stress gradient extraction

For the crack propagation analysis, it is assumed that an initial crack is present at the weld toe radius where the maximum stress occurs, as illustrated in Figure 4.10(a). Assuming mode I failure, the stresses normal to the crack plane are required, which corresponds to the global  $Y$ -direction in the FE analysis. Therefore, from the results of the FE analysis, stresses in the global  $Y$ -direction are evaluated.

In the idealized geometry, the maximum stress due to both the membrane and bending loads occurs at the same weld toe radius. However, considering the real geometry it is observed that the maximum stress locations due to membrane and bending load can be different as shown in Figure 4.10(b). It is assumed that the crack can propagate from either of the two maximum stress locations. Therefore, two life calculations are performed at the respective maximum stress locations and the minimum life from the pair is considered.

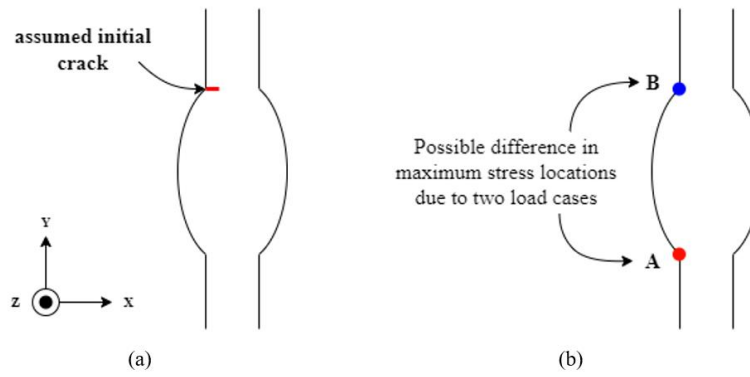


Figure 4.10: Illustration of (a) assumed initial crack for crack propagation analysis (b) Difference in maximum stress locations due to membrane and bending loads

The stress gradients from the FE analysis are extracted as follows. The node where the maximum stress occurs is identified and a local coordinate system is defined at the location for path definition, as shown in Figure 4.11. Four points are used to define the path for stress gradient extraction. Two points are defined close to the edges of the plates ( $1/10$  of thickness from either side) to capture the steep gradients in the stress gradients. Note that the stresses are extracted at 12 equispaced intermediate points between each of the points that define the path, namely, points 1, 2, 3 and 4 in Figure 4.11.

The crack propagation analyses are conducted assuming that the crack takes the shortest way to the opposite boundary [8]. For this purpose, when necessary, the defined local coordinate system is rotated by the respective angular deflection, as shown in Figure 4.11(b). The stresses are always extracted in the global Y-direction along the path, since only small angular deflections ( $1^\circ - 5^\circ$ ) are investigated. During the numerical extraction process, the length of the path can slightly deviate from the plate thickness. In order to maintain consistency the path length is limited to the thickness of the plate in the crack propagation analyses. The stress gradients due to both membrane and bending loads are extracted along the defined paths.

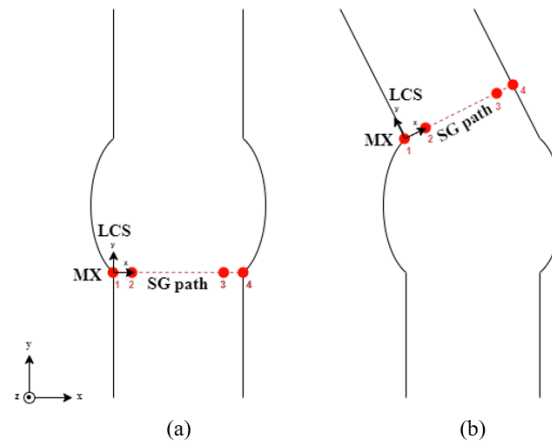


Figure 4.11: Illustration of path definition for stress gradient extraction (a) Max stress at a location such that the crack grows along the global X-direction (b) Max stress at a location such that crack growth deviates from the global X-direction

### 4.1.5 Forward and reverse bending

As discussed before, locally on the weld joint two bending stresses appear. The sketches shown in Figure 4.12 can be used to illustrate this point. The first one is the global bending moment, which is shown as moment  $M$  in the figure. The second one, local to the weld joint, is the secondary bending moment caused by the membrane load  $F$  due to presence of the edge offset ( $e$ ). Depending on the ‘direction’ of the offset, these two moments can combine together or oppose each other (see top and bottom sketches in Figure 4.12). These cases are called forward and reverse bending, respectively. The two cases are accounted for in the analysis performed in this thesis work. Conditions followed for the deterministic analysis is discussed in Section 4.3.1 and Monte Carlo simulations are discussed Section 6.3.

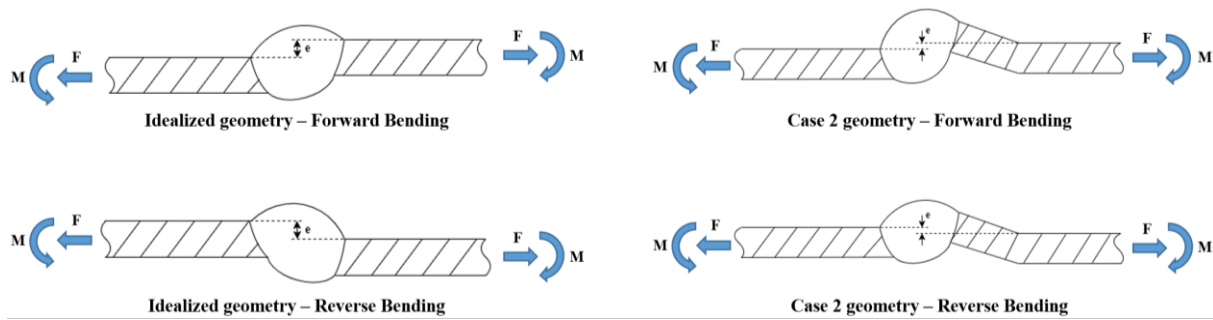


Figure 4.12: Illustration of forward and reverse bending scenarios in IG and Case 2 geometries

## 4.2 NASGRO Life calculation

The *NASFLA* (Fatigue Crack Growth) module within NASGRO 9.1 is used to perform the crack growth calculations. A detailed description of the steps followed as shown in Figure 4.1 is discussed below.

### 4.2.1 Crack geometry

There are several crack geometries available within the *NASFLA* module. The surface crack (SC30) geometry as shown in Figure 4.13, is chosen for the crack propagation analysis. The crack geometry can take up-to four univariant stress gradients as input. Therefore, the two 1D stress gradients (corresponding to unit membrane and unit bending load) obtained from the FE analysis can be provided as an input for the crack growth calculations.



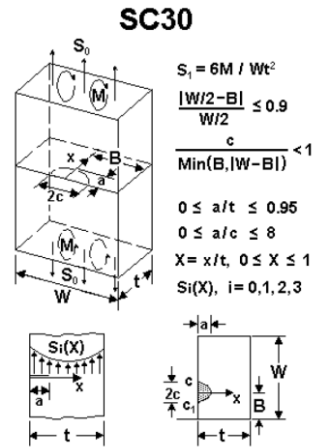


Figure 4.13: SC30 crack geometry [10]

The crack plane dimensions used for the analysis are listed in Table 4.6. According to the current NDT practices in the aerospace industry the minimum crack length that can be detected with confidence is approximately 1.52 mm, which corresponds to the  $2c$  dimension in Figure 4.13. With the  $a/c$  ratio assumed to be 1, the initial crack depth is considered as 0.76 mm for the crack propagation analysis.

Table 4.6: Crack plane dimensions used for crack propagation analysis

<i>Parameter</i>	<i>Value</i>	<i>Description</i>
$t$	4 [mm]	Thickness
$W$	15 [mm]	Width
$B$	7.5 [mm]	Crack centreline offset
$a$	0.76 [mm]	Initial crack size
$a/c$	1	Initial $a/c$ ratio

## 4.2.2 Material properties and failure criteria

Material properties that correspond to Inconel 718 (IN718) are chosen from the NASGRO material database for the crack propagation analysis. The material chosen is - *Inconel 718; STA(1700F, - -) Plt & Forg; -100F to 400F Air* (NASGRO curve ID Q3LB23AB1) and the material properties correspond to room temperature data. The Paris law parameters for the selected material are listed in Table 4.7.

Table 4.7: Paris law parameters of IN718 for crack propagation analysis

<i>Parameter</i>	<i>Value</i>
$C$	$2.054\text{e-}14 \left[ \frac{\text{mm}}{(\text{MPa}\sqrt{\text{mm}})^n} \right]$
$n$	3.50

A failure or crack instability is assumed to occur when the  $K_{max}$  value exceeds the fracture toughness of the material ( $K_c$ ). While other modes of failure such as net section stress exceeding the flow stress of the material is also available within NASGRO, only the fracture toughness is considered as a failure criteria for the current thesis work.

### 4.2.3 Load blocks

According to the nomenclature followed within NASGRO for the SC30 crack case, S0 and S1 stresses will be used for the analysis. The S0 stress correspond to membrane load and the S1 stress correspond to bending load. The loads in NASGRO are defined with three quantities: the spatial variation of stresses, time varying stresses and the stress scale factors. The spatial variation of stresses, which act at the crack plane correspond to the stress gradients (SG) that are obtained from the FE analysis, which are extracted through the thickness, as explained in Section 4.1.4. The stress gradients due to unit membrane and unit bending loads along the crack path (starting from the crack origin) are shown in Figure 4.14. The distance from the center of the initial crack is normalized by the plate thickness. These spatial gradients constitute one input to NASGRO.

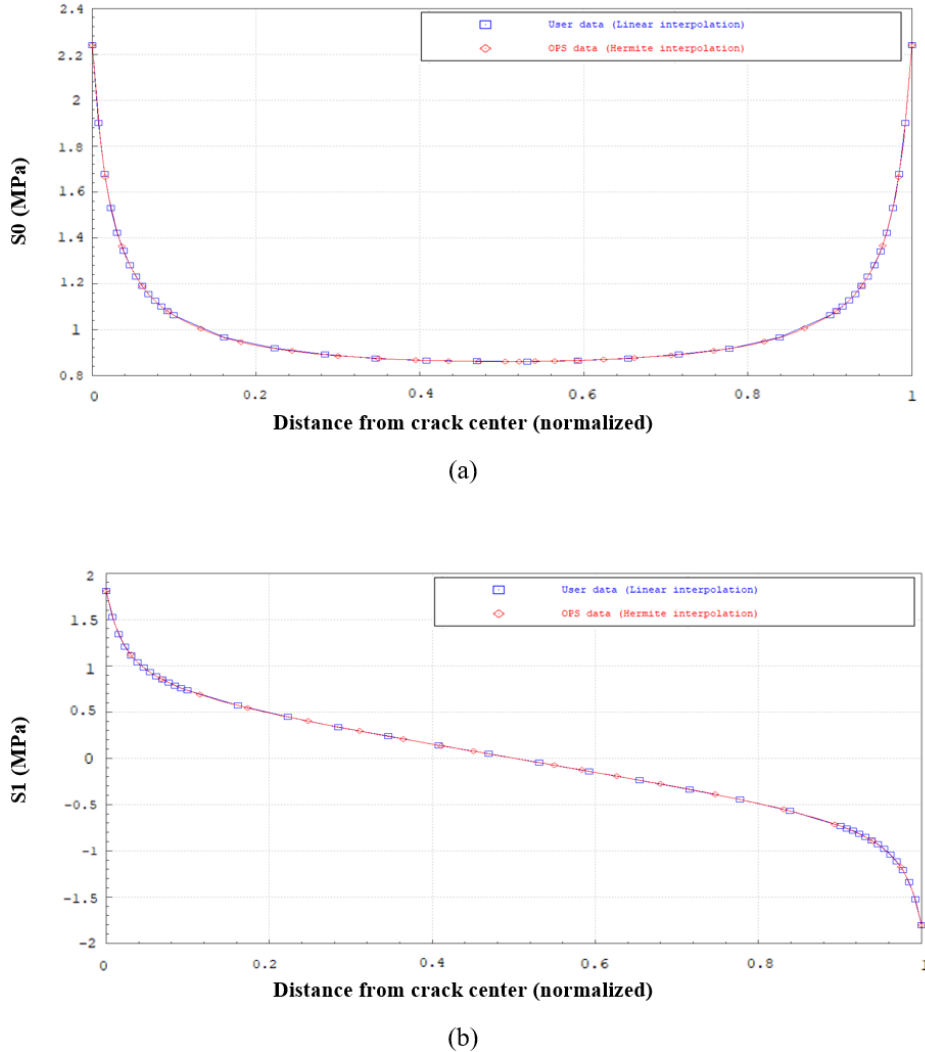


Figure 4.14: Stress gradients input in NASGRO (a) due to membrane load (S0) (b) due to bending load (S1)

For the time varying stresses, a simple fatigue stress cycle (Fat\_load) is considered for the analysis. The fatigue stress cycles for both the S0 and S1 stresses are considered to oscillate between 0 to 100 MPa as shown in Figure 4.15. The fatigue stress scale factors (scl\_fac) for both S0 and S1 is set to 1.

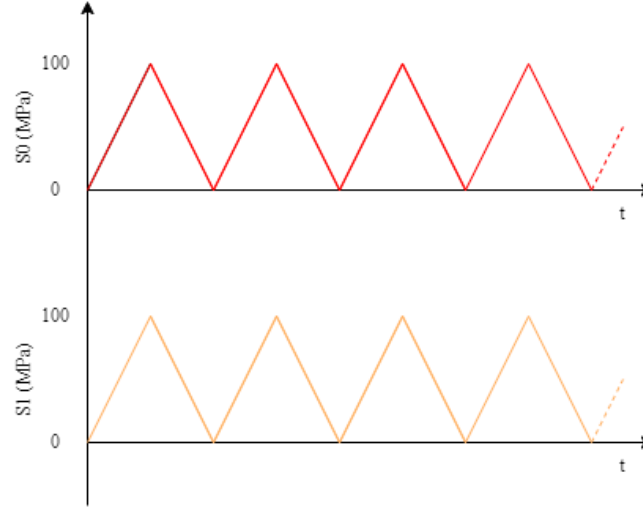


Figure 4.15: Fatigue stress cycles used for the crack propagation analysis

The total stress that would act on the crack at any given time point during the analysis is then, a superposition of both S0 and S1 loads, which can be expressed as,

$$\begin{aligned} \text{Total stress at a time point} = & (Fat\_load_{S0} * SG_{S0} * scl\_fac_{S0}) \\ & + (Fat\_load_{S1} * SG_{S1} * scl\_fac_{S1}) \end{aligned} \quad (20)$$

### 4.3 Automation

The analysis process shown in Figure 4.1 is automated through a combination of APDL and Python scripts. The main purpose of the automation is to carry out multiple analyses by varying the three weld geometry parameters ( $e/t$ ,  $\theta$  and  $f$ ), within the bounds listed in Table 4.1. This automation is the main enabler for the Monte Carlo analysis carried out in the thesis (discussed in Chapter 6 and 7). The process followed to evaluate fatigue life for an individual case has been discussed in Sections 4.1 and 4.2. The workflow employed to automate the process is explained in the following sections.

#### 4.3.1 Automation – Stress gradient extraction

Based on the results discussed in Section 5.1, the Case 1 geometry is not considered for the automation process. The idealized geometry and Case 2 geometry (referred as the real geometry in the automation process) are considered, and Figure 4.16 shows the algorithm followed in extracting the stress gradients from the FE analysis. Two APDL scripts execute the steps shown in the algorithm.

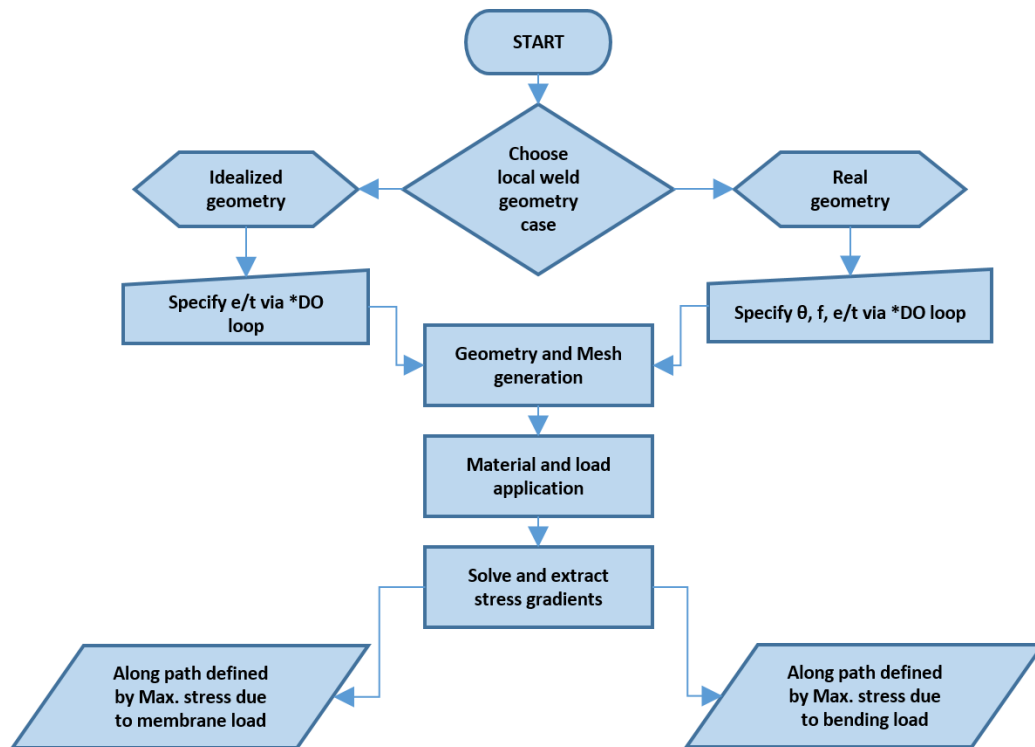


Figure 4.16: Algorithm of steps followed to extract stress gradients

The process starts with choosing the type of the local geometry. If idealized geometry is chosen, the range of normalized edge offset ( $e/t$ ) to be simulated is specified via a *\*DO* loop. If the real geometry is chosen, the ranges of three parameters: normalized edge offset ( $e/t$ ), angular deflection ( $\theta$ ) and the length factor ( $f$ ) are specified via a *\*DO* loop. The weld geometry and mesh is generated with the specified parameters, with the first APDL script. Using the second APDL script, the analysis is performed with conditions as described in Section 4.1. For the deterministic analysis (results discussed in Chapter 5), both the unit membrane and unit bending loads are applied in such a way that the global bending moment and the secondary bending moment at the weld region act in the same direction (see Section 4.1.5 for explanation). From the results of the FE analysis, the stress gradients along paths defined by maximum stresses due to membrane and bending loads are extracted as discussed in Section 4.1.4.

### 4.3.2 Automation – Life evaluation

An algorithm of the steps followed in evaluating the fatigue life with NASGRO is shown in Figure 4.17. Two Python scripts are written to perform the steps shown. The first Python script creates the NASGRO input files and the second Python script performs the NASGRO runs and extracts the fatigue life.

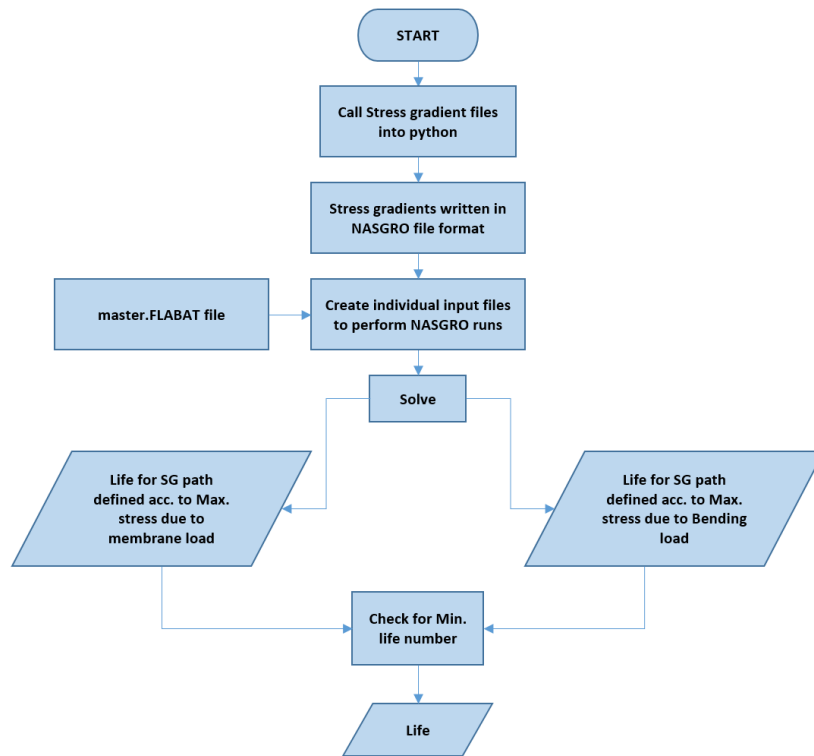


Figure 4.17: Algorithm of steps followed for evaluation of fatigue life

The process starts by calling the stress gradient files (obtained from FE analysis) into Python. The stress gradients are then written in NASGRO file format. Within NASGRO, the FLABAT file is used to perform batch runs. The only difference among the NASGRO input files corresponding to different cases lie in the respective stress gradient files. Therefore, a master FLABAT file that follows the structure of the standard input for the analysis is used as a template. As shown in Appendix 10.2, the stress gradient file names are inserted in the placeholders of the master file to generate individual input files. The NASGRO runs are then executed.

For every case, two lives are evaluated. The lives correspond to the two starting positions of the assumed initial crack, based on the maximum stress locations for the two load cases. The minimum of these two is taken as the life for the local weld geometry case analysed.

## 5 Results – Deterministic analysis

### 5.1 Initial Study – Case 1 geometry

For a Case 1 geometry, the length of the local angular deflection around the weld cannot be determined from the profilograph measurement, as shown in Figure 2.4. In the analysis geometry, the lengths of the two joining plates are set to  $L1$  and  $L2$ , and the local angular deflection ( $\theta$ ) measured from the profilograph measurement is applied to the plate with length  $L2$ , as shown in Figure 5.1. For the analysis both  $L1$  and  $L2$  are set to be equal. Life calculations are performed for various lengths of joining plates and the results are discussed in this section.

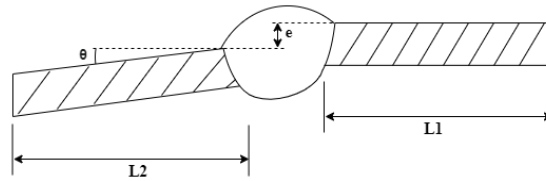


Figure 5.1: Illustration of case 1 analysis geometry

The lengths of joining plates and  $\theta$  as listed in Table 5.1, are used for the analysis. Other weld geometry parameters are set to values listed in Table 4.1.

Table 5.1: List of parameters used for Case 1 geometry analysis

<i>Parameter</i>	<i>Value</i>	<i>Description</i>
$\theta$	1 [°]	Local angular deflection
$L1, L2$	30, 40, 50 [mm]	Length of individual plates ( $L1 = L2$ )

Figure 5.2(a) shows that the maximum stress occurs on the root toe radius where the local angular deflection is present. Moreover, as the length of the joining plates increase the maximum observed stress due to membrane load increases linearly as shown in Figure 5.2(b).

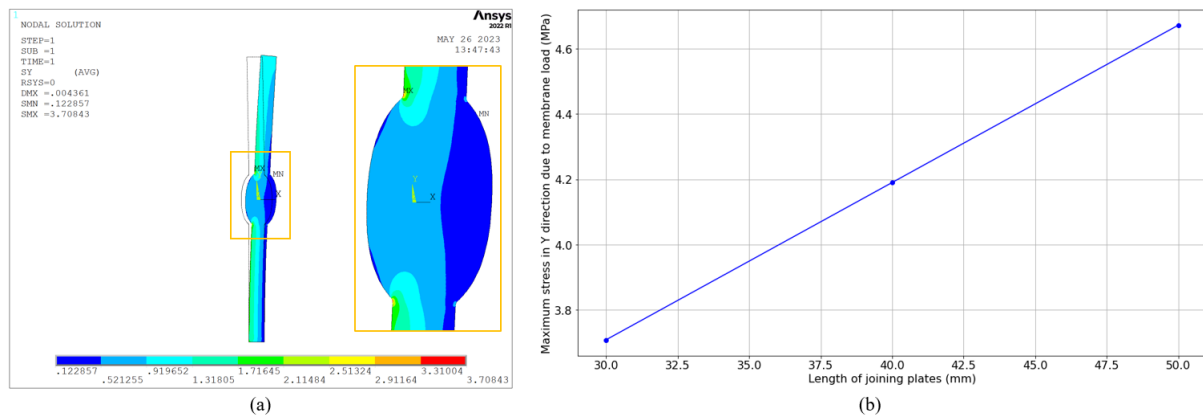


Figure 5.2: Results from FE analysis of case 1 geometry [ $\theta = 1^\circ$ ] (a) Stress distribution (in MPa) around weld region due to membrane load (1 MPa), plate length = 30 mm (b) Maximum stress in Y-direction due to membrane load as a function of the length of the plates

It is observed that as the length of the joining plates increase, it results in a significant drop of the fatigue life, as shown in Figure 5.3. The fatigue life reduces from a maximum observed value of 381849 cycles (plate lengths = 30 mm) to 190065 cycles (plate lengths = 50 mm) under a given membrane load of 1 MPa.

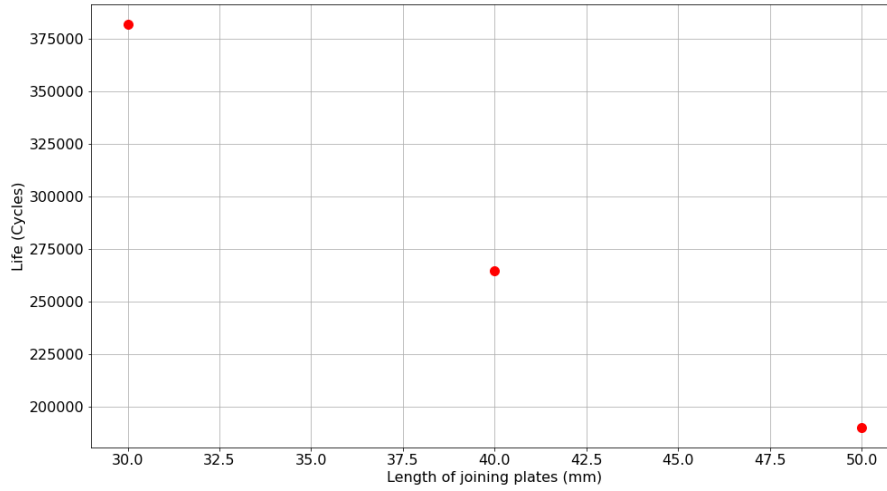


Figure 5.3: Length of joining plates vs observed life for case 1 geometry [ $\theta = 1^\circ$ ]

As the length of the plates increase the perpendicular distance between the point of load application and weld centreline increases. This causes an increase in the local bending moment at the weld joint, which is illustrated in Figure 5.4, resulting in a reduction of life.

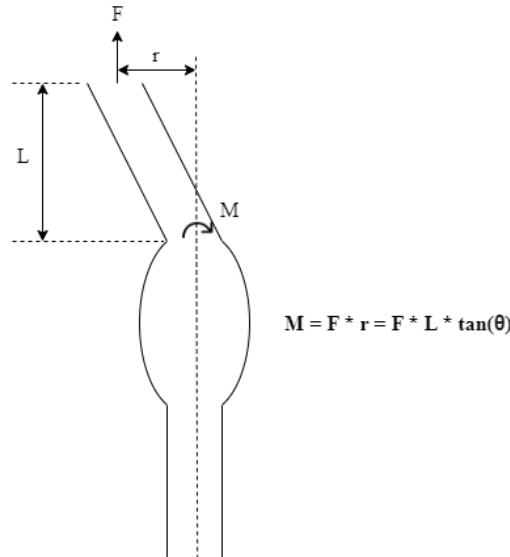


Figure 5.4: Illustration of higher moment resulting in reduction of fatigue life in case 1 geometry

However, in reality, local angular distortions do not exceed more than one bead width. The case 1 geometry therefore, does not represent a local geometry, and is out of the scope of current work. For further analysis, only the idealized geometry and Case 2 geometry (henceforth referred as the real geometry) are considered. The results obtained for the respective cases are discussed in the following sections.

## 5.2 Fatigue life results - Idealized Geometry

In an idealized geometry, the edge offset ( $e$ ) is considered between two parallel plates, as illustrated in Figure 1.2. The normalized edge offset ( $e/t$ ) is varied within bounds (0 – 0.41) that are set according to the data collected from non-conformances as discussed in Section 3. Other weld geometry parameters were set to values listed in Table 4.1.

The stress distribution due to membrane load for two cases of normalized edge offset are shown in Figure 5.5. For the case of no edge offset, the maximum stress can occur at either of the four weld toe radii, as shown in Figure 5.5(a). However, in the presence of an edge offset the maximum stress shifts to the lower root toe radius as shown in Figure 5.5(b).

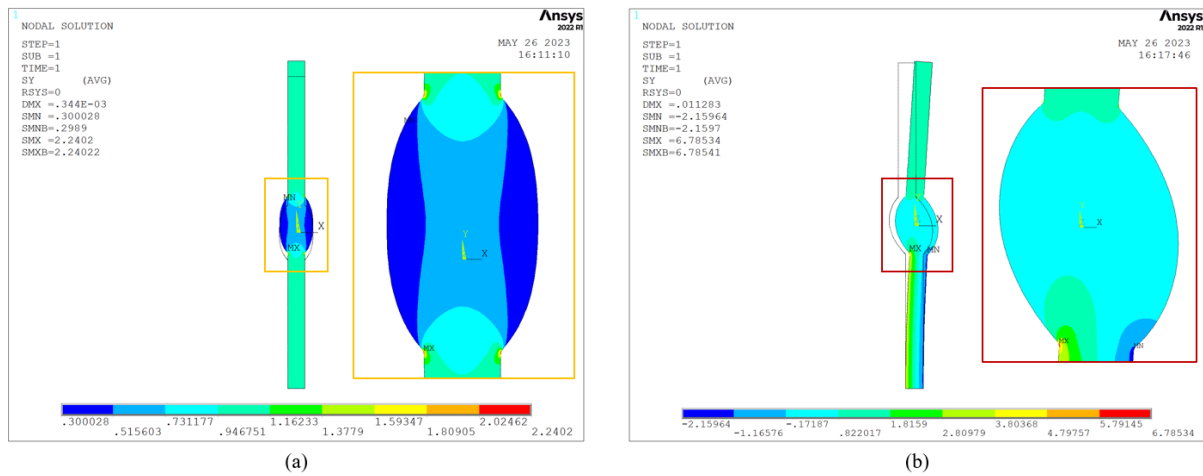


Figure 5.5: Stress distributions (in MPa) around weld region due to membrane load (1 MPa) for an idealized geometry (a)  $e/t = 0$  (b)  $e/t = 0.41$

Figure 5.6 shows the effect of normalized edge offset on the resulting fatigue life. It is observed that an increase in edge offset results in a significant reduction in the fatigue life. This is because, an increase in the edge offset leads to an increase in the local bending moment caused at the weld joint, resulting in a drop in the calculated fatigue life.

In order to generate the data shown in Figure 5.6, stress analysis and life calculations are carried out through the automation scripts. The small non-monotonic excursions on the curve are considered effect of non-identical mesh.



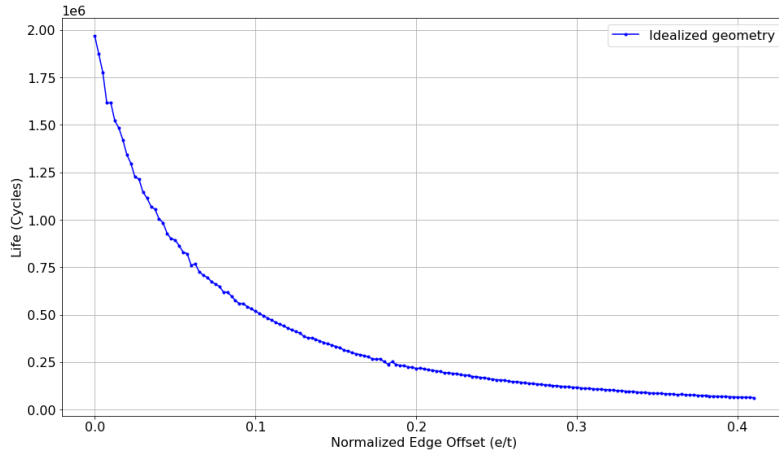


Figure 5.6: Normalized edge offset vs fatigue life for idealized geometry [ $t = 4\text{mm}$ ]

### 5.3 Fatigue life results - Real geometry

The geometric parameters of a real geometry (see Figure 2.5) are varied within bounds that are set according to data collected from non-conformance reports as discussed in Section 3. The values of respective parameters that are used for the analysis is listed in Table 5.2. Other weld geometry parameters are set to values listed in Table 4.1.

Table 5.2: Bounds for parameters of real geometry used for deterministic analysis

<i>Parameter</i>	<i>Value</i>	<i>Description</i>
$e/t$	0 – 0.4	Bounds for normalized edge offset
$\theta$	1 - 5 [ $^\circ$ ]	Bounds for local angular deflection
$f$	0.1 – 0.7	Bounds for length factor of local deflection

The effect of normalized edge offset on the fatigue life is shown in Figure 5.7. The life curves of the real geometry (RG) correspond to a specific case for a local angular deflection ( $\theta$ ) of  $2^\circ$  and the length factor ( $f$ ) is varied within the bounds. The life curves of the real geometry are overlaid on the life curve of idealized geometry for comparison.

Consider two cases of the real geometry, as shown in Figure 5.8. When no edge offset is present, as illustrated in Figure 5.8(a), the local distortion of length  $L3$  causes the maximum observed stress to occur at root radius location  $MX_1$ . This leads to a reduction of fatigue life. As  $L3$  increases, it induces higher stresses resulting in a further reduction of fatigue life. This is evident for the cases where the normalized edge offset is zero in Figure 5.7, where, as the value of  $f$  increases the observed life reduces.

When an edge offset is introduced in the model, as illustrated in Figure 5.8(b), it leads to an increase in stresses at root radius location  $MX_2$ , and there exists a value of edge offset above which, the maximum stress location shifts from root radius location  $MX_1$  to  $MX_2$ .

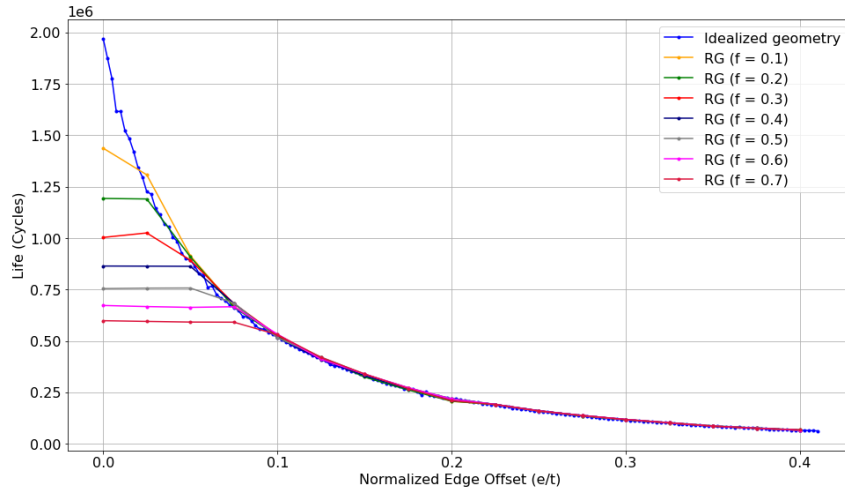
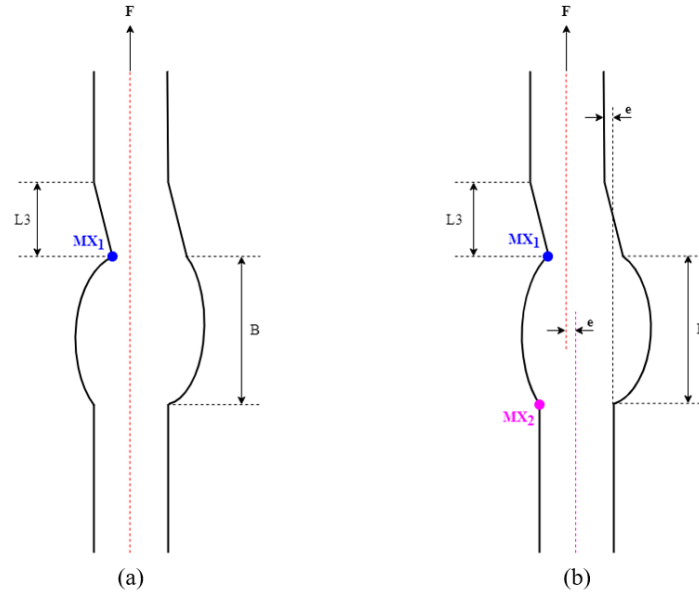

 Figure 5.7: Normalized edge offset vs fatigue life for real geometry [ $t = 4\text{mm}$ ;  $\theta = 2^\circ$ ]


Figure 5.8: Maximum stress locations in real geometry for (a) No edge offset (b) With edge offset

Therefore, for a given length of local angular deflection the fatigue life remains almost constant until a threshold value of edge offset. For higher values of edge offset, the maximum stress location shifts to  $MX_2$ , which dictates the resulting fatigue life, and both real and idealized geometries predict the same life results. This behaviour is clearly seen in Figure 5.7, where after a certain threshold value of edge offset, the real and idealized geometry yield same life numbers.

For the particular case when  $f$  is 0.6, it is observed that the fatigue life is almost constant at approximately 67000 cycles until a normalized edge offset of approximately 0.075. For higher values of edge offset, the real geometry yields approximately the same life results as the idealized geometry. The fatigue life curves for the other cases are shown in Appendix 10.3.

Figure 5.9 shows the stress distributions around the weld for the case ( $\theta = 2^\circ$ ;  $f = 0.6$ ). When the normalized edge offset is 0.025, the maximum stress occurs at location  $MX_1$ . However, for a normalized edge offset increases to 0.1, the maximum stress location shifts to  $MX_2$ .

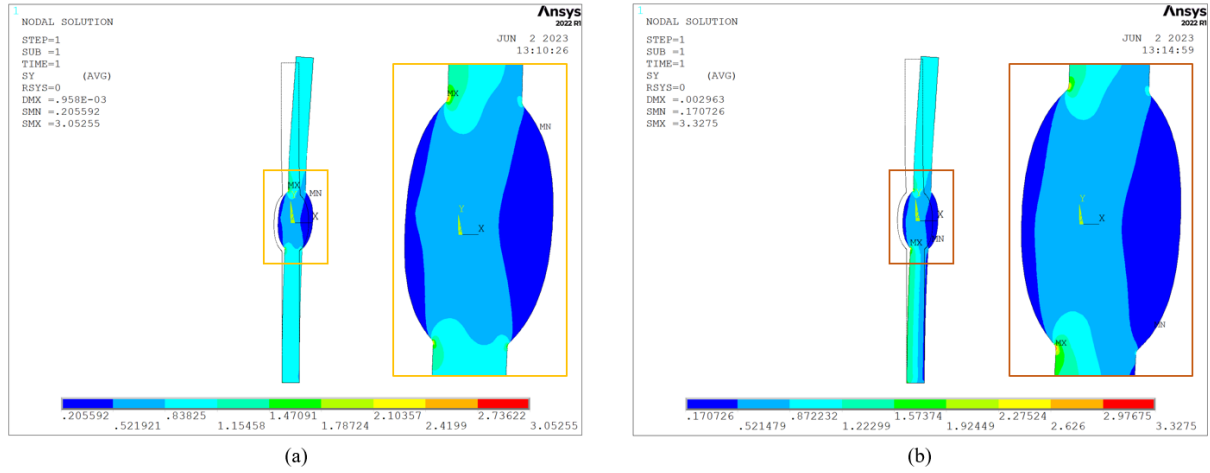


Figure 5.9: Stress distributions (in MPa) around the weld region in a real geometry [ $t = 4\text{mm}$ ;  $\theta = 2^\circ$ ;  $f = 0.6$ ] due to membrane load (1 MPa) for (a)  $e/t = 0.025$  (b)  $e/t = 0.1$

#### 5.4 Fatigue life results – Different edge offset measures

A study is carried out to investigate if it is possible to evaluate conservative life estimates using the idealized geometry instead of the real geometry with different edge offset measures.

Consider the real geometry as illustrated in Figure 5.10. Two edge offsets measures are possible. If the local distortion were ignored, it would yield a remote offset measurement ( $RO$ ). On the other hand, if the local angular deflection were considered in the measurement, one can make use of a local offset measurement ( $LO_I$ ). The idealized geometry can yield two life results depending on which offset is considered in the fatigue life evaluation. Therefore, three analysis approaches can be taken to evaluate the fatigue life with idealized and real geometries. These are real geometry (RG), idealized geometry with remote offset (IG –  $RO$ ) and idealized geometry with local offset (IG –  $LO_I$ ).

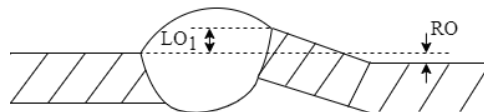


Figure 5.10: Illustration of two possible offset measurements in the real geometry

Consider a case with normalized  $RO$  and  $LO_I$  values along with other dimensions pertaining to real geometry as listed in Table 5.3. The weld geometries for the three analysis approaches are shown in Figure 5.11. The obtained life results for the respective cases are highlighted in Figure 5.17 and Table 5.3.

Table 5.3: Example 1 – Parameters of a real geometry and life results from three analysis approaches

<i>Geometry Parameters</i>	<i>Value</i>	<i>Analysis approach</i>	<i>Life (cycles)</i>
Normalized remote offset ( $RO$ )	0.05	RG	663142
Angular deflection ( $\theta$ )	2 [°]	IG – $RO$	893535
Length factor ( $f$ )	0.6	IG – $LO_I$	332399
Normalized local offset ( $LO_I$ )	0.15		

The stress gradients due to membrane load for the three cases are shown in Figure 5.12. It is observed that the peak stresses are in the order IG -  $LO_I > RG > IG - RO$ . This leads to the life results such that, the calculated life numbers are in the order IG -  $LO_I < RG < IG - RO$ .

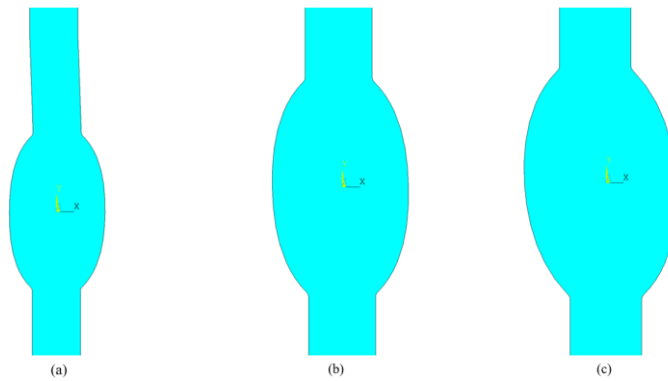
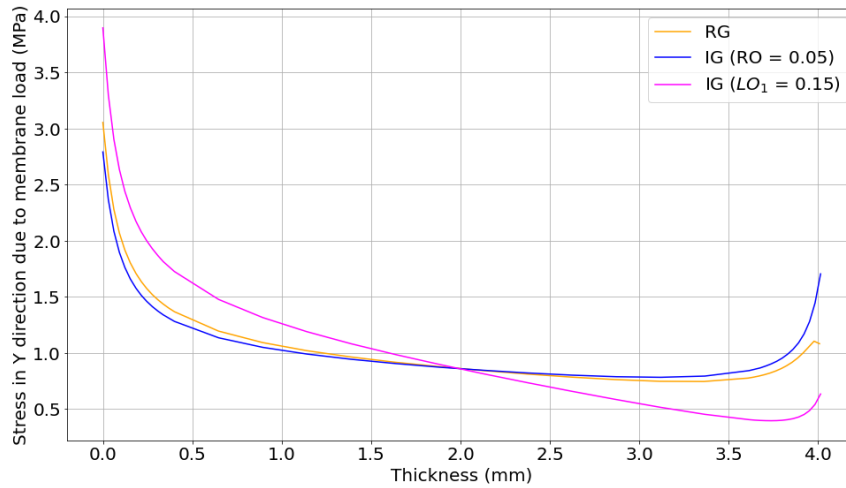

 Figure 5.11: Different stress analysis geometries for a case with  $RO = 0.05$ ,  $\theta = 2^\circ$  and  $f = 0.6$  (a) RG (b) IG [ $RO = 0.05$ ] (c) IG [ $LO_I = 0.15$ ]


Figure 5.12: Stress gradients due to membrane load for three cases in Table 5.3

Consider another case with normalized  $RO$  and  $LO_I$  values as listed in Table 5.4. The weld geometries for the three cases are shown in Figure 5.13. The respective life results are highlighted in Figure 5.17 and Table 5.4.

Table 5.4: Example 2 – Parameters of a real geometry and life results from three analysis approaches

<i>Geometry Parameters</i>	<i>Value</i>	<i>Analysis approach</i>	<i>Life (cycles)</i>
Normalized remote offset ( $RO$ )	0.025	RG	667078
Angular deflection ( $\theta$ )	2 [°]	IG – $RO$	1225533
Length factor ( $f$ )	0.6	IG – $LO_I$	984727
Normalized local offset ( $LO_I$ )	0.043		

The stress gradients due to membrane load for the three cases are shown in Figure 5.14. It is observed that the peak stresses are in the order  $RG > IG - LO_I > IG - RO$  and the corresponding calculated life results are in the order  $RG < IG - LO_I < IG - RO$ .

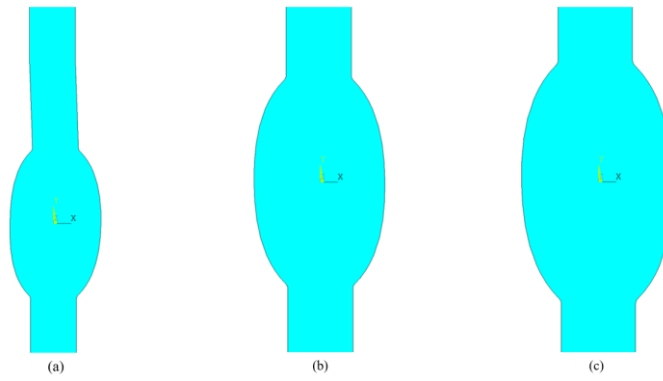


Figure 5.13: Different stress analysis geometries for a case with  $RO = 0.025$ ,  $\theta = 2^\circ$  and  $f = 0.6$  (a) RG (b) IG [ $RO = 0.025$ ] (c) IG [ $LO_I = 0.043$ ]

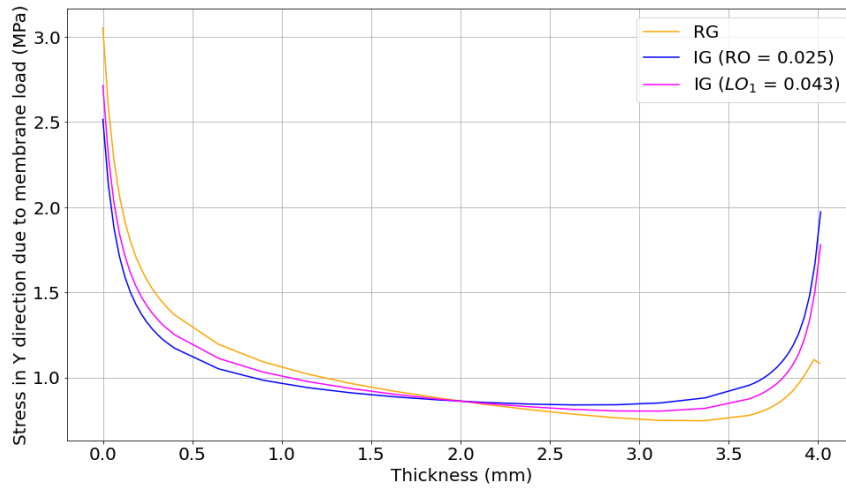


Figure 5.14: Stress gradients due to membrane load for three cases in Table 5.4

Table 5.5 shows another case of normalized  $RO$  and  $LO_I$ . The weld geometries for the three cases are shown in Figure 5.15. The respective life results are highlighted in Figure 5.17 and Table 5.5.

Table 5.5: Example 3 – Parameters of a real geometry and life results from three analysis approaches

<i>Geometry Parameters</i>	<i>Value</i>	<i>Analysis approach</i>	<i>Life (cycles)</i>
Normalized remote offset ( $RO$ )	0.08	RG	$\approx 619939$
Angular deflection ( $\theta$ )	2 [°]	IG – $RO$	619939
Length factor ( $f$ )	0.6	IG – $LO_I$	300014
Normalized local offset ( $LO_I$ )	0.16		

The stress gradients due to membrane load for the three cases are shown in Figure 5.16. It is observed that the peak stress is highest for IG -  $LO_I$ . The stress gradients are approximately same for RG and IG –  $RO$ . The same behaviour is observed in the obtained life results where, IG -  $LO_I$  predicts the minimum life. However, the life results for RG and IG –  $RO$  is approximately the same.

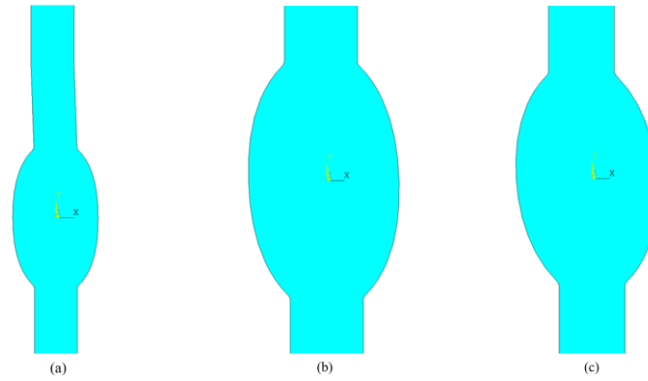


Figure 5.15: Different stress analysis geometries for a case with  $RO = 0.08$ ,  $\theta = 2^\circ$  and  $f = 0.6$  (a) RG (b) IG [ $RO = 0.08$ ] (c) IG [ $LO_I = 0.16$ ]

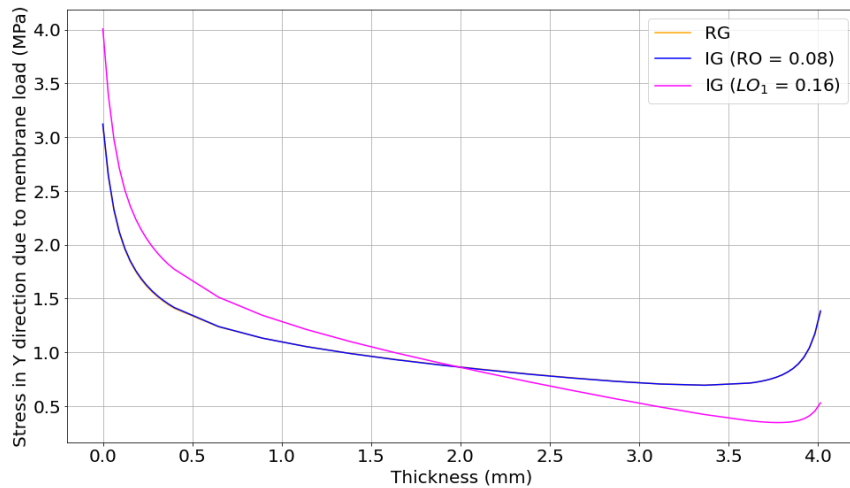


Figure 5.16: Stress gradients due to membrane load for three cases in Table 5.5

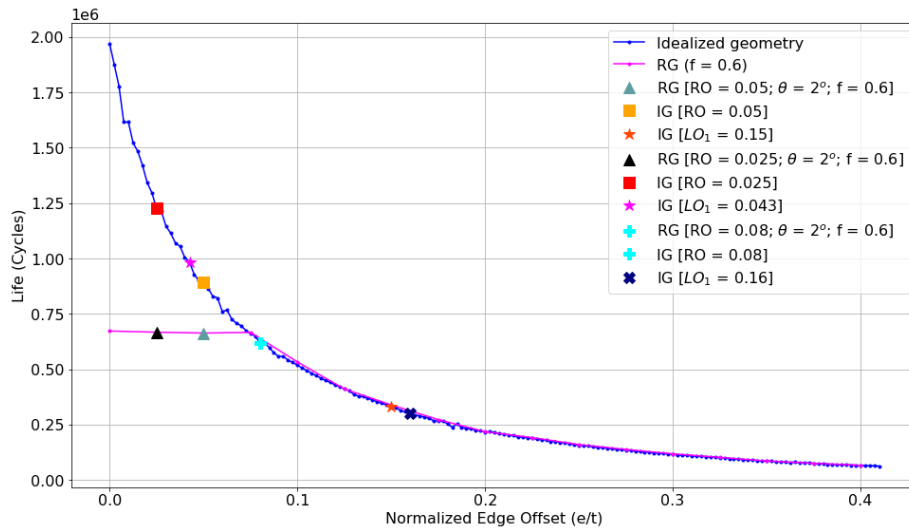


Figure 5.17: Fatigue life results for various cases of idealized and real geometries

From this deterministic analysis, we can conclude that results from the life calculations carried out using the idealized geometry can be very different from a model that includes the local geometry around the weld region. The results from the idealized geometry also depend highly on the edge offset considered for the life calculation. Further, there is no single measurement of offset (remote or local) that, when used in the idealized analysis geometry, leads to a conservative life estimate.

It is thus clear that a large number of simulations needs to be carried out to obtain a better insight about the effect of local geometry on calculated fatigue life. These analyses should account for the variation in edge offset as observed in the actual measurements reported in Chapter 3. From previous analyses, it is known that the weld root radius plays an important role in fatigue life calculation. Chapter 3 also quantified the observed variations in weld root radius values.

In order to account for such variations, a statistical analysis is desirable. Accordingly, further analysis is carried out using Monte Carlo simulations. The procedure followed and the results obtained from the Monte Carlo simulations are discussed in Chapters 6 and 7, respectively.

## 6 Analysis Setup – Monte Carlo Simulations

The Monte Carlo (MC) simulation, also known as the Monte Carlo method, is a numerical method of solving a mathematical problem by simulations of random variables. The method is used to simulate a process several times, to study the effect of the randomness in the input variables on the desired outcome of the problem [21]. Here, we would like to study the sensitivity of the edge offset and weld toe radii on the fatigue life, for two weld geometry cases: idealized (Figure 1.2) and real geometry (Figure 2.5). Four variables are considered for the MC simulation, which are listed in Table 6.1.

Table 6.1: Variables considered for MC simulation

<i>Variables in MC simulation</i>	<i>Applicable analysis geometry</i>
Normalized edge offset ( $norm\_e$ )	Idealized and real geometry
Normalized top toe radius ( $norm\_TR$ )	Idealized and real geometry
Normalized root toe radius ( $norm\_RR$ )	Idealized and real geometry
Local angular deflection ( $\theta$ )	Real geometry

The MC simulation is performed in Python. The steps followed to perform a MC simulation are illustrated in Figure 6.1. Each step is discussed further in detail in the following sections.

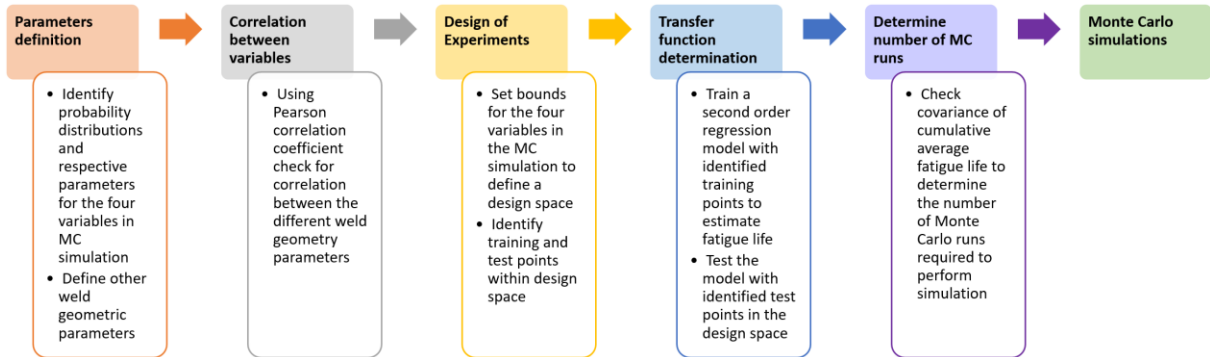


Figure 6.1: Illustration of steps involved to perform a Monte Carlo simulation

### 6.1 Weld geometry parameters

From the weld measurements discussed in Chapter 3, the probability distribution that provides a good representation of the spread of data, for the four variables listed in Table 6.1 are determined. The *scipy.stats* module within Python is used to evaluate distributions. The data considered to identify the distributions comprise of both non-conformance reports and weld qualification data for Nickel base TIG welds (see Chapter 3).

From the statistical distributions discussed in Section 2.3.1, the exponential distribution as shown in Figure 6.2, visually, captures the spread of data for normalized edge offset. The distribution parameters of the fit are listed in Table 6.2.



Table 6.2: Parameters of exponential distribution fit for normalized edge offset

<i>Parameter</i>	<i>Value</i>
Location	0
Scale	0.075373

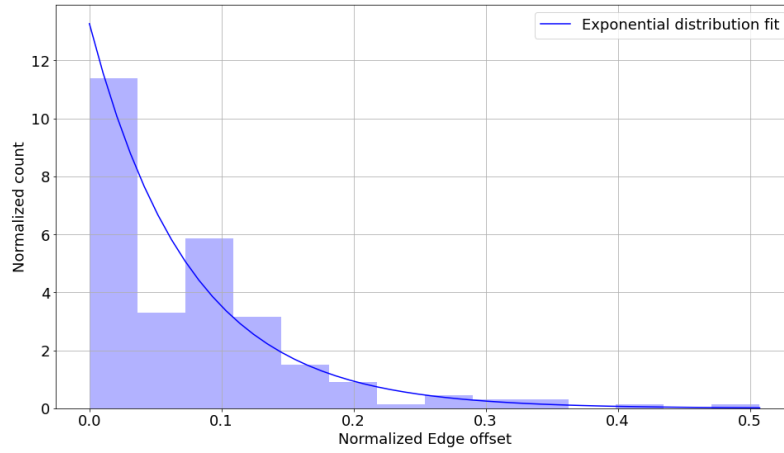


Figure 6.2: Histogram of normalized edge offset and exponential distribution fit

For both normalized top toe radius and normalized root toe radius, the lognormal distribution provides a good approximation of the spread of data, as shown in Figure 6.3 and Figure 6.4 respectively. The distribution parameters for the variables are listed in Table 6.3 and Table 6.4 respectively.

Table 6.3: Parameters of lognormal distribution fit for normalized top toe radius

<i>Parameter</i>	<i>Value</i>
Shape	1.093874
Location	-0.016442
Scale	1.731843

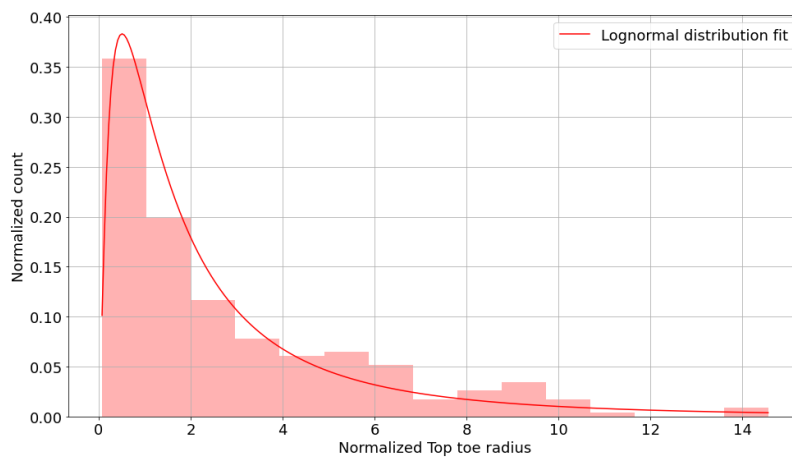


Figure 6.3: Histogram of normalized top toe radius and lognormal distribution fit

Table 6.4: Parameters of lognormal distribution fit for normalized root toe radius

<i>Parameter</i>	<i>Value</i>
Shape	0.734439
Location	-0.049476
Scale	0.600797

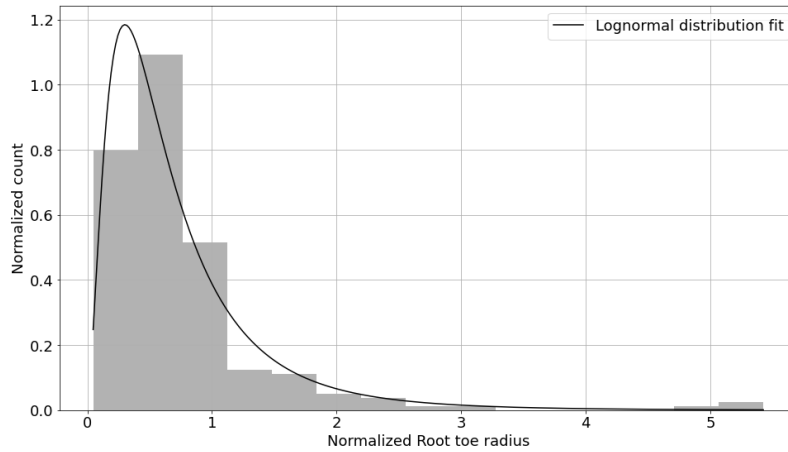
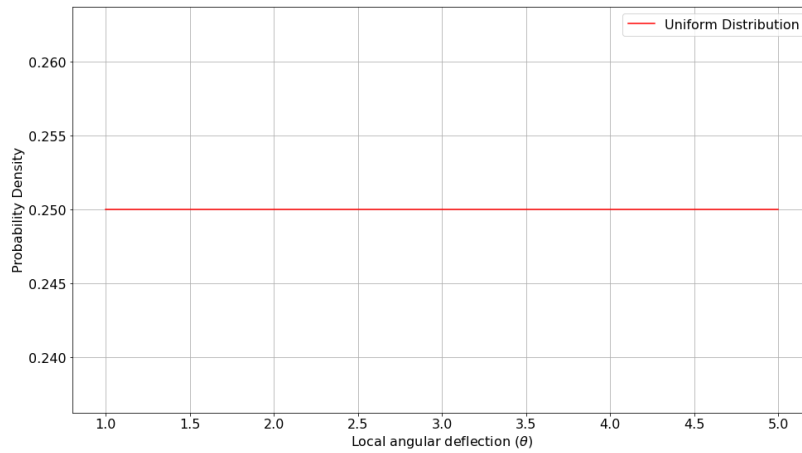


Figure 6.4: Histogram of normalized root toe radius and lognormal distribution fit

For the local angular deflection ( $\theta$ ), since the dataset available was not large enough, identifying the underlying distribution was not feasible. Hence, for conservative estimates, a uniform distribution was assumed within the identified bounds as shown in Figure 6.5.

Figure 6.5: Uniform distribution for local angular deflection ( $\theta$ )

The parameters normalized top bead width, internal top and root flank angles, and their respective values used in the simulation are listed in Table 6.5. These values represent a typical Nickel base TIG weld.

Table 6.5: Values of weld geometry parameters used in MC simulation

<i>Parameter</i>	<i>Value</i>
Normalized top bead width ( $B$ )	3.69
Internal top flank angle ( $\phi 1, \phi 2$ )	11 [°]
Internal root flank angle ( $\phi 3, \phi 4$ )	25 [°]

Other weld geometry parameters are set to the same values, as used in the deterministic analysis, which is summarized in Table 6.6. To reduce the complexity of the analysis, the length factor of local deflection ( $f$ ) is set to the average value from compiled data, obtained from non-conformance reports.

Table 6.6: Other weld geometric parameter values used in MC simulation

<i>Parameter</i>	<i>Value</i>
Root bead width ( $C$ )	B
Top bead height ( $Bh$ )	0.15*B
Root bead height ( $Ch$ )	0.15*C
Length of plate #1 ( $L1$ )	30 [mm]
Length of plate #2 ( $L2$ )	30 [mm]
Length factor of local deflection ( $f$ )	0.3

A design space is defined with the four variables listed in Table 6.1. The lower ( $x_L$ ) and upper ( $x_U$ ) bounds of the four variables are listed in Table 6.7. The lower bounds are set to the minimum observed value from the compiled weld measurement data. The upper bounds are chosen such that, it does not generate unrealistic geometries for the stress analysis. The idealized and real geometries for the respective lower and upper bound values are shown in Figure 6.6 and Figure 6.7.

Table 6.7: Lower and Upper bounds of the design space for MC simulation

<i>Parameter</i>	<i>[<math>x_L, x_U</math>]</i>
$norm\_e$	[0, 0.5]
$norm\_TR$	[0.071, 4]
$norm\_RR$	[0.05, 2.5]
$\theta$	[1°, 5°]

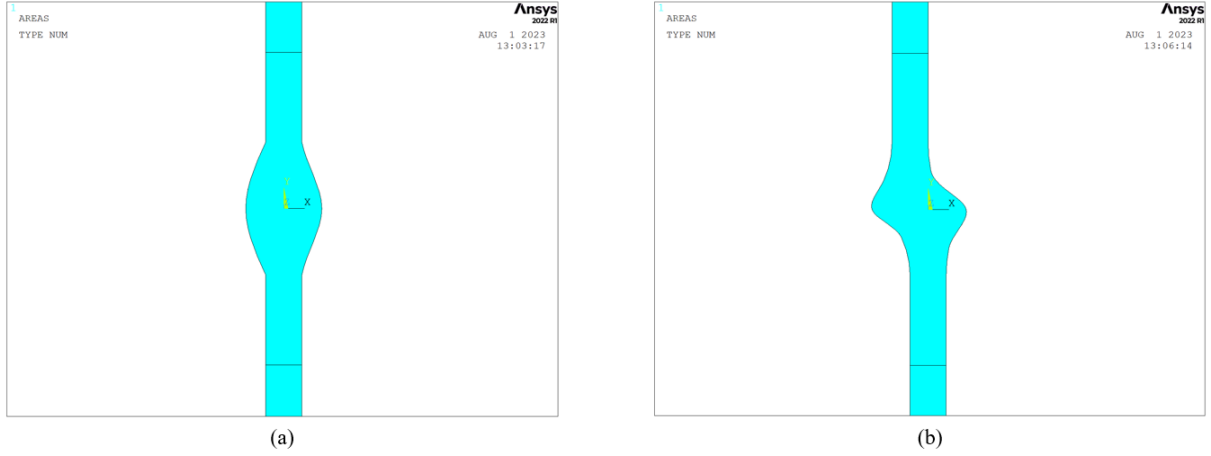


Figure 6.6: Idealized geometries at the extremities of the design space (a) lower bounds (b) upper bounds



Figure 6.7: Real geometries at the extremities of the design space (a) lower bounds (b) upper bounds

## 6.2 Correlation between variables

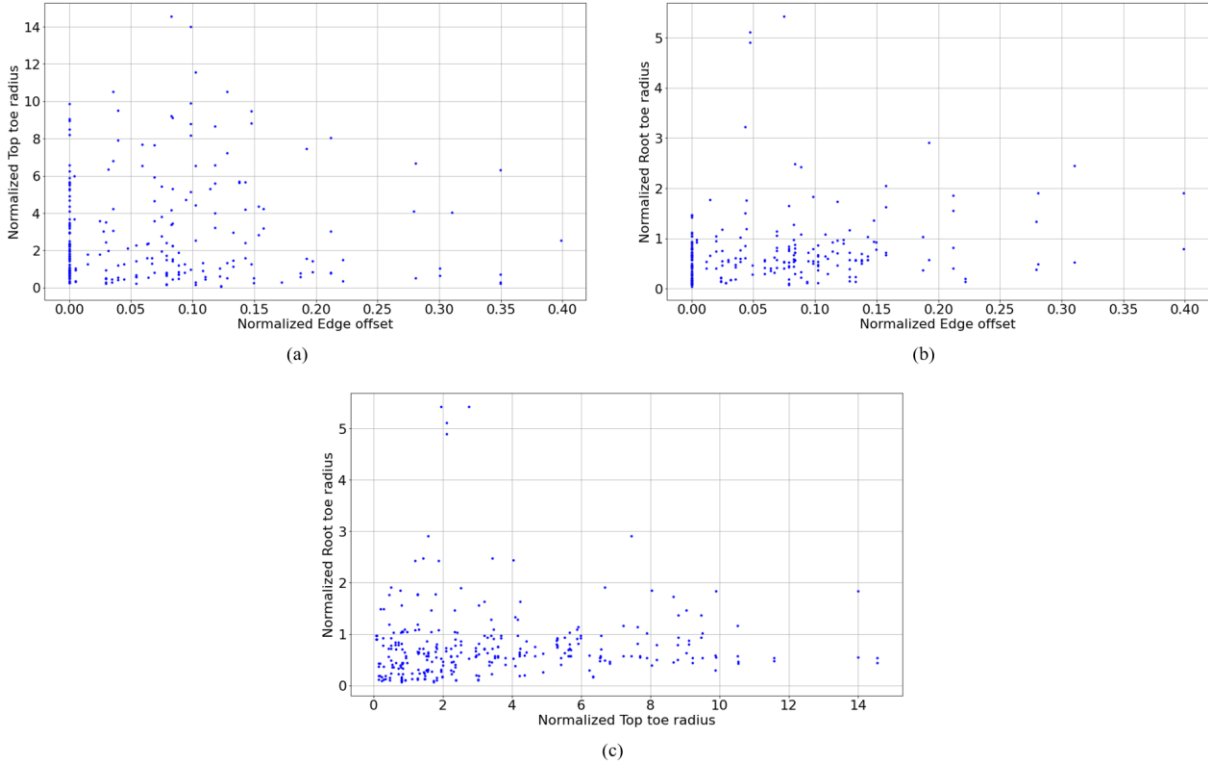
From the compiled weld measurements discussed in Section 3, the correlation between three variables: normalized edge offset ( $norm\_e$ ), normalized top toe radius ( $norm\_TR$ ) and normalized root toe radius ( $norm\_RR$ ) is evaluated using the Pearson's correlation coefficient, discussed in Section 2.3.2. For continuous variables, the relationship is shown in Equation (10) and can be rewritten for a discrete set of variables, as shown below,

$$\rho_{xy} = \frac{\sum[(x_i - \bar{x})(y_i - \bar{y})]}{\sqrt{\sum(x_i - \bar{x})^2 * \sum(y_i - \bar{y})^2}} \quad (21)$$

The correlation plots between pairs of variables are shown in Figure 6.8 and the respective coefficients identified using Equation (21), are listed in Table 6.8.

Table 6.8: Correlation coefficients of three variable pairs

<i>Variable pairs</i>	<i>Correlation coefficient (<math>\rho_{xy}</math>)</i>
$norm\_e$ vs $norm\_TR$	0.0241
$norm\_e$ vs $norm\_RR$	0.19
$norm\_TR$ vs $norm\_RR$	0.052

Figure 6.8: Correlation plots (a)  $norm\_e$  vs  $norm\_TR$  (b)  $norm\_e$  vs  $norm\_RR$  (c)  $norm\_TR$  vs  $norm\_RR$ 

The  $norm\_TR$  is independent of both  $norm\_e$  and  $norm\_RR$ , since the correlation coefficient is close to zero for both the cases. Even though the correlation coefficient is 0.19 between  $norm\_e$  and  $norm\_RR$ , the value is not large enough to imply a positive correlation. Hence, all three variables are treated independent of each other.

### 6.3 Determination of transfer function

In the Monte Carlo (MC) simulation, repeated sampling of the random variables is performed, to predict the distribution of life. Performing full simulations (i.e., extracting stress gradients from stress analysis and performing NASGRO runs to evaluate life, discussed in Sections 4.1 and 4.2) for each case is time consuming. Therefore, the entire process is represented with a transfer function or surrogate model to estimate the fatigue life. This significantly reduces the time taken to perform large number of MC runs, while estimating the life distribution with sufficient accuracy.

While performing full simulations in MC simulation to train the transfer function, life from both the forward and reverse bending cases are evaluated and the minimum of the two lives are considered for each case (see Section 4.1.5 for explanation). In the simulations, instead of creating new geometry by changing the ‘direction’ of offset, the global bending moment is applied in the reverse direction, which is an equivalent consideration. Note that within each case (i.e. forward and reverse bending), crack propagation lives are computed assuming different locations for the initial crack (see Section 4.1.4).

The upper bounds of the normalized root radius (*norm\_RR*), shown in Table 6.7, result in large root radii, which result in high fatigue lives and in some cases, can result in infinite fatigue lives. To overcome this and have finite fatigue lives in the considered design space, the magnitude of loads in NASGRO (Section 4.2.3) is increased by increasing the stress scale factors of S0 and S1 stresses (*scl\_fac<sub>S0</sub>* and *scl\_fac<sub>S1</sub>*) to 2, see Equation (20). Thus, for all simulations in Chapters 6 and 7, both the membrane and bending stresses oscillate between 0 and 200 MPa.

Additionally,  $\log_{10}$  values of the life results from full simulation is used to train the transfer function. It is known that small changes in stress causes large change in fatigue life. The use of  $\log_{10}(\text{life})$  as a dependent variable reduces the non-linearity and hence the error in training the transfer function. Consequently in the MC simulation, the transfer function estimates  $\log_{10}(\text{life})$ , from which the life is calculated to obtain a distribution of life.

### 6.3.1 Transfer function for idealized geometry

The transfer function used for the idealized geometry is a three variable second order regression model considering interaction effects, shown in Equation (22),

$$\begin{aligned} \log_{10}(\text{life}) = & \beta_0 + \beta_1 x_1 + \beta_2 x_2 + \beta_3 x_3 + \beta_4 x_1^2 \\ & + \beta_5 x_1 x_2 + \beta_6 x_1 x_3 + \beta_7 x_2^2 + \beta_8 x_2 x_3 + \beta_9 x_3^2 \end{aligned} \quad (22)$$

where  $x_1$  corresponds to *norm\_e*,  $x_2$  corresponds to *norm\_TR* and  $x_3$  corresponds to *norm\_RR*. To train the transfer function to estimate the fatigue life accurately over the entire design space, points where full simulation have to be carried out are identified with two Design of Experiments (DoE) approaches: the Central Composite Design (CCD) and Latin Hypercube Sampling (LHS). Concepts of regression models and DoE are discussed in Sections 2.3.3 and 2.3.4 respectively.

Since the design space is well defined as shown in Table 6.7,  $\alpha$  value is set to 1. With the bounds defined, for three variables the CCD yields 15 full simulation points covering extremities of the design space, which is shown in Figure 6.9.

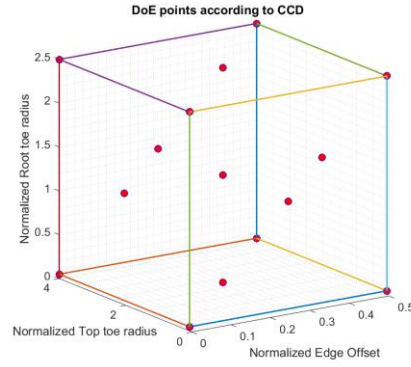


Figure 6.9: Fifteen full simulation points according to CCD for training IG transfer function

Additionally, to train the function to predict the fatigue life accurately within the design space, 75 full simulation points are identified with LHS that fill up the entire design space, as shown in Figure 6.10. Full simulations are carried out at the identified 90 points and the  $\log_{10}(\text{life})$  is evaluated.

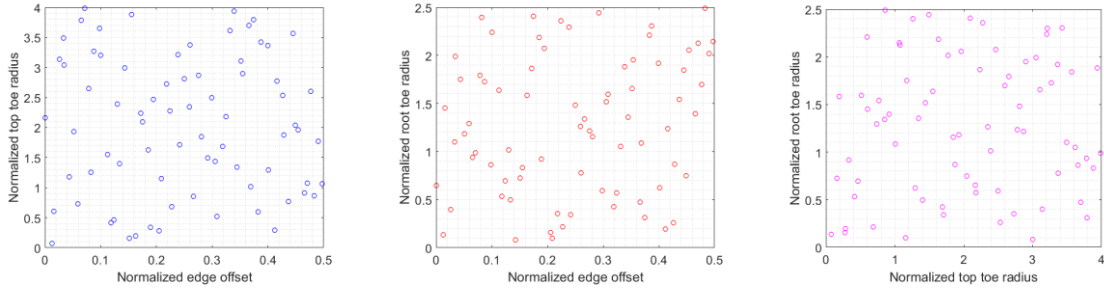


Figure 6.10: Seventy-five full simulation points according to LHS for training IG transfer function

The transfer function shown in Equation (22) is identified for three plate thicknesses: 2.03 mm, 4 mm and 6 mm. With full simulation results at the 90 points for three thickness cases, the regression model is trained for each case with the respective results. The identified regression coefficients are listed in Table 6.9.

Table 6.9: Regression coefficients of transfer functions for IG – Three plate thicknesses

Plate thickness (mm)	Regression coefficients									
	$\beta_0$	$\beta_1$	$\beta_2$	$\beta_3$	$\beta_4$	$\beta_5$	$\beta_6$	$\beta_7$	$\beta_8$	$\beta_9$
2.03	4.915	-3.528	0.013	0.229	1.716	-0.029	0.067	-0.002	0.003	-0.067
4	4.845	-3.799	0.016	0.271	1.914	-0.042	0.080	-0.003	0.004	-0.079
6	4.770	-3.905	0.016	0.310	1.945	-0.045	0.092	-0.003	0.004	-0.089

The obtained regression coefficients show that the normalized edge offset ( $\beta_1$ ) has the maximum influence and a negative effect on life. The next highest influence is due to the normalized root toe radius ( $\beta_3$ ), which has a positive effect on life. The normalized top toe radius ( $\beta_2$ ) has a negligible influence on the fatigue life.

To validate the transfer functions, the  $R^2$  and  $R^2_{adj}$  values are evaluated, which is shown in Table 6.10. The  $R^2$  and  $R^2_{adj}$  values are large and approximately equal to each other for the three cases, confirming good regression models.

Table 6.10:  $R^2$  and  $R^2_{adj}$  values of IG transfer functions for respective plate thickness values

Plate thickness (mm)	$R^2$	$R^2_{adj}$
2.03	0.997	0.997
4	0.997	0.996
6	0.996	0.996

An identity line is also used to validate the transfer functions. In addition to the 90 training points, 30 points are sampled at random from the distributions of the three variables, to test the transfer functions. Full simulations are performed at the test points. The transfer functions are used to predict the life at both the training and test points. The full simulation life and the predicted life are plotted along with an identity line to check the agreement between the two values, in a log-log plot.

The result for plate thickness of 2.03 mm is shown in Figure 6.11. It is seen that transfer function predicts the fatigue life with good accuracy, well within a factor of 1.5 of the full simulation life. The results for plate thicknesses of 4 mm and 6 mm are shown in Appendix 10.4.

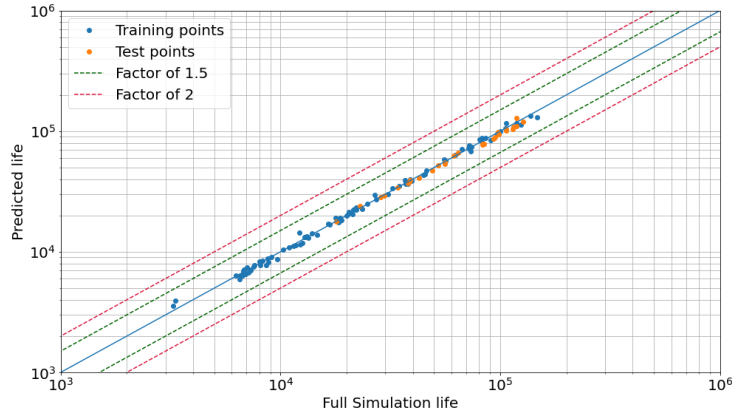


Figure 6.11: Full simulation vs Predicted life from transfer function of IG [Thickness = 2.03 mm]

### 6.3.2 Transfer function for real geometry

The transfer function used for a real geometry is a four variable second order regression model, considering interaction effects, as shown in Equation (23),

$$\begin{aligned} \log_{10}(\text{life}) = & \beta_0 + \beta_1 x_1 + \beta_2 x_2 + \beta_3 x_3 + \beta_4 x_4 + \beta_5 x_1^2 + \beta_6 x_1 x_2 + \beta_7 x_1 x_3 \\ & + \beta_8 x_1 x_4 + \beta_9 x_2^2 + \beta_{10} x_2 x_3 + \beta_{11} x_2 x_4 + \beta_{12} x_3^2 + \beta_{13} x_3 x_4 + \beta_{14} x_4^2 \end{aligned} \quad (23)$$



where  $x_1$  corresponds to  $norm\_e$ ,  $x_2$  corresponds to  $norm\_TR$ ,  $x_3$  corresponds to  $norm\_RR$  and  $x_4$  corresponds to  $\theta$ . Similar to idealized geometry, in order to train the transfer function to estimate the fatigue life accurately over the entire design space, full simulation points are identified using CCD and LHS approaches.

Since the bounds of the design space are well defined as shown in Table 6.7,  $\alpha$  value is set to 1. For four variables, the CCD yields 25 experiments covering the extremities of the entire design space, which is shown in Figure 6.12.

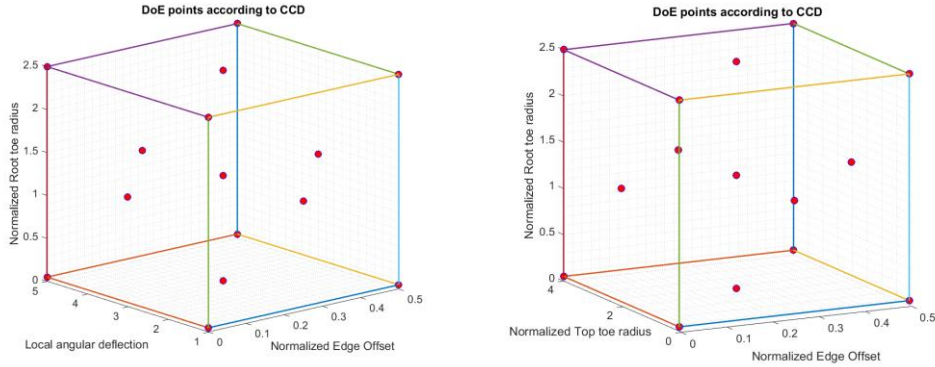


Figure 6.12: Twenty-five full simulation points according to CCD for training real geometry transfer function

Additionally, to train the function to predict fatigue life accurately within the design space, 75 full simulation points are identified with LHS, which covers the entire design space as shown in Figure 6.13. Full simulations are carried out at the identified 100 points and the  $\log_{10}(\text{life})$  is evaluated.

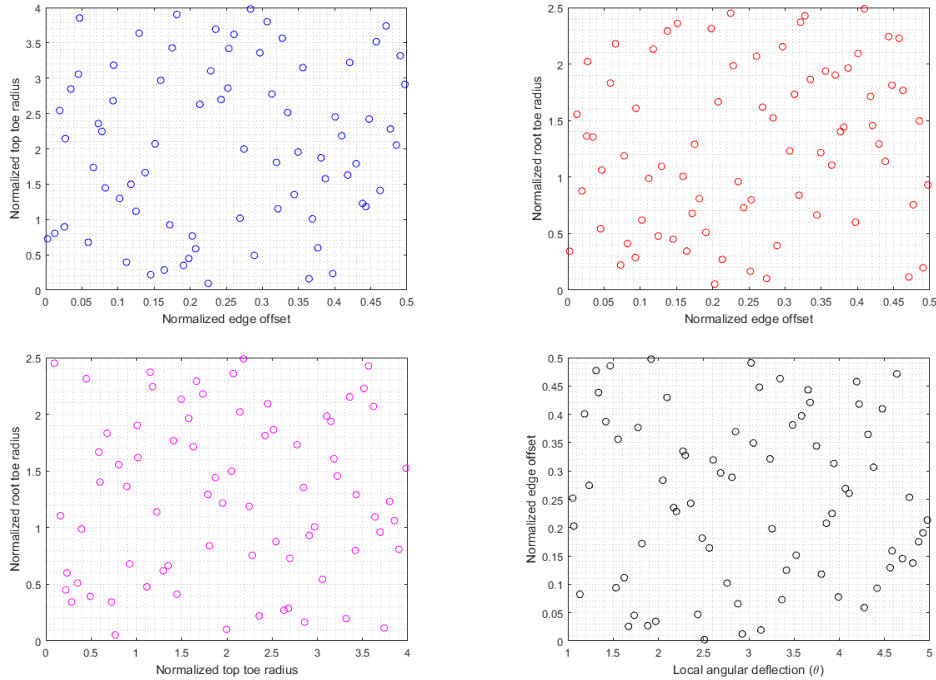


Figure 6.13: Seventy-five full simulation points according to LHS for training real geometry transfer function

The regression model shown in Equation (23) is trained with the full simulation results for a plate thickness of 2.03 mm. The identified regression coefficients is listed in Table 6.11.

Table 6.11: Regression coefficients of transfer function for real geometry [Thickness = 2.03 mm]

<i>Regression coefficients</i>											
$\beta_0$	$\beta_1$	$\beta_2$	$\beta_3$	$\beta_4$	$\beta_5$	$\beta_6$	$\beta_7$	$\beta_8$	$\beta_9$	$\beta_{10}$	$\beta_{11}$
4.844	-2.761	-0.033	0.279	-0.038	-0.095	-0.020	0.064	0.132	-0.006	-0.003	-0.001
$\beta_{12}$	$\beta_{13}$	$\beta_{14}$									
-0.075	-0.003	-0.0007									

From the identified regression coefficients of the transfer function for a real geometry, it is observed that the normalized edge offset ( $\beta_1$ ) has the maximum influence and a negative effect on life. The next highest influence is due to the normalized root toe radius ( $\beta_3$ ) which has a positive effect on life. The normalized top toe radius ( $\beta_2$ ) and local angular deflection ( $\beta_4$ ) have similar yet, negligible influence on life.

To validate the transfer function, the  $R^2$  and  $R^2_{adj}$  values are evaluated, which are shown in Table 6.12. It is observed that the  $R^2$  and  $R^2_{adj}$  values are large and approximately equal to each other, confirming a good regression model.

Table 6.12:  $R^2$  and  $R^2_{adj}$  values of the transfer function for real geometry [Thickness = 2.03 mm]

$R^2$	$R^2_{adj}$
0.982	0.979

An identity line is also used to validate the transfer function. In addition to the 100 training points, 30 points are sampled at random from the distributions of the four variables, to test the transfer function. Full simulations are performed at the test points. The transfer function is used to predict the life at both the training and test points. The full simulation life and the predicted life are plotted along with an identity line to check the agreement between the two values, in a log-log plot. The result for plate thickness of 2.03 mm is shown in Figure 6.14. It is observed that the transfer function predicts life values with good accuracy within a factor of 1.5 of the full simulation life.

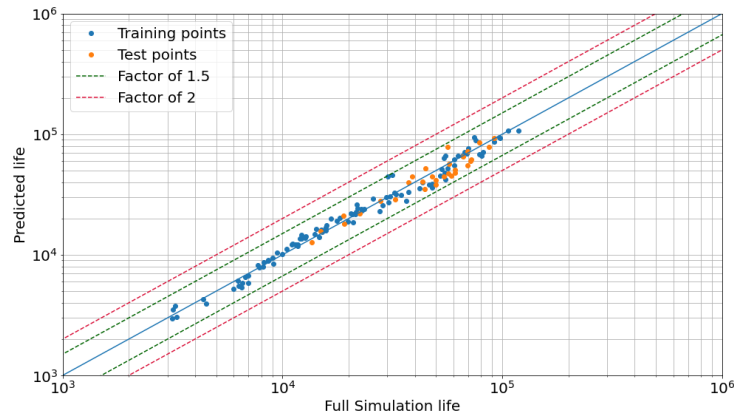


Figure 6.14: Full simulation vs Predicted life from transfer function for real geometry [Thickness = 2.03 mm]

## 6.4 Monte Carlo Simulation

### 6.4.1 Number of Monte Carlo runs

Since the Monte Carlo (MC) simulation is essentially a random sampling procedure, it is important to identify the number of MC runs required to achieve a stable result. The coefficient of variation (CV) from 20 iterations of the cumulative average fatigue life (CAFL) is evaluated for increasing MC runs. The results are shown in Table 6.13.

For 50000 MC runs, the CAFL is predicted with great accuracy as it tends to the mean value with the least standard deviation, and the CV is 0.20 %. The respective convergence plot for 50000 MC runs is shown in Figure 6.15. The plots for other cases is shown in Appendix 10.5. Henceforth, 50000 MC runs will be performed for all MC simulations.

Table 6.13: Coefficient of variation for CAFL for various cases of MC runs

<i>No. of MC runs</i>	<i>Mean of CAFL (Cycles)</i>	<i>Standard deviation of CAFL (Cycles)</i>	<i>CV (standard deviation / mean)</i>	<i>% CV</i>	<i>Time to complete runs</i>
100	69799	2536	0.0363	3.63	0.53 sec
1000	70265	771	0.0109	1.09	2.67 sec
10000	70122	268	0.0038	0.38	25.43 sec
20000	70287	257	0.0036	0.36	54.06 sec
30000	70165	196	0.0027	0.27	1 min 36 sec
50000	70160	144	0.0020	0.20	2 min 59 sec

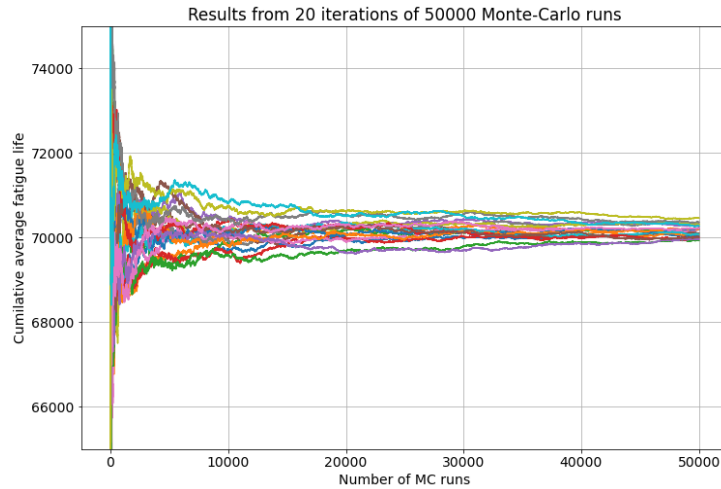


Figure 6.15: Convergence plot of *CAFL* for 20 iterations of 50000 MC runs

#### 6.4.2 Script algorithm to perform Monte Carlo simulation

The algorithm that is followed to perform the Monte Carlo (MC) simulation for idealized geometry is shown in Figure 6.16. The process starts by defining the probability distributions and bounds for the three variables of the idealized geometry. With the number of MC runs defined, a random sample dataset is generated from the probability distributions.

The next step in the MC simulation involves performing checks on the generated sample dataset of the variables, to verify the values are within the bounds of design space. The conditions defined are as follows:

- If any of the sampled variables exceed the respective lower bounds of the design space, or the maximum observed value obtained from weld measurements – The dataset is ignored and a new sample dataset is generated.
- If any of the sampled variables exceed the respective upper bounds of the design space, but are less than the maximum observed value obtained from weld measurements – The upper bound value is assigned to the variable and the process continues.
- If the sampled variables are within the bounds of the design space, the generated samples are used and the process continues.

Following the checks, the transfer function is used to estimate the fatigue life for the generated random sample dataset. The estimated life is stored and the next run continues. The procedure loops until the defined number of MC runs are completed. Finally, the Empirical Cumulative Distribution Function (discussed in Section 2.3.5) of the distribution of life is determined to compare the results from different cases.

The MC simulation procedure is similar for the Case 2 (real) geometry, but additionally the fourth variable (local angular deflection -  $\theta$ ) is sampled from a uniform distribution along with

aforementioned three variables. The respective transfer function for real geometry is used for estimation of fatigue life.

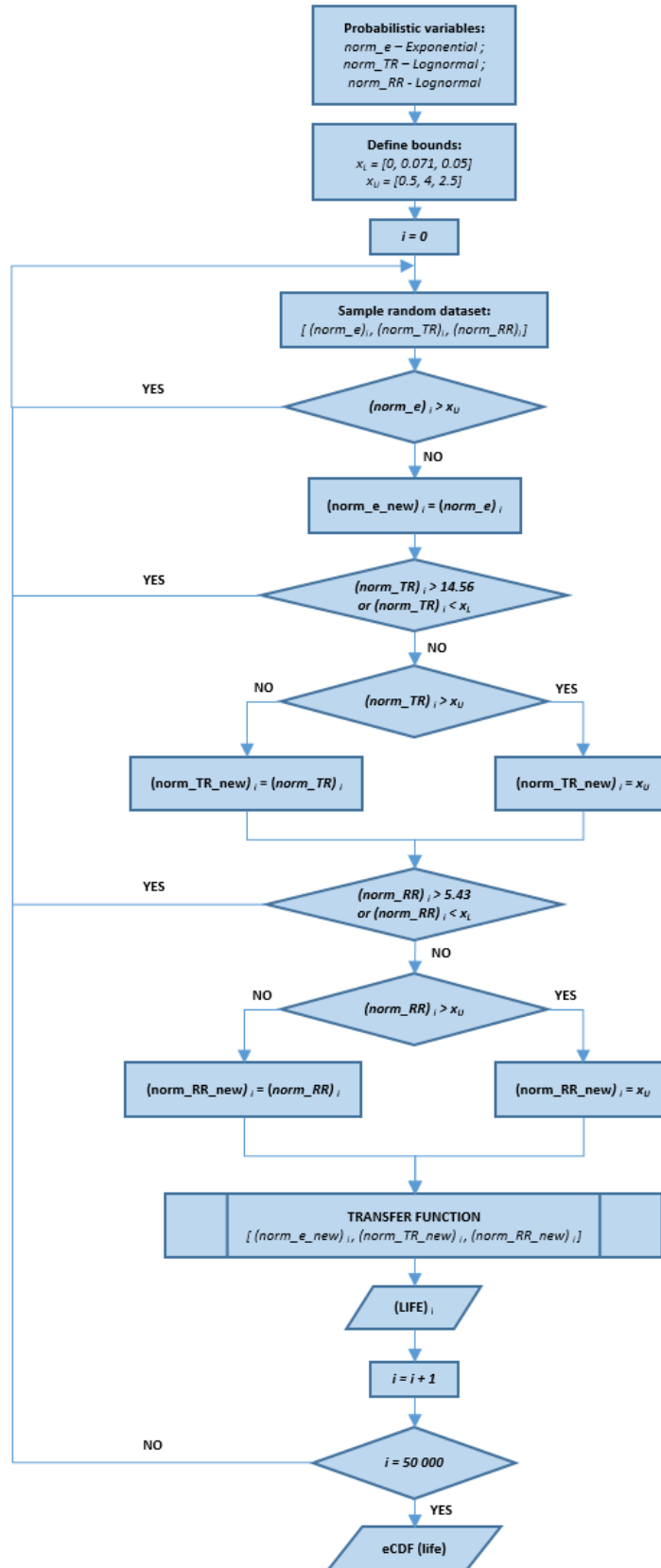


Figure 6.16: Algorithm for MC simulation - idealized geometry

## 7 Results – Monte Carlo simulations

### 7.1 Effect of thickness on fatigue life

A study is conducted to investigate the influence of varying thickness of the joining plates on the fatigue life. The idealized geometry is considered for the analysis. The initial crack size is fixed to dimensions shown in Table 4.6. Monte Carlo (MC) simulations are performed for three plate thicknesses, namely: 2.03 mm, 4 mm and 6 mm. The respective transfer functions identified in Section 6.3.1 are used for the analysis. The Empirical Cumulative Distribution Function (eCDF) is calculated and used for comparison of results. Two types of edge offset are investigated: normalized edge offset and absolute edge offset. The obtained results are discussed in the following sections.

#### 7.1.1 Normalized edge offset

For this study, the distribution of normalized edge offset shown in Figure 6.2 is used. Figure 7.1 shows the fatigue life vs failure probabilities for the three thickness cases. Two parameters of interest are the minimum life or 99.9% survival probability and the median life or 50% survival probability, which are shown for the respective cases in Table 7.1.

Table 7.1: Minimum life and median life for three thickness cases – Idealized geometry

<i>Plate thickness (mm)</i>	<i>Minimum life - 99.9% survival probability (cycles)</i>	<i>Median life – 50% survival probability (cycles)</i>
2.03	5679	71999
4	4217	62138
6	3252	53993

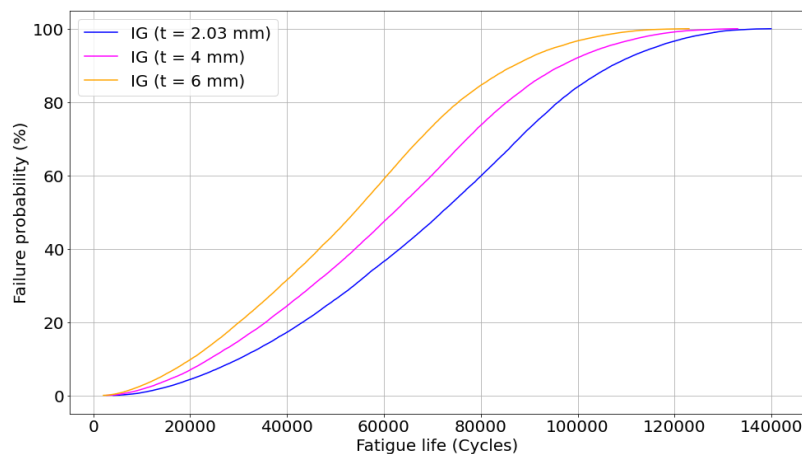


Figure 7.1: Empirical CDF of fatigue life for three thickness cases – Idealized geometry (IG)

It is observed that as the thickness of the plate increases, the resulting fatigue life reduces. Since the normalized edge offset ( $norm_e$ ) is used in estimating the fatigue life, for the same  $norm_e$

value, higher plate thickness results in a higher edge offset, which results in a reduction of fatigue life.

### 7.1.2 Absolute edge offset

The absolute value of the edge offset is fixed at 0.3 mm and the respective *norm\_e* values are varied for the three plate thicknesses is listed in Table 7.2.

Table 7.2: *norm\_e* values for different plate thicknesses [ $e = 0.3$  mm]

<i>Edge offset</i>	<i>Plate thickness (mm)</i>	<i>Normalized edge offset (norm_e)</i>
0.3 mm	2.03	0.1478
	4	0.075
	6	0.05

The fatigue life vs failure probabilities for the three cases is shown in Figure 7.2. The respective minimum and median lives are listed in Table 7.3. It is observed that as the thickness of the plate increases, the resulting fatigue life increases.

Table 7.3: Minimum life and median life for three thickness cases – IG [ $e = 0.3$  mm]

<i>Edge offset</i>	<i>Plate thickness (mm)</i>	<i>Minimum life - 99.9% survival probability (cycles)</i>	<i>Median life – 50% survival probability (cycles)</i>
0.3 mm	2.03	27842	35625
	4	39072	51794
	6	40276	55364

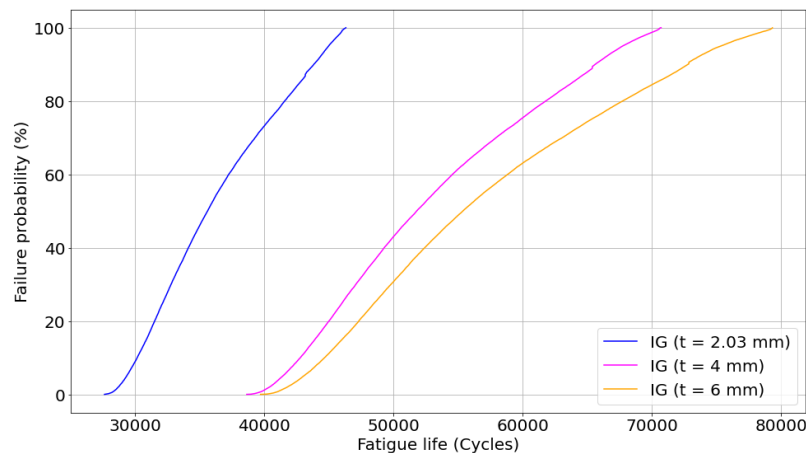


Figure 7.2: Empirical CDF of fatigue life for three thickness cases – Idealized geometry (IG) [ $e = 0.3$  mm]

To understand the behaviour, consider a case when the *norm\_TR* and *norm\_RR* values are set to 0.1. For this case, full simulations (i.e., extracting stress gradients from stress analysis and performing NASGRO runs to evaluate life) are carried out for the three thickness values. The obtained fatigue lives are listed in Table 7.4. Similar to the MC simulation results, as the thickness of the plates increase, an increase of fatigue lives is observed.

Table 7.4: Fatigue lives for three thickness cases from full simulation - IG [ $e = 0.3$  mm]

<i>norm_TR</i>	<i>norm_RR</i>	<i>norm_e</i>	<i>Plate thickness (mm)</i>	<i>Fatigue life (cycles)</i>
0.1	0.1	0.1478	2.03	26804
		0.075	4	37629
		0.05	6	39271

A surface crack as shown in Figure 4.13 is used in the crack propagation analysis. The surface crack has two tips: the a-tip and c-tip, which are illustrated in Figure 7.3.

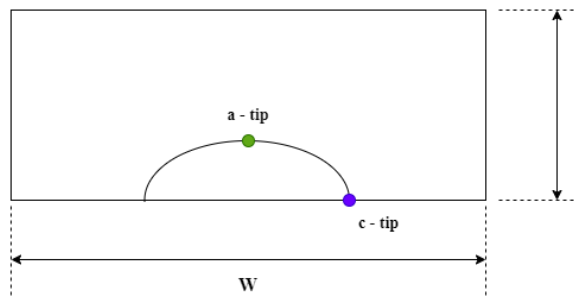
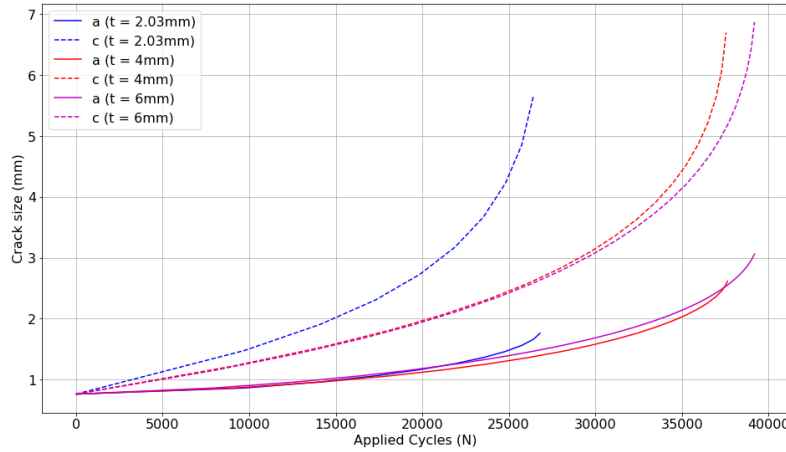


Figure 7.3: a-tip and c-tip in a surface crack

From the results of crack propagation analysis, the crack size vs cycles is shown in Figure 7.4 for both the a-tip and c-tip. It is observed that the crack grows faster at the c-tip compared to the a-tip.

Figure 7.4: Crack size vs Applied cycles of a-tip and c-tip for three thicknesses - IG [ $e = 0.3$  mm]

From Paris law shown in Equation (3), we know that the crack growth rate ( $da/dN$ ) is directly proportional to the stress intensity factor range ( $\Delta K$ ). The  $\Delta K$  at the c-tip is plotted against the crack size of c-tip, which is shown in Figure 7.5. Here, it is observed that the  $\Delta K$  value reduces for higher thickness values.



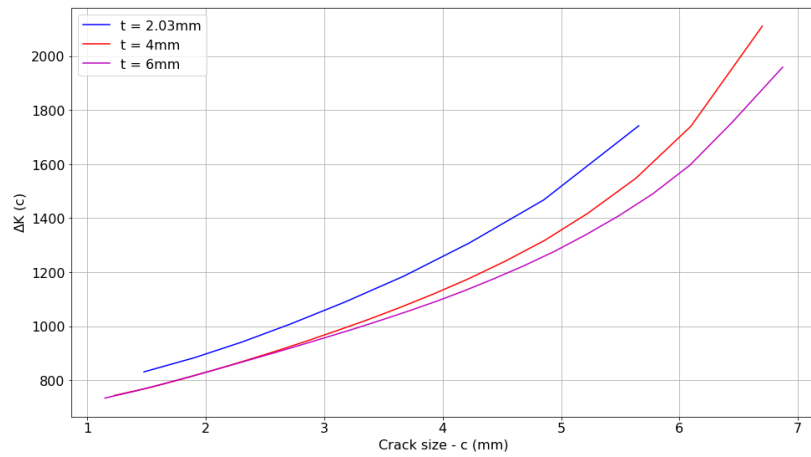


Figure 7.5: Stress intensity factor range  $\Delta K$  vs crack size at c-tip for three thicknesses - IG [ $e = 0.3$  mm]

This results in lower crack growth rates for increasing thickness, which leads to an increase in fatigue life for higher plate thicknesses.

## 7.2 Influence of real geometry on the fatigue life

Monte Carlo (MC) simulations are carried out for idealized (Figure 1.2) and real (Figure 2.5) geometries, for a plate thickness of 2.03 mm. The weld geometry parameters discussed in Section 6.1, and the respective transfer functions identified in Sections 6.3.1 and 6.3.2, are used in the analysis. The Empirical Cumulative Distribution Function (eCDF) of fatigue life is calculated for both the cases, as discussed in Section 6.4, for comparison of results.

Figure 7.6 shows the eCDF of fatigue life vs the respective failure probabilities, for both the geometries. The minimum and median lives for the two cases are listed in Table 7.5. It is observed that both the geometries yield a similar minimum life. However, the real geometry predicts a lower median life compared to the idealized geometry.

Table 7.5: Minimum life and median life for idealized (IG) and real (RG) geometries

<i>Geometry case</i>	<i>Minimum life - 99.9% survival probability (cycles)</i>	<i>Median life – 50% survival probability (cycles)</i>
IG	5679	71999
RG	5739	54019

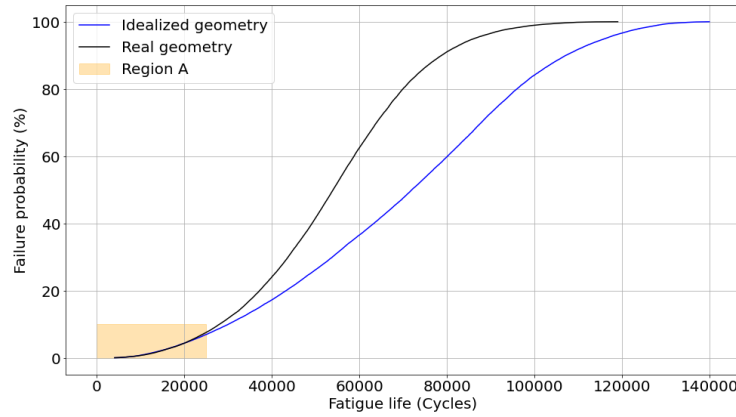


Figure 7.6: Empirical CDF of fatigue life for idealized and real geometries [Thickness = 2.03 mm]

In *Region A* (marked in Figure 7.6), both the geometries estimate similar life results. *Region A* corresponds to cases with high edge offset values. Since the edge offset has exceeded the threshold value (see Section 5.3 for explanation), the edge offset is a limiting factor on fatigue life instead of the local angular deflection ( $\theta$ ). However, for lower survival probabilities it is observed that the real geometry produces conservative life estimates compared to the idealized geometry, since the local angular deflection becomes a limiting factor on life.

For the idealized geometry, the distribution of life is affected by three variables: normalized edge offset ( $norm\_e$ ), normalized top toe radius ( $norm\_TR$ ) and normalized root toe radius ( $norm\_RR$ ), see Equation (22). From the results of the MC simulation, the correlation coefficients between the fatigue life and input variables are computed. The contribution to variance ( $v_i$ ) in fatigue life for each input variable is evaluated using the following equation,

$$v_i = \frac{c_i^2}{\sum_{i=1}^3 c_i^2} \quad \text{for } i = 1, 2, 3 \quad (24)$$

where  $c_i$  is the individual correlation coefficients between a input variable and fatigue life. The contribution to variance in fatigue life from the three input variables for the idealized geometry are shown in Figure 7.7.

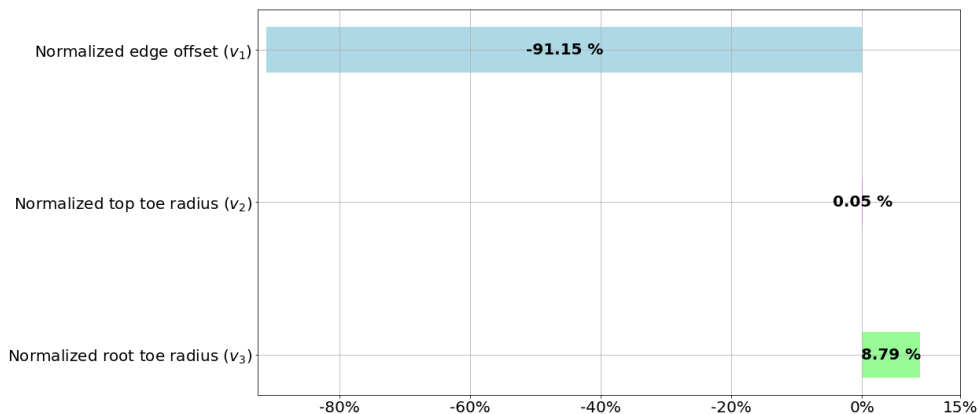


Figure 7.7: Contribution to variance in fatigue life from three input variables - idealized geometry

The  $norm\_e$  has the maximum influence on life (approximately 91%), and it has a negative effect. The second highest influence is due to  $norm\_RR$ , which has a positive effect on life, since an increase in the root radius reduces the stress concentrations in the weld region, which leads to an increase in life. The  $norm\_TR$  has a negligible influence on life, since the weld geometry considered for the analysis has a lower internal flank angle on the top side, compared to the root side, as shown in Table 6.5.

For the real geometry, the distribution of life is affected by four variables:  $norm\_e$ ,  $norm\_TR$ ,  $norm\_RR$  and the local angular deflection ( $\theta$ ), see Equation (23). Similar to the idealized geometry, the contribution of the four input variables, to the variance in fatigue life is evaluated, which is shown in Figure 7.8.

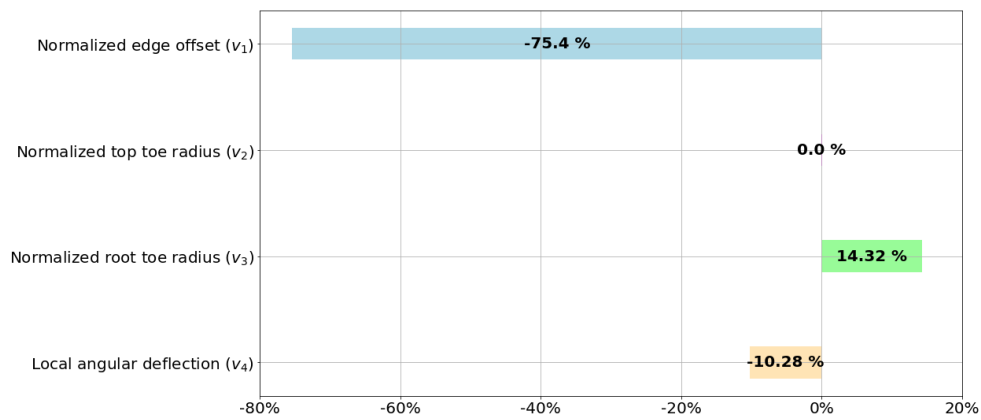


Figure 7.8: Contribution to variance in fatigue life from four input variables - real geometry

Comparing the results with the idealized geometry, the  $norm\_e$  again has the highest influence on life and a negative effect. The  $norm\_TR$  again has a negligible influence on life. The influence of  $norm\_RR$  on life has increased for a real geometry, since based on the weld geometry construction, the root radius has a higher influence on the stress concentrations caused due to the real geometry. The third highest influence is due to the local angular deflection. It has a negative effect on life, as an increase in  $\theta$  leads to a decrease in life, with the length factor of the local distortion ( $f$ ) fixed for the analysis (see Table 6.6).

From the results of MC simulation for both the idealized and real geometries, the dependence of life on the three variables:  $norm\_e$ ,  $norm\_TR$  and  $norm\_RR$  is investigated. The dependence is illustrated through scatter plots. Figure 7.9(a) and Figure 7.9(b) quantify the dependence on the normalized offset values, for idealized and real geometry, respectively. In both cases, the scatter band is larger for low normalized offset values. The variation in normalized radii values leads to a larger variation in life when the offset value is low. However, for high values of normalized offset, the stresses are dominated by the offset itself, and the influence of radii on fatigue life is small, leading to a narrow scatter band.

From Figure 7.10(a) and Figure 7.10(b), it is observed that no correlation can be identified between the top toe radius and resulting fatigue life. In the case of the root toe radius, from

Figure 7.11(a) and Figure 7.11(b), the life has a positive dependence until a  $norm\_RR$  value of approximately 1.5, after which no correlation can be identified.

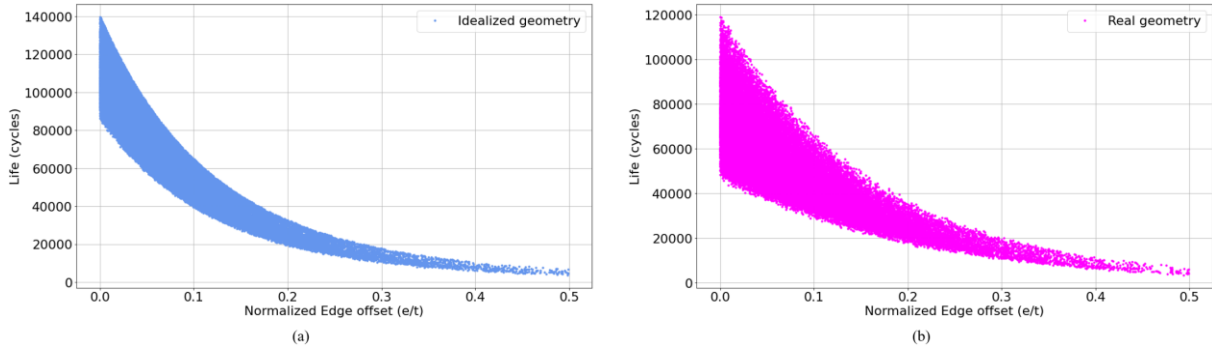


Figure 7.9: Dependence of life on normalized edge offset from results of MC simulation (a) Idealized geometry (b) Real geometry

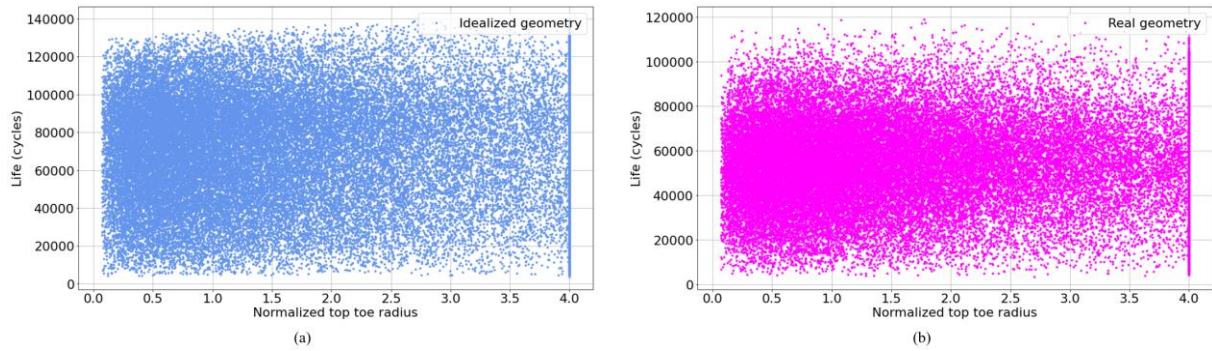


Figure 7.10: Dependence of life on normalized top toe radius from results of MC simulation (a) Idealized geometry (b) Real geometry

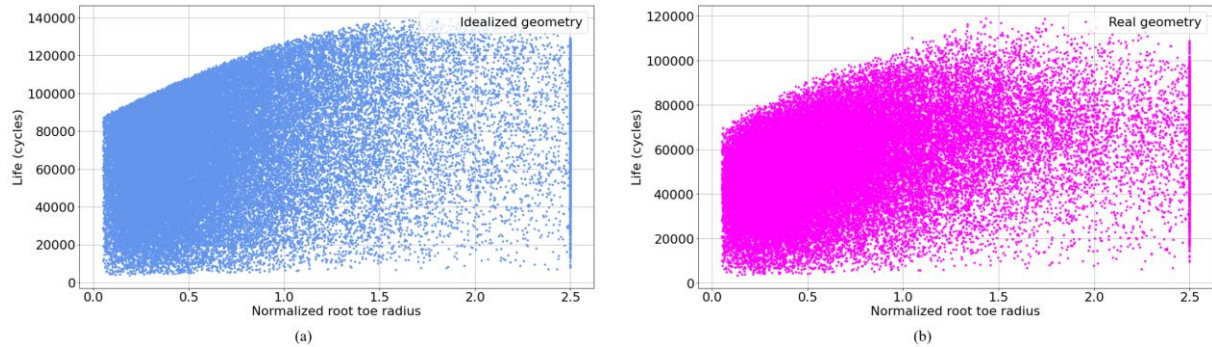
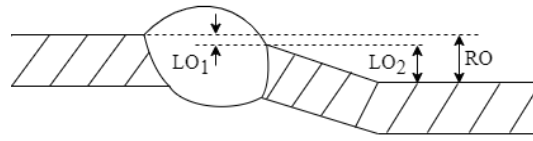


Figure 7.11: Dependence of life on normalized root toe radius from results of MC simulation (a) Idealized geometry (b) Real geometry

### 7.3 Influence of different edge offset measures on fatigue life

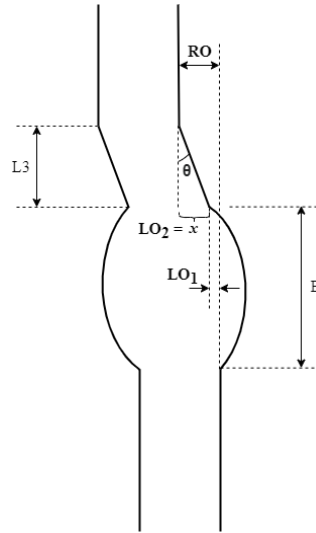
From the results of deterministic analysis in Section 5.4, two possible offset measures from the real geometry were investigated:  $RO$  and  $LO_1$ . Monte Carlo (MC) are performed for the different edge offset measures, to account for the randomness in the measures caused due to the real geometry. A third offset measure  $LO_2$ , in addition to  $RO$  and  $LO_1$ , shown in Figure 7.12, is considered in the analysis. A plate thickness of 2.03 mm is considered for the analysis. The idealized geometry (IG) transfer function is used to estimate the life for the different measures.

Figure 7.12: Three offset measures -  $RO$ ,  $LO_1$  and  $LO_2$ 

In the MC simulation, the *norm\_e* variable corresponds to the normalized  $RO$  measure. To evaluate other offset measures, a random sample of  $\theta$  is generated and as illustrated in Figure 7.13, values for  $LO_1$  and  $LO_2$  are calculated using Equations (25) and (26),

$$LO_2 = x = L3 * \tan(\theta) \quad (25)$$

$$LO_1 = |x - RO| \quad (26)$$

Figure 7.13: Schematic representation of geometry for calculation of  $LO_1$  and  $LO_2$ 

The calculated offset measures are normalized, and checked that they do not exceed the bounds of the design space. The Empirical Cumulative Distribution Function (eCDF) of fatigue life is identified for the different cases and the obtained results are discussed in the following sections.

### 7.3.1 Life distribution based on IG- $LO_1$

The fatigue life vs failure probability is shown Figure 7.15, for both  $RO$  and  $LO_1$  measures. The minimum and median lives for the two measures are tabulated in Table 7.6.

Table 7.6: Minimum life and median life for two offset measures -  $RO$  and  $LO_1$ 

Offset measure	Minimum life - 99.9% survival probability (cycles)	Median life – 50% survival probability (cycles)
$RO$	5679	71999
$LO_1$	7453	79045

The  $LO_I$  measure predicts a higher minimum life and a higher median life compared to  $RO$  measure. From Figure 7.15, for survival probabilities until *Region B*, the life estimated with  $LO_I$  is higher than that with  $RO$ . This is because, within the defined design space and the geometry used for the analysis, the  $LO_I$  measure is always less than or equal to  $RO$  measure. This is illustrated in Figure 7.14. Depending on the sampled  $RO$  value,  $LO_I$  can be below the  $X_{ref}$  line (see Figure 7.14(a)), or above the  $X_{ref}$  line (see Figure 7.14(b)).

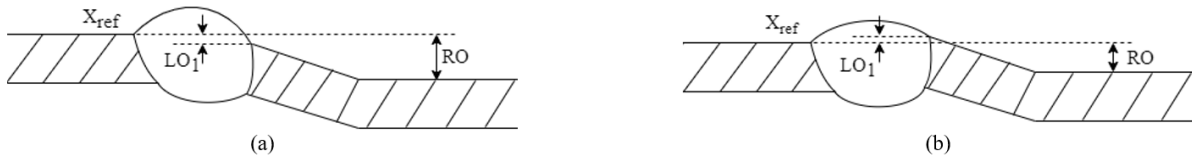


Figure 7.14: Illustration of  $LO_I$  measure relative to  $RO$  for two cases when (a)  $LO_I$  below  $X_{ref}$  (b)  $LO_I$  above  $X_{ref}$

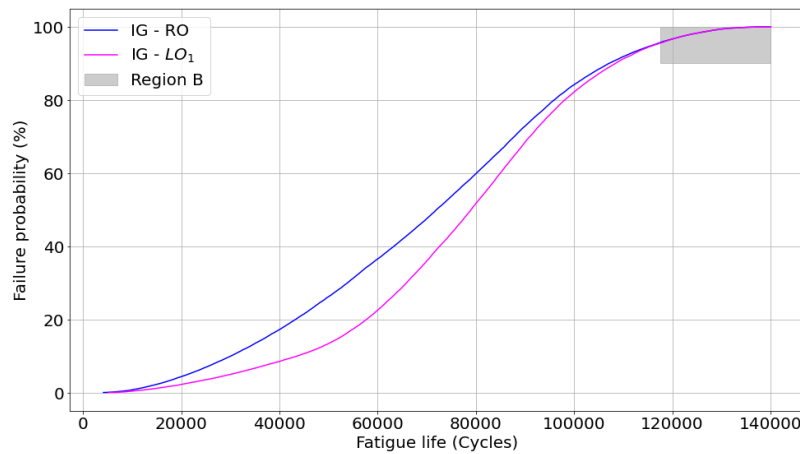


Figure 7.15: Empirical CDF of fatigue life for two offset measures -  $RO$  and  $LO_I$  [Thickness = 2.03 mm]

However, in *Region B* it is observed that both the offset measures estimate approximately the same fatigue lives. *Region B* corresponds to cases close to zero edge offset ( $RO$ ). As seen from the calculation of  $LO_I$  shown in Figure 7.13, certain values of  $RO$  and  $\theta$  can result in  $LO_I$  values close to zero. Therefore, the idealized geometry transfer function predicts similar life numbers for the two offset measures. It can be concluded that the  $LO_I$  measure does not produce conservative life estimates.

### 7.3.2 Life distribution based on IG- $LO_2$

The fatigue life vs failure probability for  $RO$  and  $LO_2$  measures, computed from the idealized geometry, is shown in Figure 7.17. The minimum and median lives for the two measures are tabulated in Table 7.7.

Table 7.7: Minimum life and median life for two offset measures -  $RO$  and  $LO_2$

Offset measure	Minimum life - 99.9% survival probability (cycles)	Median life – 50% survival probability (cycles)
$RO$	5679	71999
$LO_2$	42204	69761

It is observed that the  $LO_2$  measure predicts a much higher minimum life compared to  $RO$  measure, however the predicted median lives are close to each other. From Figure 7.17, in *Region C* the  $LO_2$  measure produces higher life estimates compared to  $RO$ . *Region C* corresponds to cases that tend to high edge offset ( $RO$ ) values. Due to this, within the defined design space, the  $LO_2$  measure is always less than the  $RO$  measure, as shown in Figure 7.16(a).



Figure 7.16:  $LO_2$  measure relative to  $RO$  in (a) *Region C* and (b) *Region D*

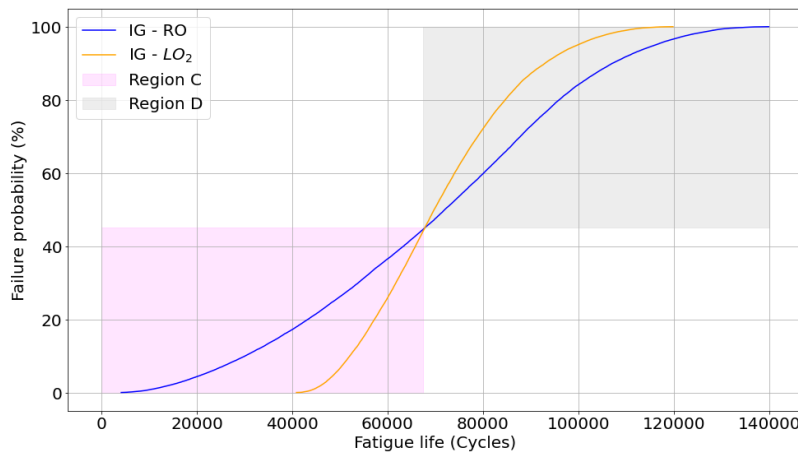


Figure 7.17: Empirical CDF of fatigue life for two offset measures -  $RO$  and  $LO_2$  [Thickness = 2.03 mm]

However, in *Region D*, the  $LO_2$  measure predicts lower life estimates compared to  $RO$ . In *Region D*, the sampled values tend to low edge offset ( $RO$ ) values, and the  $LO_2$  measure is always higher than the  $RO$  measure, as shown in Figure 7.16(b).

The fatigue life vs failure probabilities curves of all the cases discussed are shown in Figure 7.18. It is seen that the fatigue life predicted by  $LO_2$  measure approaches the life predicted by real geometry close to zero survival probability. Since the edge offset are close to zero in this region, the fatigue life is dictated by the local angular deflection ( $\theta$ ). Therefore, both the real geometry and  $LO_2$  measure produce similar life estimates.



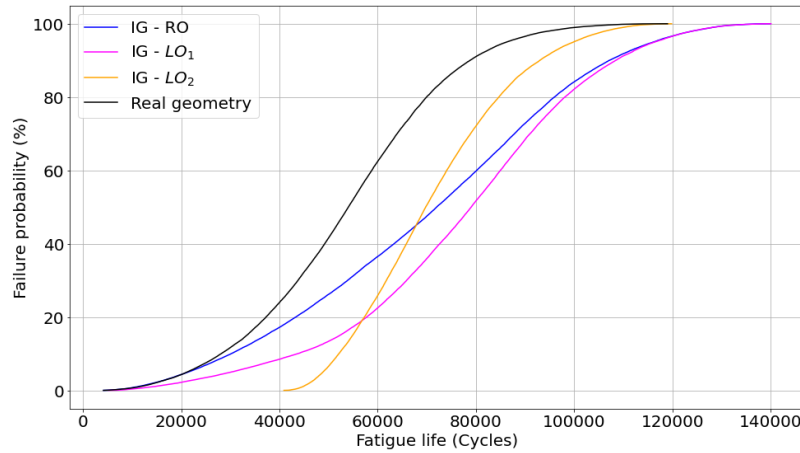


Figure 7.18: Empirical CDF of fatigue life for three offset measures and real geometry [Thickness = 2.03 mm]

It is also seen that none of the three offset measures yield conservative estimates compared to real geometry. The aim is to identify an offset measure that yields conservative life results using the idealized geometry. The results for one such offset measure is discussed in the following section.

### 7.3.3 Life distribution based on IG- $LO_4$

To obtain conservative life estimates compared to the real geometry, a fourth offset measure  $LO_4$  which accounts for offset due to both  $RO$  measure and local angular deflection  $\theta$  can be defined as,

$$LO_4 = RO + LO_2 \quad (27)$$

The life distribution is estimated using the idealized geometry (IG) transfer function. The fatigue life vs failure probabilities for  $LO_4$  measure, along with results from the other cases, are shown in Figure 7.19. The minimum and median lives for  $LO_4$  measure and real geometry (RG) are tabulated in Table 7.8.

Table 7.8: Minimum life for  $LO_4$  measure and real geometry

<i>Geometry Case</i>	<i>Minimum life - 99.9% survival probability (cycles)</i>	<i>Median life - 50% survival probability (cycles)</i>
IG - $LO_4$	5078	45446
RG	5739	54019



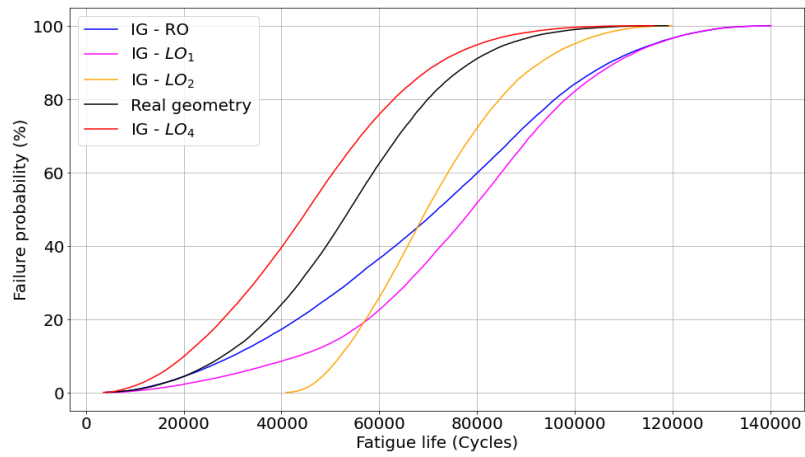


Figure 7.19: Empirical CDF of fatigue life for  $LO_4$  measure along with other cases

It is observed that the  $LO_4$  measure predicts a conservative minimum and median lives compared to the real geometry. From Figure 7.19, it is seen that throughout the distribution of life,  $LO_4$  measure produces conservative life estimates compared to the real geometry.

## 8 Conclusions

The effect of a distorted local geometry (real geometry) on the fatigue life is investigated. Measurements of different weld geometric parameters were compiled from two sources: non-conformance reports and weld qualification data, for Nickel and Titanium base materials, with a focus on Tungsten Inert Gas (TIG) and Laser Beam Welding (LBW) welding processes. A deterministic analysis is performed to investigate the influence of a real geometry on the fatigue life, and the results are compared with an idealized geometry.

Accounting for the variation in edge offset and weld toe radii from the weld measurements, a statistical method is devised to evaluate the sensitivity of life to the different weld geometric parameters. This method uses a transfer function or a surrogate model to estimate the fatigue life. Through using Monte Carlo simulations, the distribution of life is evaluated for the two geometry cases. The influence on life due to different edge offset measures from a real geometry is investigated, and a possible offset measure to obtain conservative life estimates with an idealized analysis geometry is explored.

The influence of thickness of the joining plates on the fatigue life is investigated, for an idealized geometry. Two measures of edge offset were studied: normalized edge offset and absolute edge offset.

Based on these investigations the following can be concluded:

- The real geometry around the weld region has a significant effect on life.
- Irrespective of the local weld geometry, the edge offset has the maximum influence on the variance in distribution of life. The root toe radius has the second highest influence, and for a real geometry, the contribution of root toe radius to variance in life increases. The top toe radius has a negligible influence on life.
- From the different edge offset measures investigated, it is observed that a simple local offset ( $LO_1$ ) measurement does not always produce conservative life estimates.
- A suggestion is to use the sum of  $RO$  and  $LO_2$  measure in the idealized geometry, to obtain conservative life estimates compared to the real geometry.
- Given the same normalized edge offset and same initial crack size, an increase in the plate thickness results in higher edge offset, which leads to a decrease in fatigue life.
- Given the same absolute edge offset and same initial crack size, an increase in thickness leads to lower crack growth rates, which results in an increase in the fatigue life.

### 8.1 Suggestions for future work

Weld measurements were compiled for different base materials and welding processes. This thesis focuses only on Nickel base TIG welds. Therefore, other welding process such as LBW, and other base materials, such as Titanium can be investigated.

The results presented in this thesis, are considering linear elastic material properties for the stress analysis and LEFM assumptions for the crack propagation analysis. The load ratio  $R$  is zero for all life calculations performed in this thesis. In reality, a material does not exhibit an elastic behaviour under loading. Instead, most materials exhibit an elasto-plastic behaviour. This can affect the  $R$ -ratio that is considered for the crack propagation analysis. The fatigue life distribution for the different cases can therefore be different, which can be investigated as a future work.

The influence of two main weld geometric parameters: edge offset and weld toe radii was investigated in this thesis. Other parameters such as the weld bead width, bead height etc. can be studied as part of a future work, to evaluate their influence on the fatigue life.

Finally, possibilities of experimental analysis can be investigated to validate the numerical results, since all the results presented in this thesis are from numerical analysis alone.

## 9 References

- [1] "Are these the aircraft engines of the future?," 2021. [Online]. Available: <https://blog.satair.com/are-these-the-aircraft-engines-of-the-future>. [Accessed 21 March 2023].
- [2] S. Ralph I., A. Fatemi, R. R. Stephens and H. O. Fuchs, *Metal Fatigue in Engineering*, 2nd ed., John Wiley & Sons., 2001.
- [3] W. Fricke, "Recent developments and future challenges in fatigue strength assessment of welded joints," *Proceedings of the Institution of Mechanical Engineers, Part C: Journal of Mechanical Engineering Science*, vol. 229, pp. 1224-1239, 2015.
- [4] A. Niraula, H. Remes and P. Lehto, "Local weld geometry-based characterization of fatigue strength in laser-MAG hybrid welded joints," *Weld World*, 2023.
- [5] T. Ninh Nguyen and M. Wahab, "A theoretical study of the effect of weld geometry parameters on fatigue crack propagation life," *Engineering Fracture Mechanics*, vol. 51, no. 1, pp. Pages 1-18, 1995.
- [6] C. Steimbregger, N. Gubeljak, T. Vuherer, N. Enzinger, W. Ernst and M. Chapetti, "Effect of welding processes on the fatigue behaviour of ultra-high strength steel butt-welded joints," *Engineering Fracture Mechanics*, vol. 275, no. 108845, 2022.
- [7] H. Gao, X. Zhang, P. Huang, H. Jiang and Z. Li, "Fatigue reliability of welded joints accounting for uncertainties in weld geometry," *Advances in Mechanical Engineering*, vol. 14, no. 5, 2022.
- [8] T. Månsson, "Stress analysis of butt welds," GKN Internal Report, VOLS: 10054978, Trollhättan, Sweden, 2014.
- [9] T. Månsson, "Crack propagation experiments and analysis in TIG welded IN718 sheet material," GKN Internal Report, VOLS: 10080555, Trollhättan, Sweden, 2009.
- [10] NASGRO 9.1 Manual, San Antonio, TX, USA: Southwest Research Institute, May 2019.
- [11] "Acceptance criteria for fusion welding," GKN Internal Report: VOLS: 10063557, Trollhättan, Sweden, 2012.
- [12] H. Söderlund, "Weld alignment dimensional inspection," GKN Internal Report: VOLS: 10285785, Trollhättan, Sweden, 2022.
- [13] R. O. Ritchie, "Influence of microstructure on near-threshold fatigue-crack propagation in ultra-high strength steel," *Metal Science*, Vols. 11:8-9, pp. 368-381, 1977.
- [14] D. Kujawski and F. Ellyin, "A fatigue crack growth model with load ratio effects," *Engineering Fracture Mechanics*, vol. 28, no. 4, pp. 367-378, 1987.
- [15] H. Benaroya and S. M. Han, *Probability Models in Engineering and Science*, Boca Raton: CRC Press, 2005.
- [16] D. C. Montgomery and G. C. Runger, *Applied Statistics and Probability for Engineers*, 3rd ed., John Wiley & Sons, Inc., 2002.

- [17] D. C. Montgomery, *Design and Analysis of Experiments*, 8th ed., Wiley, 2012.
- [18] V. Felipe A.C, “A Tutorial on Latin Hypercube Design of Experiments,” in *Quality and reliability engineering international*, 2016, pp. 1975-1985.
- [19] S. J.M. and A. D.F., “Large-sample Statistical Methods,” in *International Encyclopedia of Education (Third Edition)*, Elsevier, 2010, pp. 232-237.
- [20] “Inconel Alloy 718,” Special Metals, [Online]. Available: <https://www.specialmetals.com/documents/technical-bulletins/inconel/>. [Accessed 18 May 2023].
- [21] S. P. and A. F. M. A. , “Fatigue life prediction of adhesive joint in heat sink using Monte Carlo method,” *International Journal of Adhesion and Adhesives*, vol. 50, pp. 164-175, 2014.
- [22] D. Peña, “Design of Aero Engine Structures Using Additive Manufacturing,” 2015.

## 10 Appendix I

### 10.1 APDL script for mesh refinement

```

413
414      lsel,s,,,2,4,2      !Selection of weld toe radii
415      lsel,a,,,7,9,2
416      nsll,s              !Selecting nodes associated with radius arcs
417      *do,ii,1,7          !*DO loop for selecting neighbouring elements
418          esln,s          !Selecting elements associated with nodes
419          nsle,s          !Selecting nodes associated with elements
420      *enddo
421      SMRT,6              !Set Smart level sizing to 6
422      EREF,all,,,1,0,1,1  !Mesh refinement on selected elements
423      lsel,s,,,2,4,2      !Repetition of the above process for the 2nd time
424      lsel,a,,,7,9,2
425      nsll,s
426      *do,ii,1,5
427          esln,s
428          nsle,s
429      *enddo
430      SMRT,6
431      EREF,all,,,1,0,1,1
432      lsel,s,,,2,4,2      !Repetition of the above process for the 3rd time
433      lsel,a,,,7,9,2
434      nsll,s
435      *do,ii,1,5
436          esln,s
437          nsle,s
438      *enddo
439      SMRT,6
440      EREF,all,,,1,0,1,1
441

```

### 10.2 NASGRO FLABAT file structure

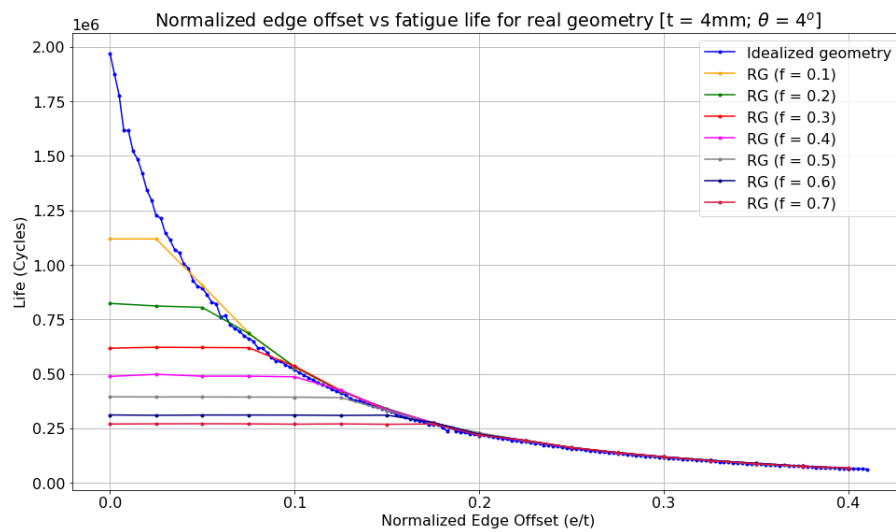
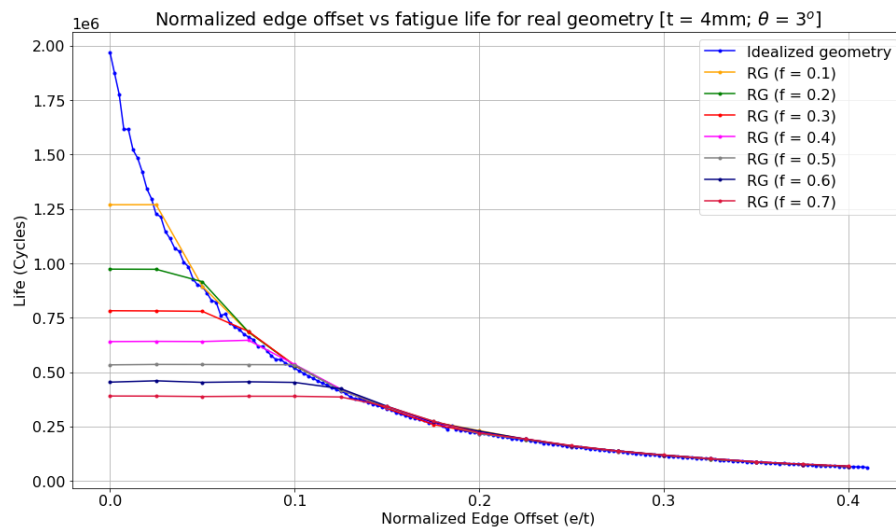
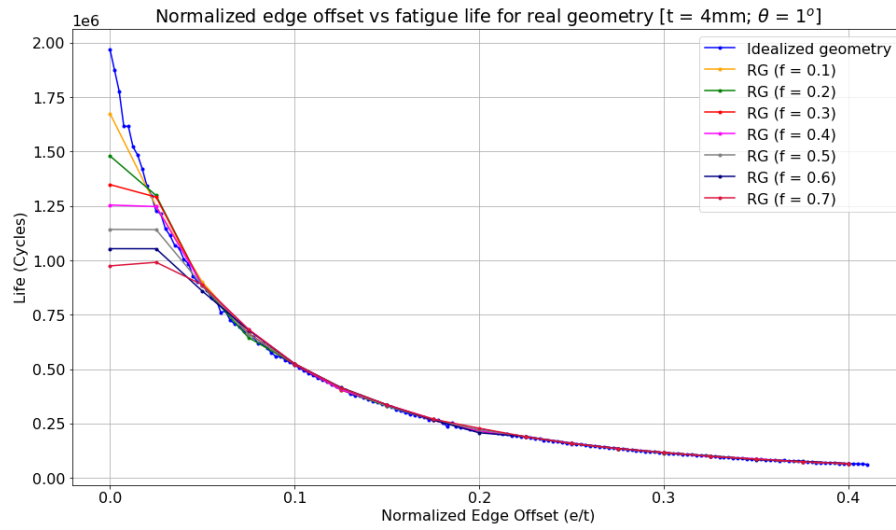
```

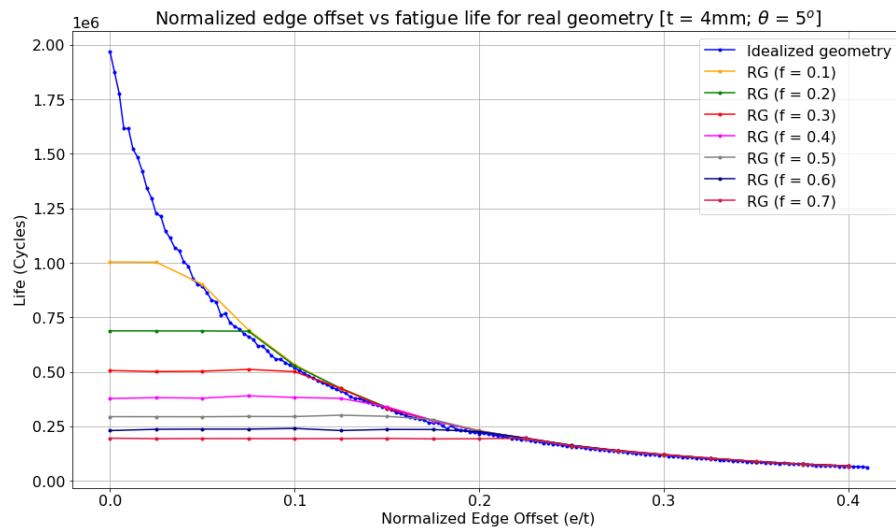
1  TMPOUT1
2  2
3  d
4  [no title given]
5  SC
6  30
7  2      [istrtype]
8  4      [Thickness, t]
9  15     [Width, W]
10 7.5    [Crack ctr offset, B]
11 2
12 2      [nsquan]
13 0      [tens,comp/t1,t2 option]
14 1      [jfiles]
15 N      [fullstresstensor]
16 *Mem_SG_file_name
17 *Bend_SG_file_name
18 0      [iresid]
19 OPS    [optimum point spacing]
20 0      [compounding option]
21 U
22 0.76   [Initial flaw size, a]
23 1      [Initial a/c]
24 0
25 NASMF.XMLZ
26 NASA data/NASGRO eqn (single temp)
27 0      [temperature option]
28 1      [mat count slider value]
29 N      [non-interaction]
30 3      [manual mode]
31 NI ALLOYS/SUPERALLOYS
32 Inconel alloys
33 Q3LB23AB1
34 Inconel 718 ST(1750F/954C) + A(1325F/718C/8h+1150F/621C/10h)
35 Forg Blk ; T-L & L-T; LA; Room temp
36

```

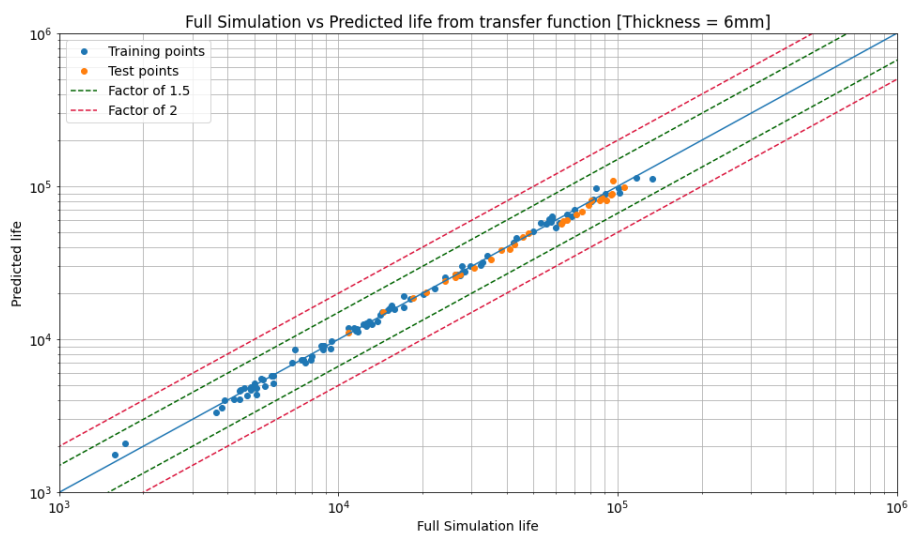
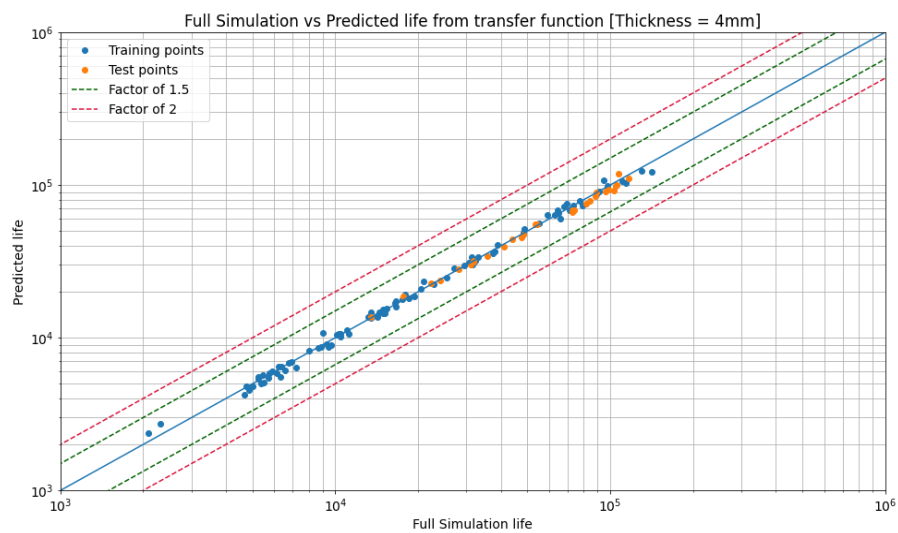
Placeholders to insert respective stress gradient file names

### 10.3 Fatigue life curves – Real geometry





## 10.4 Verification of transfer functions





## 10.5 MC convergence plots of *CAFL*

